Development and application of novel multiscale modeling techniques for studying the loss processes in polymer solar cell nanodevices

Dissertation

zur Erlangung

des Doktorgrades der Naturwissenschaften

(Dr. rer. nat.)

der Naturwissenschaftlichen Fakultät IV

-Chemie und Pharmazie-

der Universität Regensburg

vorgelegt von

Anton Pershin

aus Sankt Petersburg

September 2013

Die vorliegende Arbeit wurde in der Zeit von Mai 2010 bis September 2013 unter Anleitung von Herrn PD. Dr. Stephan A. Bäurle am Institut für Physikalische und Theoretische Chemie der Universität Regensburg angefertigt.

Prüfungsausschuss:

Prof. Dr. Burkhard König (Vorsitzender)

PD. Dr. Stephan Bäurle

Prof. Dr. Bernhard Dick

Prof. Dr. Thomas Niehaus

Folgende Ergebnisse dieser Arbeit sind bereits veröffentlicht bzw. eingereicht worden:

Kapitel 4:

A. Pershin, S. Donets und S. A. Baeurle,
"A new multiscale modeling method for simulating the loss processes in
polymer solar cell nanodevices",
J. Chem. Phys. **136**, 194102 (2012);
doi:10.1063/1.4712622

S. Donets, A. Pershin, M. J. A. Christlmaier und S. A. Baeurle
"A multiscale modeling study of loss processes in
block-copolymer-based solar cell nanodevices"
J. Chem. Phys. **138**, 094901 (2013);
doi: 10.1063/1.4792366

Kapitel 5:

A. Pershin, S. Donets und S. A. Baeurle,
"Photocurrent contribution from inter-segmental mixing in
donor-acceptor-type polymer solar cells: A theoretical study"
eingereicht (2013)

Kapitel 6:

A. Pershin, S. Donets und S. A. Baeurle,
"Performance enhancement of block-copolymer solar cells
through tapering the donor-acceptor interface:
a multiscale study"
eingereicht (2013)

Noch zu erwartende Publikationen im Rahmen der Doktorarbeit:

1. S. Donets, A. Pershin und S. A. Baeurle, “Optimizing and improving the performance of polymer solar cells by using a multiscale computer simulation technique”, in Vorbereitung

2. S. Donets, A. Pershin und S. A. Baeurle, “Simulating polymer solar cell nanodevices using cost-efficient multiscale parameterization”, in Vorbereitung

Acknowledgments

I would like to express the deepest appreciation to my doctoral adviser PD Dr. Stephan A. Baeurle for his patient guidance and for sharing his outstanding knowledge in the field of Theoretical Chemistry. Without his full support this thesis would not have been possible. I gratefully acknowledge the head of the chair Professor Dr. Bernhard Dick for the excellent working conditions within the Institute of Physical and Theoretical Chemistry at the University of Regensburg, and, in particular, for organizing the interesting research seminars and extremely useful comments during my presentations. I would also like to thank the members of our research group, namely, Dr. Emanuel Peter, Sergii Donets, Martin Christlmaier, and Ivan Stambolić, for their help and friendship. Special acknowledgements go to the Deutsche Forschungsgemeinschaft (DFG) for the financial support of the present work through the Grant No. BA 2256/3-1. Finally, I would like to thank Zsuzsanna Lurcza for her kind support and understanding during these difficult times.

“We know what kind of a dance to do experimentally to measure this number very accurately, but we don't know what kind of dance to do on the computer to make this number come out, without putting it in secretly!”

Richard Feynman

Contents

Theoretical backgroung

Results and discussion

1. Introduction

1.1 Organic solar cells: a promising technology for renewable energy

Every year over one hundred and twenty thousand terawatts of solar power irradiate the Earth [1]. In comparison to this, the global consumption of fifteen terawatts seems to be just a negligible quantity. Harvesting this power is a fascinating opportunity for the human society enabling to cover all the energy needs with a minimal effect on the environment. Nowadays, however, photovoltaic devices hardly contribute to the energy market, what is essentially related to the large initial costs to acquire the equipment. Modern solar cells are typically constructed by the use of expensive inorganic materials such as silicon, gallium-arsenide, and cadmium-indium-selenide [2]. Moreover, these materials also pollute the environment and need to be manufactured in a very pure monocrystal form, what produces a number of additional difficulties within the fabrication procedure.

In contrast to this, a new class of organic materials, conjugated polymers and molecules, are a promising alternative, capable to change the current status of solar energy in context of the global energy market. Conjugated polymers combine the electronic properties of traditional semiconductors with the ease of processing and mechanical flexibility [3]. An important advantage of these materials is the ability to tailor their properties, such as the width of band gap, by introducing simple chemical changes. Their use opens new possibilities for environmentally safe, flexible, lightweight large-scale electronics [4].

Although the organic solar modules can be manufactured with very low costs, their efficiency and stability is still insufficient to be competitive in nanodevice applications with respect to their inorganic counterparts. Moreover, the power conversion efficiency of these devices can hardly reach the values, obtained with the amorphous silicon-based solar cells. Nevertheless, recent calculations demonstrate that they can be used to generate low-cost energy. Even rough estimations of cost-efficiency, made for the modules with the power-conversion efficiency of 9% and a lifetime of 5-10 years, show that these devices can produce one kWh of energy for about 10 Eurocent in Middle Europe [5].

The relatively low power conversion efficiency of organic photovoltaic (OPV) cells can mainly be attributed to loss phenomena of the elementary particles involved in the

photovoltaic process, such as photon loss, exciton loss, and charge carrier loss [6]. With the exception of the process of exciton diffusion to the donor-acceptor (DA) heterojunction, none of these processes have been optimized in a satisfactory way in case of the polymer solar cell materials currently available. This optimization has to be done simultaneously with respect to the optical and electrical properties, which may result in the development of new active materials. Under these circumstances, theoretical models, capable to emulate the entire fabrication process of the solar cells, would be an extremely useful tool, allowing to explore the full range of design alternatives by providing key insights into the physics of solar cell operation [7].

During the past decade, the maximum values of the photovoltaic efficiency of organic solar cells have increased from 1 % to more than 8 % [8], whereas the outdoor lifetime has grown from a few hours up to 15000 h [9]. This steady progress sustain the rational hope that already in foreseeable future organic solar cells will play an important role as a powerful source of green energy.

1.2 Current-voltage characteristics of organic solar cells

To characterize the performance of a solar cell in an electrical circuit, it is common to consider several basic device parameters, namely, the short circuit current (I_{sc}), open circuit voltage (V_{oc}), fill factor (FF), and power conversion efficiency (PCE), which are usually obtained from the current-voltage (IV) curve. This curve describes the relationship between the electric current through the electronic device and the corresponding voltage across its terminals. A typical IV curve has a shape, as depicted in Fig. 1.1. Let us in the following provide the physical meaning of these basic device parameters and show, how they can be obtained from the IV curve [10].

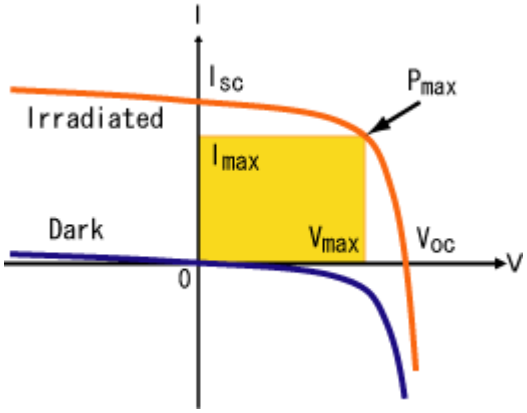

Fig. 1.1: A typical current-voltage curve, describing the dependency of the current through a solar cells device on the applied voltage. The red curve describes the dependency under illumination, whereas the blue curve is obtained in the absence of light [11].

The first parameter is the short circuit current, which is the current through the device, when the voltage of the solar cell is zero (see Fig. 1.1). This quantity characterizes the largest photocurrent, which can be gained from the solar cell. In case, when there is with no internal losses in the system (an "ideal" cell), the short circuit current is the total current, produced in the solar cell by photon excitation. The second parameter is the open circuit voltage, which is the maximum voltage, obtainable from a solar sell. This situation occurs at zero current through the device, which depends on the saturation current of the solar cell and the light-generated current. Since the saturation current is influenced by the charge recombinations in a solar cell, while the maximum of photocurrent has usually small variations with respect to the active material, this parameter can be used to measure the amount of recombinations in the system. The next parameter is the fill factor, which is defined as the ratio of the maximum power from the solar cell to the product of V_{oc} and I_{sc}, given as:

$$\mathrm{FF} = \frac{P_{\max}}{I_{sc} \times V_{oc}}, \tag{1.1}$$

where

$$P_{\max} = \max\{I_i \times V_i\}, \tag{1.2}$$

is the maximum power, which can be obtained from the device. This parameter can be used to assess the amount of internal losses and represented as square area in Fig. 1.1. Finally, the power conversion efficiency is the most commonly used parameter to compare the performance of one solar cell device to another. It is defined as the fraction of incident power converted to electricity, given as:

$$\mathrm{PCE} = \frac{P_{\max}}{P_0} \cdot 100\%, \tag{1.3}$$

where P_0 is a power of illuminating light.

It is also worth mentioning that together with the photocurrent, one can observe in Fig. 1.1 a dark current through the device, which is especially large for the high values of applied bias. This current can potentially interact with the photocurrent, changing the amount of internal losses in the system. The influence of the dark current on the device performance will be one of the subjects described in chapter 4.

1.3 Device structure and operation

The simplest OPV cell can be produced by clamping a thin layer of organic semiconducting material between two electrodes where one of the electrodes is optically transparent. For the construction of an OPV device, indium tin oxide (ITO) represents an important material, which is characterized by high optical transparency and electrical conductivity, and is frequently used as anode, whereas the low work-function metals, for example Al, Mg, and Ca, are used as cathode [8]. The difference in work functions of the two electrodes generates an internal electric field, which is caused by built-in potential. This electric field drives the photoinduced electrons to the electrode with low work function and the holes to the opposite electrode with high work function, which induces a photocurrent. In practice, however, such solar cells possess very small power conversion efficiencies, which raises the question: why this technology works for the silicon-based solar cells?

Years of study on this question have demonstrated that OPV devices differ from their inorganic counterpart in many fundamental aspects. First of all, the mobilities of the charge carriers in organic semiconductors are several orders of magnitude lower than those found in

the crystalline inorganic materials [13]. Nowadays, even the highest reported values of hole mobilities in semicrystalline polymers reach only 0.6 $cm^2V^{-1}s^{-1}$ [14] (for silicon, it is 450 $cm^2V^{-1}s^{-1}$), whereas the difference between the electron mobilities in polymers (0.1 $cm^2V^{-1}s^{-1}$) and silicon (1400 $cm^2V^{-1}s^{-1}$) is even higher [15]. As a result, the charge transport properties in OPV devices are better described by a hopping mechanism, in contrast to the band theory, successfully used for most of the inorganic semiconductors.

The second important difference between the organic and inorganic materials lies in the value of exciton binding energy, which are much higher for organic semiconductors (~0.5 eV, [16]) in comparison to the silicon-based materials (~0.01 eV). When the organic semiconducting phase absorbs light, electrons in the conduction band and holes in the valence band are generated. However, due to the low permittivity, this newly formed hole-electron pair, which is also known as singlet exciton, is strongly bound. Thus, the thermal energy (~0.025 eV at room temperature) is not sufficiently high to disassemble the exciton into the free charges − some additional energy is required. This explains why the power conversion efficiency (PCE) of single-layer devices does not exceed 0.1 % [13].

To accomplish the charge separation in an effective way, Tang [17] developed a two-layer OPV cell consisting of a semiconducting donor (D) material with low electron affinity and a semiconducting acceptor (A) material with high electron affinity, depicted in Fig. 1.2 (a). In such a cell, light absorption induces the creation of excitons in the material, which can diffuse in all directions by minimizing the energy. The fraction of excitons, reaching the DA interfacial region also called the DA heterojunction, can be separated into free charge carriers, where the electrons are migrating into the lowest unoccupied molecular orbital (LUMO) of the electron acceptor and the holes in the highest occupied molecular orbital (HOMO) of the electron donor. After the charge separation process has taken place, the electrons are transported within the A material and the holes within the D material to the respective electrodes [17].

Although the PCE of the planar bilayer heterojunction devices is more than 10 times higher than in case of the single-layer devices, the quantity is still limited through the exciton diffusion length [18], which characterizes the average distance excitons can travel through a material before annihilation occurs through geminate recombination [19]. In most organic

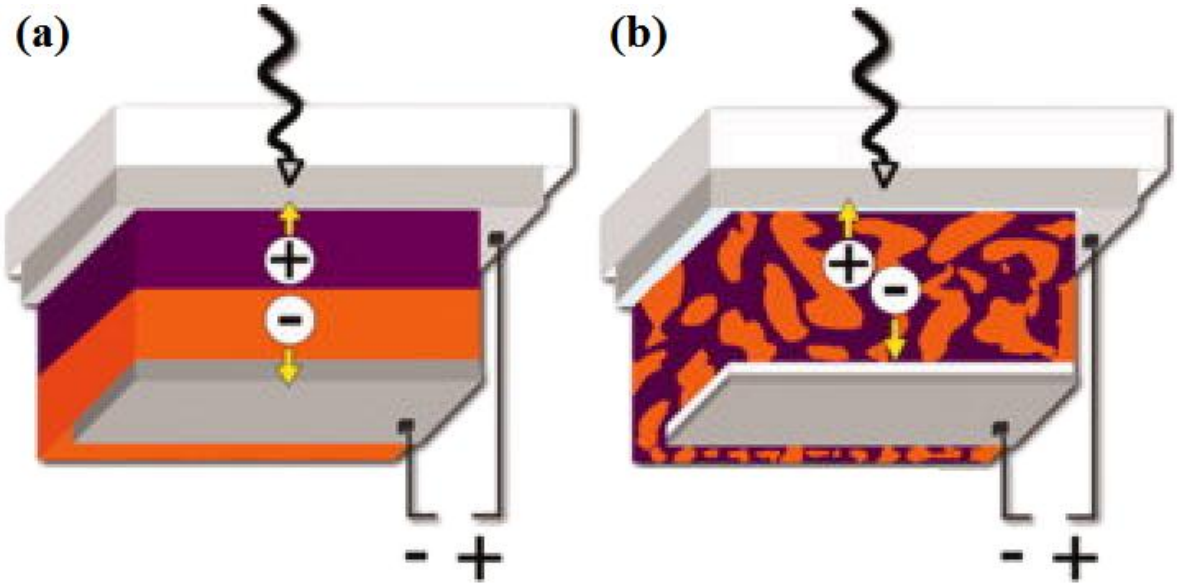

Fig. 1.2: Typical device architecture of (a) bilayer solar cells, and (b) bulk heterojunction solar cells [18].

semiconductors the exciton diffusion length typically adopts a value of about 3–10 nm [20]. The active volume of this type of OPV cell is, because of the previously mentioned annihilation processes, restricted to a very small region near to the interface. However, it is generally not large enough to absorb the major part of the radiation energy and for an efficient power energy conversion.

To further increase the performance of OPV cells, tremendous efforts have been realized in the last few years to develop new nanostructured materials, in which the size of the active volume is adjusted to accommodate the optimal exciton diffusion length. In case of the so-called bulk heterojunction (BHJ) the nanostructured morphology ensures that all excitons can reach the DA interface within the exciton diffusion length (see Fig. 1.2 b). This construction is to date the most successful OPV cell.

1.4 Optimization of polymer nanomorphology

The progress in the field of organic solar cells, achieved during the last several years, can primary be attributed to the optimization of the nanomorphology of the device active

layer. In practice, this optimization can be achieved through two different strategies, which may be carried out simultaneously. The first strategy is to manipulate the material's composition by changing the chemical structure and/or molecular weights. As an example for this technique, we can mention the systematic improvement of performance of poly[(9,9-dioctylfluorenyl-2,7-diyl) -alt- (4,7-bis(3-hexylthiophen-5-yl) -2,1,3-benzothiadiazole)-2',2''-diyl] (F8TBT) and [6,6]-phenyl C61 butyric acid methyl ester (PC61BM) blends, observed with the grow of F8TBT molecular weight [21]. The second strategy is to influence on the process of preparation by controlling the external conditions. For instance, for the well-known system poly(3-hexylthiophene):[6,6]-phenyl C60 butyric acid methyl ester (P3HT:PCBM), thermal annealing of the initial morphology at 75 ^{o}C can improve the efficiency from 0.4 % to 2.4 % [22]. Similar improvements can be achieved at room temperature by "solvent annealing" or "solvent vapor annealing" [20].

Since the time the importance of the morphology optimization was realized, there were a number of scientific works suggesting how the morphology can be controlled. These works involved a large variety of experimental techniques, applied for the morphology characterization. However, these techniques turned out to reach their limits very rapidly. For example, X-ray diffraction techniques can provide useful information about molecular packing in crystals, but they are not applicable for amorphous polymer alloys [23]. Electron microscopy enables to determine the domain size, but often with a large error, like in case of the P3HT/PCBM blends [24]. The NMR technique can give the nearest-neighbor information, but can hardly be extended to resolve the domain size [25]. On the other hand, combination of different experimental techniques, including the above mentioned methods together with scanning probe microscopy, neutron scattering, and atomic force spectroscopy, provides previous information about the morphology and charge transport in OPV devices, but this requires both significant efforts and an access to the corresponding equipment. There are, however, several problems, which cannot be solved experimentally even by this combination of measurement tools, such as, for example, the characterization of amorphous domains. The only available tools here are computational.

With an appropriate mathematical model in hand, it becomes possible to discover and characterize new materials without significant spending on experimental equipment and reagents. As a matter of fact, these models are already extensively used in the field of organic

electronics, showing very promising results. For example, in the work of Sokolov *et al*. the combination of molecular dynamics and quantum chemistry enabled to discover a new compound with a hole mobility of 16 $cm^2V^{-1}s^{-1}$, which is still almost unique for the organic semiconductors [26]. The development of a suitable theoretical model for treating the photovoltaic processes in polymer solar cell nanodevices was a major goal of this thesis. As a final remark to this chapter, we should mention that the computational investigations of photovoltaic processes do not have the purpose to replace the experimental methods, but rather to provide an additional analyzing tool to elucidate certain phenomena, which are not accessible with experimental measurements. Ideally, the simulations and experiment should be used in tandem to accelerate the design of new functional materials.

1.5 Modeling of polymer-based solar cells

The first attempt to describe theoretically the effect of the morphology on the performance of polymer solar cells was made by Walker *et al.* [28], who determined the internal quantum efficiencies for a set of phase-separated morphologies, which differed from each other in the values of polymer domain size. In this model, the Ising spin Hamiltonian was employed to simulate the different degrees of phase separation, whereas the optoelectronic properties of the devices under investigation were simulated by using the kinetic Monte Carlo technique. Even if the results of these simulations were in good agreement with the experimental data, the main drawback of this approach was the absence of a realistic polymer model, describing the polymer phase separation process within the active layer of the OPV device. The development of such a model represents a challenging task for modern computational chemistry.

As the most accurate level of system description, one could describe a polymeric mixture by using *ab initio* methods of quantum mechanics, which take into account nuclear coordinates and electronic degrees of freedom. This approach allows investigating the interactions between the particles, composing the mixture, without additional assumptions and knowledge from experiment. The disadvantage of these methods is that they can deal only with systems consisting of less than 1000 atoms, what is not useful for polymers, where each

chain contains more than this number of atoms. In the next higher level of description, one can eliminate electronic degrees of freedom and treat the nuclear motion classically. This elimination is done by introducing classical potentials, describing the potential energy as a function of nuclear coordinates [27]. However, modern computational facilities do not allow the treatment of the systems, containing more than 10^6 atoms for the trajectories, longer than 1000 ns. These numbers are still too small for polymers, where equilibration of the system may take seconds, hours, or even days.

To solve this problem, an alternative approach can be used, in which the fundamental degrees of freedom are not the particle positions and momenta, but rather a continuous scalar field function that varies with position **r** [29]. To decouple the interactions between the particles and replace them by the field function, one uses particles-to-fields transformation. This transformation can be performed exactly, through the technique known as Hubbard-Stratonovich transformation. The numerical implementation method, describing the behavior of polymeric chains within the mean-field approximation, is called the self-consistent field theory (SCFT). It enables to increase the resolution from 0.01 nm for particle-based approaches up to 1 nm for the field-based simulations, which significantly reduces the computational costs, allowing to perform simulations for large polymeric systems within the length- and time-scales of practical interest. Therefore, in context of solar cell applications, the field-theoretic technique seems to be the most appropriate choice for the calculations of nanoscale polymeric morphology.

On the other hand, we should point out that, although the polymeric morphology determines the efficiency of polymer-based solar cells to a large extent, this is not the only factor, which needs to be taken into account. In particular, the performance of OPV devices is also limited by molecular packing of solids, contacts between polymers and electrodes, the value of HOMO-LUMO gap, reorganization energy, etc. Unfortunately, many of these effects cannot be treated within a unified formalism without further approximations. To overcome this problem, in the present thesis we propose to treat the photovoltaic processes in polymer-based solar cell nanodevices as a multiscale problem. Multiscale modeling generally implies that different kind of information, characterizing the system under investigation, can be sampled from different levels of its description. In the context of the OPV simulations presented herein, we combine the mesoscopic level, which is treated by field-theory, with the

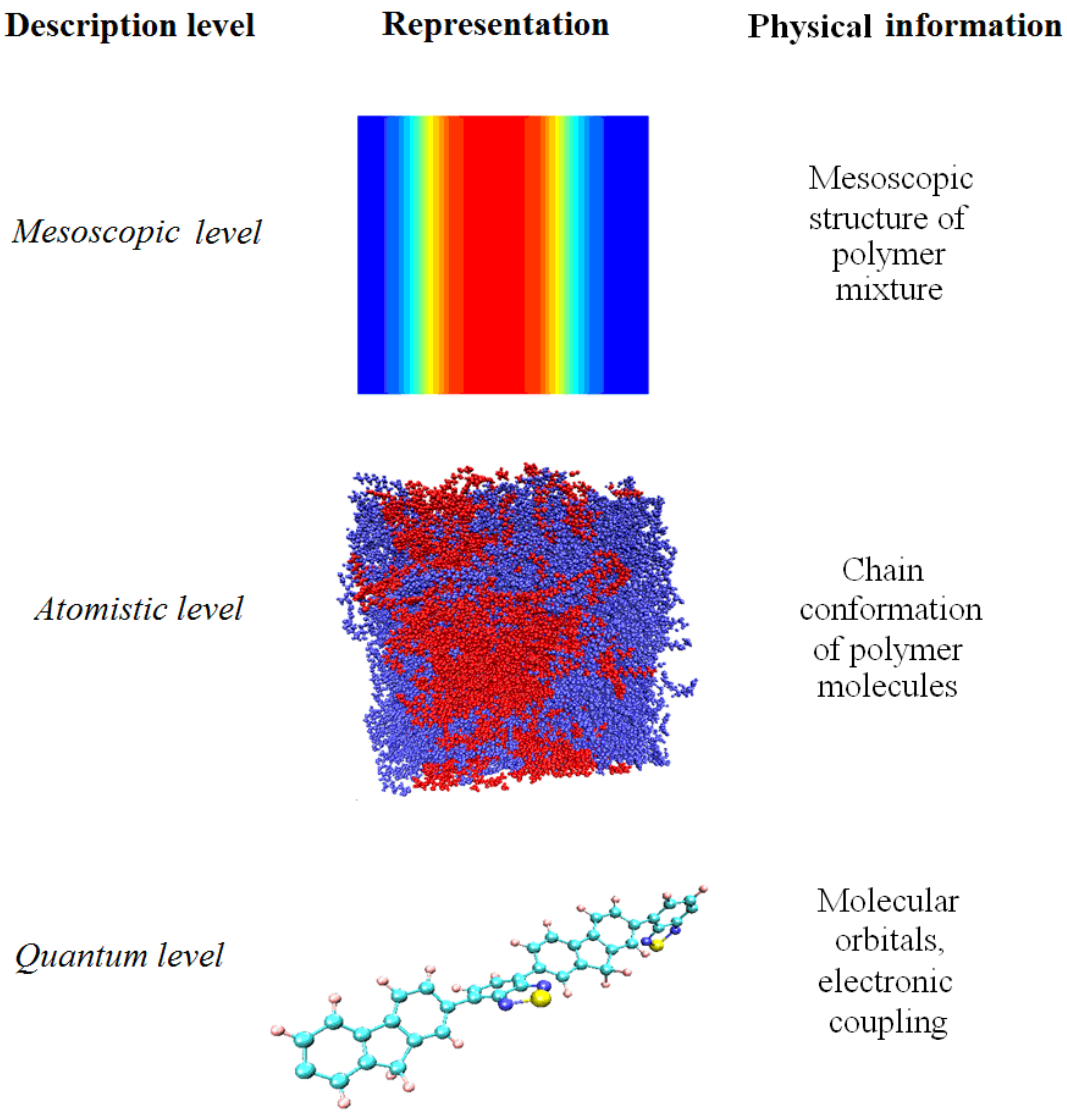

Fig. 1.3: Illustration of multiscale modeling concept for simulating the photovoltaic processes in organic solar cells

atomistic level, described by molecular dynamics simulations, and the quantum level, described by using the density functional theory or semi-empirical methods (see Fig. 1.3). The mesoscopic level provides us the information about nanoscale bulk morphology and polymer contacts with the electrodes. At the atomistic level, we can follow the conformational dynamics of polymer chains and changes in molecular packing. The quantum level is needed to determine the rates of the charges, moving through the morphology. The effective linking between these levels will enable us to explore the whole range of factors, which affect the performance of organic solar cells. The multiscale model, which we are presenting in this

thesis, can describe a wide variety of phenomena simultaneously within only one simulation cycle. It unifies the knowledge from different fields of theoretical chemistry and physics with the goal of optimizing the loss processes in polymer based solar cells.

1.6 Scope of the thesis

In this thesis, our goal is to elucidate the causes for the loss processes in polymer-based solar cells and asses their influence on the photovoltaic performance. We are primary interested in two types of loss processes, namely, exciton- and charge-losses, occurring within the active layer of solar cell nanodevices. In order to study these processes, we will develop different multiscale solar cell algorithms, allowing to predict the relationship between polymeric morphology and optoelectronic properties of the materials, such as the internal quantum efficiency, fill factor, power conversion efficiency, etc. To reach this goal, we intend to make use of polymer field theory to determine the morphology, whereas the photovoltaic processes will be described with a suitable kinetic Monte Carlo method. To treat the density fluctuations and analyze the effect of conformational defects, we will accomplish a field-to particle transformation by performing direct mapping between mesoscopic and atomistic levels. Regarding the morphological effects, we will concentrate on the study of loss processes at structural defects, such as dead-ends and bottlenecks, appearing during the device fabrication procedure. In addition, we will investigate the influence of the influence of interfacial mixing of monomers between donor- and acceptor-domains, chemical changes of polymer structure, achieved by photo-degradation of polymer chains. Finally, by studying different types of polymer architectures, namely, polymer blends, diblock-copolymers, triblock-copolymers, and tapered block-copolymers, we will show how the developed algorithms can be used to improve the photovoltaic performance of polymer solar cell nanodevices.

Theoretical background

2. Photovoltaic processes in organic solar cells

The photoconversion mechanism in organic solar cells may be divided into five components: light absorption, exciton transport, exciton dissociation, charge transport, and charge collection. The photovoltaic performance represents the combination of the efficiencies of all these processes, which can be quantitatively described by the value of internal quantum efficiency (IQE), η, as [10]:

$$\eta = \eta_{\mathrm{EDE}} \eta_{\mathrm{CTE}}, \tag{2.1}$$

where η_{EDE} is the exciton dissociation efficiency (EDE) and η_{CTE} is the charge transport efficiency (CTE). Generally, the internal quantum efficiency shows how efficient the active layer of the solar cell can use the photons, and, therefore, optimizing this value represents the main subject of this thesis. The present chapter aims to show how the components of the internal quantum efficiency can be obtained theoretically for a given morphology of the active layer. In our description, we start with a consideration of Förster resonance theory and different charge transport models, used for organic semiconductors. Then, we introduce the Marcus theory together with the related parameters and methods of their determination. Finally, we describe the dynamical Monte Carlo modeling technique, which we apply for studying the elementary photovoltaic processes in the active layer of the device.

2.1. Förster resonance theory

As we have already mentioned in the introduction, light absorption in organic semiconductors leads to the formation of a mobile electron-hole pair, which is called exciton. The effectiveness how the exciton is separated by forming of free charges determines the photovoltaic performance to a large extent. Since the exciton is primary dissociated at the DA interface, it is crucial to include an exciton transport in the model for simulating the photovoltaic processes in organic solar cells. One of the possibilities to describe this process

is to compute the exciton transfer rate between two states by employing the Förster resonance energy transfer theory [30].

To demonstrate the basic idea of the Förster theory, let us consider the following process of exciton transfer:

$$D^* + A \rightarrow D + A^*, \tag{2.2}$$

where D* (D) represents the excited (ground) state of the donor molecule and A (A*) is the ground (excited) state of the acceptor molecule, respectively. The ground electronic state consisting of D and A is denoted as $|g\rangle$, the donor exciton state consisting of D* and A as $|D\rangle$, and the acceptor exciton state consisting of D and A* as $|A\rangle$. All other degrees of freedom are defined as the bath. The bath Hamiltonian corresponding to $|g\rangle$ is H_b.

Let us assume that an impulsive and selective creation of $|D\rangle$ is possible while the bath remains in the canonical ensemble for $|g\rangle$. Then, the effective total Hamiltonian governing the exciton and bath can be expressed as [31]:

$$H = (E_D + B_D)|D\rangle\langle D| + (E_A + B_A)|A\rangle\langle A| + J(|D\rangle\langle A| + |A\rangle\langle D|) + H_b, \tag{2.3}$$

where E_D is the energy of $|D\rangle$, E_A is the energy of $|A\rangle$, and J is the electronic coupling. B_D is a bath operator representing the displacement of bath modes upon the creation of $|D\rangle$ and B_A is that for $|A\rangle$. At a non-zero time, the probability to find the exciton state $|A\rangle$ is

$$P_A(t) = Tr_b\{\langle A \mid e^{-iHt/h}\rho(0)\, e^{iHt/h}|A\rangle\}. \tag{2.4}$$

For short enough time, we can determine the perturbation expansion of the above mentioned expression with respect to $H_{DA} = J(|D\rangle\langle A| + |A\rangle\langle D|)$. Expanding $P_A(t)$ up to the second order of t and taking its time derivative, we obtain the following time dependent rate of energy transfer:

$$k(t) = \frac{2J^2}{\hbar^2}\mathrm{Re}\left[\int_0^t dt' e^{i(E_D - E_A)t'/\hbar}\frac{1}{Z_b}\mathrm{Tr}_b\{e^{i(H_b+B_D)t/\hbar}e^{-i(H_b+B_A)t'/\hbar}e^{-i(H_b+B_D)(t-t')/\hbar}e^{-\beta H_b}\}\right]. \tag{2.5}$$

The last expression can be used to evaluate the rate of resonance energy transfer between two states, which can be computed as follows:

$$k_F = \frac{9000(\ln 10)\kappa^2}{128\pi^5 N_A \tau_D n^4{}_r R^6}\left(\int d\tilde{\nu}\ \frac{f_D(\tilde{\nu})\varepsilon_A(\tilde{\nu})}{\tilde{\nu}^4}\right), \tag{2.6}$$

where κ^2 is the dipole orientation factor, R is the distance between the donor and the acceptor, τ_D is the lifetime of the spontaneous decay of $|D\rangle$ state, $f_D(\tilde{\nu})$ is the normalized donor emission spectrum, and ε_A is the molar extinction coefficient. For the detailed derivation of eq. (2.6) we refer the reader to [31].

In context of organic solar cells it is more common to use the closed form of the last equation, given as:

$$k_F = \frac{1}{\tau_D}\left(\frac{R_0}{R}\right)^6, \tag{2.7}$$

where R_0 is called the Förster radius, representing the critical distance at which the fluorescence probability is equal to the probability of energy transfer [32].

This model, however, does not consider effects of inhomogeneous broadening and energetic disorder, which may lead to considerable large errors in prediction of exciton diffusion parameters [33]. This disadvantage can be overcome by introducing into the expression the *f*-function, representing the Boltzmann factor, which considers the relative energy state differences of donor and acceptor:

$$k_F = \frac{1}{\tau_D}\left(\frac{R_0}{R}\right)^6 f(E_i, E_j). \tag{2.8}$$

The *f*-function is defined according to the relationships:

$$f(E_i, E_j) = \begin{cases} e^{\left(-\frac{E_j - E_i}{k_B T}\right)} & \text{if } E_j > E_i, \\ 1 & \text{if } E_j < E_i \end{cases} \tag{2.9}$$

where E_i and E_j are the site energies of the donor and acceptor molecules, respectively, corresponding to the density-of-states (DOS), which is often described by a Gaussian distribution with standard deviation, σ [34].

2.2 Charge transport models

As revealed through the eq. (2.1), the charge transport efficiency is a second contribution to the internal quantum efficiency, which represents the number of collected charges per number of dissociated excitons and can be determined by simulating the charge transport through the disordered organic materials. However, up to now there is no general model, which could describe the charge transport for the broad range of external conditions, such as, for example, the temperature. Every existing model, describing charge transport in organic semiconductors, is adjusted to the system under investigation. Each of these models is based on an idealized representation of the system which is achieved by a set of standard and well-established approximations.

To illustrate where these approximations come from, let us consider the minimalist model, which is used for the description of charge transport mechanisms. This model deals with a one dimensional array of molecules, characterized by one electronic state and one optical phonon per molecule. A convenient Hamiltonian for the model in terms of second quantization is given by [35]:

$$H = H_{\text{el}}^0 + H_{\text{phon}}^0 + V_{\text{el}} + V_{\text{local el-phon}} + V_{\text{impurities}}, \tag{2.10a}$$

$$H_{\text{el}}^0 = \sum_j \varepsilon_j a_j^{\dagger} a_j, \tag{2.10b}$$

$$V_{\text{el}} = -J \sum_j a_j^{\dagger} a_j + 1, \tag{2.10c}$$

$$H_{\text{phon}}^0 = \sum_j h\omega_0 \left(b_j^{\dagger} b_j + \frac{1}{2} \right), \tag{2.10d}$$

where $a^{\dagger}$ and a are the creation and annihilation operators of a charge carrier, respectively, and $b^{\dagger}$ and b are the corresponding operators for the phonon. V_{el} reflects the interactions between each localized site and its neighbors, where J describes the electronic coupling and is also known as the charge transfer integral. $V_{\text{local el-phon}}$ is the local electron-phonon coupling and has the meaning of a reorganization energy, whereas H_{el}^0 and H_{phon}^0 represent electronic and nuclear Hamiltonians of the non-interacting molecules. Note that the distribution in ε_j describes the density of states as long as *J* defines the tunneling time scale [36].

Despite the simplicity of the minimalistic model, even this model cannot be used for calculations of transport properties in organic semiconductors, such as, for example, charge mobility, without further approximations. In practice, one considers two limit cases of the eq. (2.10), which lead to two different simulation strategies for the investigation of charge transport properties:

1. Electronic coupling J is much smaller than the reorganization energy, $V_{\text{local el}-\text{phon}}$. In this case, charges are localized at certain parts of the molecules and their motion can be seen as a consequence of uncorrelated thermal hops. This approximation is considered to be the most relevant to the charge transport mechanism in organic semiconductors at high temperatures.
2. The second case is the situation when the electronic coupling is much larger than all the other energies. Here, the charges are delocalized over the molecules and the theory which is employed is called a band model. This formalism corresponds to the charge transport at low temperatures.

Since we were primary interested in studying the photovoltaic processes under operation temperatures, the first of the previously mentioned approximations has been used in all our simulations. The theories, describing charge transport under low temperatures, such as the tight binding theory [35], remained beyond the scope of present thesis, and, therefore, will not be present here. As a final remark to this chapter we should mention that there is a case of particular interest when the electronic coupling is comparable to the electron-phonon coupling. In this case, one gets quasi-particles, also known as polarons, in which the electronic core is surrounded by the phonon cloud [37]. This effect was also included into our simulation model by the appropriate choice of the charge transport theory.

2.3 Marcus theory

Theories, describing the rates of charge transfer between weakly coupled donor and acceptor molecules, are mainly addressed by the work of R.A. Marcus, which has been originally published in 1956 [38]. Its original results have been found wide application up to

now in charge transport of organic materials. Marcus theory deals with the calculation of the reaction rate for the electron transfer between donor and acceptor molecules:

$$D + A = D^{+} + A^{-}. \tag{2.11}$$

This electron transfer in organic semiconductors is accomplished by structural reorganizations of both directly involved and surrounding molecules and mediated by a nuclear coordinate, Q. The Hamiltonian, describing this process, can be written as [39]:

$$H = |D\rangle H_D \langle D| + |A\rangle H_A \langle A| + V \tag{2.12}$$

where $|D\rangle$ and $|A\rangle$, refer to the potential energy surfaces for the electron located on the donor and acceptor molecules, respectively, as long as *V* defines the coupling between the surfaces. These surfaces are represented by the harmonic potentials, which are identical in shape, but displaced with respect to each other vertically in energy and horizontally along the reaction coordinate.

Transfer rate between these two states can be evaluated by employing Fermi Golden Rule, given as:

$$w_{kl} = \frac{2\pi}{\hbar} \sum_{l} p_l |V_{kl}|^2 \delta^2 (E_k - E_l) = \frac{1}{\hbar^2} \int_{-\infty}^{+\infty} dt \langle V_I(t) V_I(0) \rangle, \tag{2.13}$$

where p_l is a probability of occupying the *l*-th state and δ is the Dirac delta function.
By using $V_I(t) = e^{iH_0 t/\hbar} V e^{-iH_0 t/\hbar}$, the electron transfer rate can be written as:

$$\begin{aligned} w_{ET} &= \frac{|J|^2}{\hbar^2} \int_{-\infty}^{+\infty} dt e^{-i(E_A - E_D)t/\hbar} \left\langle e^{iH_D t/\hbar} e^{-iH_A t/\hbar} \right\rangle \\ &= \frac{|J|^2}{\hbar^2} \int_{-\infty}^{+\infty} dt e^{-i(E_A - E_D)t/\hbar} \left\langle \exp\left[-\frac{i}{\hbar} \int_0^t dt' e^{iH_D t/\hbar} (H_A - H_D) e^{-iH_A t/\hbar} \right] \right\rangle, \end{aligned} \tag{2.14}$$

The last equation can be expressed in terms of correlation- and lineshape-functions, which in the classic limit, e.g. $k_B T >> \hbar\omega$, leads to the final expression for the electron transfer rate of the semi-classical Marcus theory, given as:

$$w_{ET} = \frac{|J|^2}{\hbar^2} \sqrt{\frac{\pi}{\lambda k_B T}} \exp\left[\frac{-(E_A - E_D + \lambda)^2}{4\lambda k_B T} \right], \tag{2.15}$$

where the parameter J is called charge transfer integral, λ is the reorganization energy, and $\Delta E = E_A - E_D$ is the site energy difference, whose physical meanings were described

previously. From the previous discussion, we deduced that only these three parameters have to be determined additionally. The methods of their determination will be described in the following chapters.

2.4 Charge transfer integral and site energy difference

The charge transfer integral is one of the most important parameters, required for the simulation of transport properties of organic semiconductors. There are various methods for its calculation such as, for instance, the direct method, the site-energy correction method, and the band-fitting method [40]. In this chapter, however, we will discuss only those methods, which were used in present thesis, and namely, the dimer projection and energy splitting methods [41].

Let us consider a charge transport process between two monomers, labeled as A and B, respectively. Assuming that the frontier orbitals of the formed dimer result exclusively from the interaction of the frontier orbitals of monomers ϕ^A and ϕ^B, we can obtain the dimer orbitals and the energy levels by solving the following secular equation [41]:

$$\mathbf{HC} - E\mathbf{SC} = 0, \tag{2.16}$$

where **H** and **S** are, respectively, the Hamiltonian and the overlap matrices, defined as:

$$\mathbf{H} = \begin{pmatrix} e_A & J_{AB} \\ J_{AB} & e_B \end{pmatrix}, \qquad \mathbf{S} = \begin{pmatrix} 1 & S_{AB} \\ S_{AB} & 1 \end{pmatrix}, \tag{2.17}$$

with the following matrix elements:

$$e_i = \left\langle \phi^i \middle| \hat{H} \middle| \phi^i \right\rangle, \qquad J_{ik} = \left\langle \phi^i \middle| \hat{H} \middle| \phi^k \right\rangle, \qquad S_{ik} = \left\langle \phi^i \middle| \phi^k \right\rangle. \tag{2.18}$$

In general, the frontier orbitals of monomers are not orthonormal with respect to each other, and $\mathbf{S} \neq \mathbf{1}$. Therefore, it is convenient to transform the original secular equation into the standard eigenvalue problem, given by [36]:

$$\mathbf{H}^{eff}\mathbf{C} = E\mathbf{C}. \tag{2.19}$$

According to Löwdin [42], this transformation can be performed as follows:

$$\mathbf{H}^{eff} = S^{-\frac{1}{2}}\mathbf{H}S^{-\frac{1}{2}}. \tag{2.20}$$

After some mathematical manipulations, the final expression for the effective Hamiltonian can be written as:

$$\mathbf{H}^{eff} = \begin{pmatrix} e^{eff}{}_{A} & J^{eff}{}_{AB} \\ J^{eff}{}_{AB} & e^{eff}{}_{B} \end{pmatrix} = \begin{pmatrix} \varepsilon_A & t_{AB} \\ t_{AB} & \varepsilon_B \end{pmatrix}. \tag{2.21}$$

Here, the matrix element t_{AB} corresponds to the transfer integral in the Marcus equation and ε_i is the site energy, which are given by:

$$\begin{aligned} t_{AB} &= \frac{J_{AB} - \frac{1}{2}(e_A + e_B)S_{AB}}{1 - S^2{}_{AB}}, \\ \varepsilon_i &= \frac{1}{2}\frac{1}{1 - S^2{}_{AB}}\left((e_A + e_B) - 2J_{AB}S_{AB}(e_A - e_B)\sqrt{1 - S^2{}_{AB}}\right). \end{aligned} \tag{2.22}$$

The parameter J_{AB} can be calculated by the direct numerical integration in real space as:

$$J_{AB} = \left\langle \phi^A \middle| \hat{H} \middle| \phi^B \right\rangle = \int \phi^A \hat{H} \phi^B d^3r. \tag{2.23}$$

However, the numerical integration is computationally inefficient, and it is convenient to represent the expression (2.23) in terms of the projections of the monomer orbital on the dimer orbitals. This transformation is done by introducing the unity operator,

$$\mathbf{1} = \sum_i |\psi_i\rangle\langle\psi_i|, \tag{2.24}$$

into the expression for J_{AB}:

$$\begin{aligned} J_{AB} &= \left\langle \phi^A \sum_i |\psi_i\rangle\langle\psi_i \middle| \hat{H} \middle| \sum_i |\psi_i\rangle\langle\psi_i| \phi^B \right\rangle \\ &= \sum_i \sum_i \left\langle \phi^A \middle| \psi_i \right\rangle \left\langle \psi_i \middle| \hat{H} \middle| \psi_i \right\rangle \left\langle \psi_i \middle| \phi^B \right\rangle, \end{aligned} \tag{2.25}$$

where the vector ψ_i designates the molecular orbitals of the dimer, and $\left\langle \phi^{A(B)} \middle| \psi_i \right\rangle$ represents the above mentioned projections, whose values can be determined as:

$$\left\langle \phi^{A(B)} \middle| \psi_i \right\rangle = \zeta^{A(B)} (\vartheta \zeta^{D}). \tag{2.26}$$

In the last expression, ζ and ϑ represent the expansion coefficients and overlap matrix of atomic orbitals, respectively.

In practice, however, it is quite common to use the energy splitting method [36], which is simply a ZINDO approximation of the dimer projection method. In this approach, it is assumed that the overlap between the orbitals of monomers can be neglected and the difference of the eingenvalues of the effective Hamiltonian corresponds to the energy splitting between HOMO and HOMO-1 (or, for electron transfer, LUMO and LUMO+1) levels of the dimer:

$$\Delta E = \sqrt{(\varepsilon_A - \varepsilon_B)^2 + (2t_{AB})^2}. \tag{2.27}$$

This enables to express the values of transfer integral as:

$$t_{AB} = \frac{1}{2}\sqrt{(\Delta E)^2 - (\varepsilon_A - \varepsilon_B)^2}. \tag{2.28}$$

The energy splitting method was verified against the dimer projection method a number of times, and the results provided by both methods are, generally, in a good qualitative agreement (see [36] and references therein). It is also should be noted that some authors go even further and approximate the site energy difference to be zero. This approximation, however, is rather crude, since even if the geometries of both monomers are identical, the dimer has to be symmetrical, e.g. to have an inversion center, to exclude the polarization effect. This statement also indicates that in general case the information, coming from each monomer as well as from the dimer, is required, and, hence, three quantum chemical calculations need to be carry out to predict a single transfer integral.

Increasing the number of calculations by a factor of three may seem to be unattractive in case of large systems, where many thousands of transfer integrals are needed to be calculated. However, the possibility to obtain the site energy difference together with the values of transfer integral, which is difficult to compute with the other methods, represents an important advantage of the dimer projection method. On the other hand, this difference corresponds to the conformational changes in conjugated segments, whereas under the device operation

conditions some additional contributions to the site energies, such as the build-in field and the Coulombic interactions between the free charges, also have to be accounted. More details, related to calculations of site energies, can be found within chapter 4.3.

2.5 Reorganization energy

The reorganization energy is the last unconsidered parameter which needs to be determined for the calculation of charge transfer rate between two states within the Marcus theory. Formally, this value corresponds to the free energy, required to change the molecules involved and the environment from the equilibrium configuration of reactant to the equilibrium configuration of products, staying on the same diabatic surface [43]. In the limit of high temperatures, the classical reorganization energy, λ, can be defined in terms of spectral density function, $J(w)$, as:

$$\lambda = \frac{2}{\pi}\int_0^\infty dw \frac{J(w)}{w}, \tag{2.29}$$

where w is the angular frequency. The spectral density function can be computed from molecular simulations as the cosine transform of the autocorrelation function, $c(t)$, of the vertical energy gap, $\Delta E = E_B - E_A$, sampled in the reactant state, A:

$$\frac{J(w)}{w} = \frac{1}{2k_B T}\int_0^\infty dt c(t)\cos(wt), \tag{2.30}$$

$$c(t) = \left\langle \delta\Delta E(0)\delta\Delta E(t)\right\rangle_A, \tag{2.31}$$

where $\delta\Delta E(t) = \Delta E(t) - \left\langle \Delta E\right\rangle_A$ refers to the usual canonical ensemble average. The energy gap is equal to the vertical potential energy between the two diabatic states A and B.

The more rigorous approach to estimate the reorganization energy is to split the value into two contributions: the contribution λ_i, coming from the molecules which are directly involved into the transfer ("inner shell"), and the contribution λ_o, coming from the changes in the environment ("outer shell") [44]:

$$\lambda = \lambda_i + \lambda_o. \tag{2.32}$$

The inner shell contribution to the reorganization energy for the charge transfer between two molecules M_1 and M_2 can be computed by using quantum chemical calculations. According to the Fig. 2.1 the charge transport process is split into two parts: (a) vertical charge transfer, obeying the Franck-Condon principle, and (b) the system relaxation to the equilibrium state. Consequently, the inner shell reorganization energy can be represented as:

$$\lambda_i = \lambda_i(M_1) + \lambda_i(M_2). \tag{2.33}$$

The contributions $\lambda_i(M_1)$ and $\lambda_i(M_2)$ can be determined by performing four single point quantum chemical calculations, which provide: (i) the energy of the neutral donor molecule in the optimized geometry for the charged molecule, (ii) the energy of the neutral donor molecule in the optimized geometry for the neutral molecule, (iii) the energy of the charged acceptor molecule in the optimized geometry for the neutral molecule, (iv) the energy of the charged acceptor molecule in the optimized geometry for the charged molecule. In case, where the molecules M_1 and M_2 are identical, the resulting value of inner shell reorganization energy corresponds to twice the polaron binding energy [45]. At the same time, due to the high density and viscosity of the polymers under investigation, significant changes in the environment are not expected and outer shell contribution can usually be neglected [46].

2.6 Dynamical Monte Carlo and First Reaction Method

Till now, we have only considered the theories of exciton- and charge-transport without specification of their use. Now, let us show how these theories can be coupled to each other to characterize the performance of OPV. In this thesis the coupling is achieved by application the dynamical Monte Carlo (DMC) approach, which is based on the concept of Markov chain [47].

The Markov chain in probabilistic theory can be considered as the analogue of the trajectory in classical mechanics, however, whereas in classical mechanics, the evolution of the system at $t + \Delta t$ depends on ($\mathbf{r}$ (t), $\mathbf{p}$ (t)), in stochastic dynamics this evolution depends only on $\mathbf{r}$ (t). Formally, a sequence of successive events $\mathbf{r}_0 \ldots \mathbf{r}_i \ldots \mathbf{r}_{N-1}$ is Markovian, if the

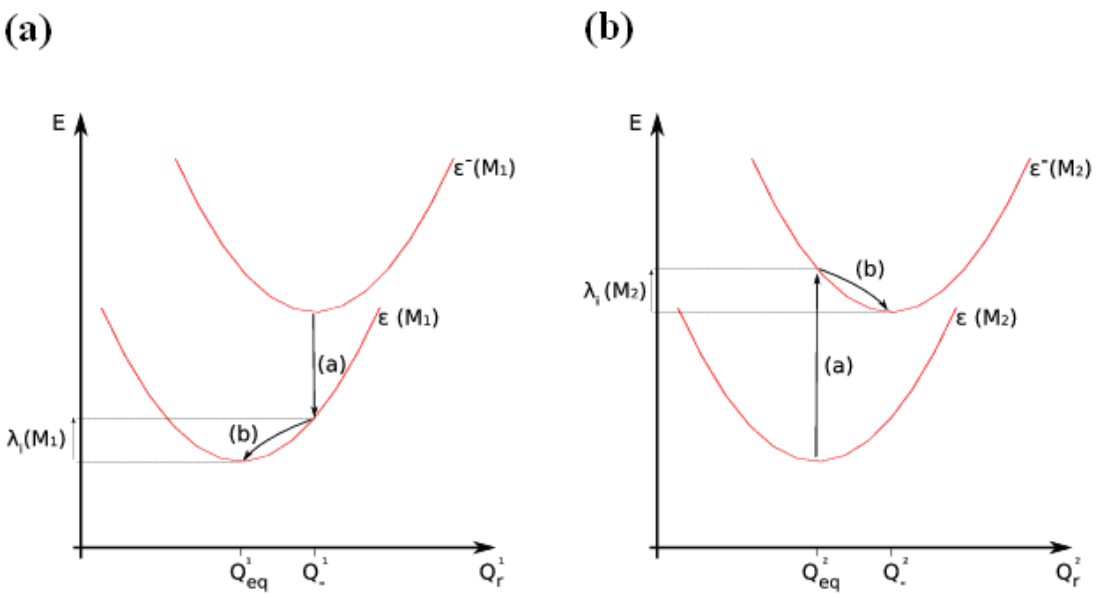

Fig. 2.1:Schematic diagram describing the energy changes for the (a) donor molecule and (b) acceptor molecule, involved in the charge transfer reaction.

probability to obtain event $\mathbf{r}_N$ only depends on $\mathbf{r}_{N-1}$:

$$k(\mathbf{r}_N \mid \mathbf{r}_0,\ldots,\mathbf{r}_i,\ldots,\mathbf{r}_{N-1}) = k(\mathbf{r}_N \mid \mathbf{r}_{N-1}). \tag{2.34}$$

As a consequence, the probability to have the successive events $P(\mathbf{r}_0\ldots\mathbf{r}_i\ldots\mathbf{r}_{N-1})$ can be expressed as:

$$P(\mathbf{r}_0,\ldots,\mathbf{r}_i,\ldots,\mathbf{r}_N) = P(\mathbf{r}_0)k(\mathbf{r}_1 \mid \mathbf{r}_0)k(\mathbf{r}_2 \mid \mathbf{r}_1)\ldots k(\mathbf{r}_N \mid \mathbf{r}_{N-1}), \tag{2.35}$$

where $P(\mathbf{r}_0)$ is the probability to be initially in the configuration $\mathbf{r}_0$ and

$$k\left(\mathbf{r}_j \mid \mathbf{r}_i\right) \equiv k\left(\mathbf{r}_i \to \mathbf{r}_j\right) = k_{ij}, \tag{2.36}$$

The second requirement for a Markov chain is the existence of a unique distribution of states, which leads to a coherent calculation of the physical properties. To ensure this, all possible configurations of the system must be achievable in finite time. This requirement is called ergodicity [47].

Finally, the system must obey the detailed balance condition [48], which is equivalent to the condition of microscopic reversibility of the system:

$$P(\mathbf{r}_j)k_{ji} = P(\mathbf{r}_i)k_{ij}. \tag{2.37}$$

The exciton and charge transport in organic semiconductors can be described by solving the Pauli Master equations [49]. A suitable tool for solving these equations is the DMC

algorithm, existing in several versions. For the purposes of this thesis we employed the first reaction method (FRM).

The FRM implies that all possible events are stored in a queue in order of ascending waiting times [50]. At each simulation step, the event with the smallest waiting time at the onset of the queue is chosen and carried out. Finally, this event is removed from the queue and the simulation time is incremented by the respective waiting time.

The algorithm of the FRM, implemented in this thesis, includes the following steps:

1. **Initialization**:

   At this step we are setting the convergence criteria and defining the initial value of time to be zero

2. **Calculation of waiting times**:

   Waiting times for all possible events for the local configuration are calculated as:

   $$\Delta t = -\frac{1}{w}\ln R, \tag{2.40}$$

   where w is a reaction rate and R is an uniformly distributed random number, $R \in (0;1]$.

3. **Execution of the event**:

   The event with the smaller waiting time is executed and the corresponding configuration changes are applied. The local time, t^i, is updated as given:

   $$t^{i+1} = t^i + \Delta t, \tag{2.41}$$

   where i is an iteration number.

4. **Convergence check**:

   If the deviations in the calculated values of the properties of interested are smaller than the predefined error, the simulation ends and the obtained values are considered to be the equilibrium ones. If not – the algorithm is repeated starting with step 2, until the convergence criteria is fulfilled.

3. Dynamics of polymer chains in organic photovoltaic devices

In following sections we introduce the SCFT formalism, which is used in this thesis for the description of the polymer phase separation process. Here, we start with the description of the models, applied in the approach to characterize the behavior of single polymer chains and, then, we show how SCFT treats different polymer mixtures of interest, namely, homo-polymer blends and block-copolymers. Furthermore, we describe the algorithm for determining the numerical SCFT solution. The last section deals with the problem of coupling the SCFT and previously described dynamical Monte Carlo algorithm.

3.1 Self-consistent field theory

3.1.1 Ideal Gaussian chain models

Let us consider a system composed of linear homopolymeric chains in a homogeneous environment and imply, for the moment, that all monomer-monomer interactions, including the short-range repulsive interactions, can be neglected. If the molecular weights of these molecules are high enough, all such polymers can be universally classified as non-avoiding random walks which show a degree of common properties, in particularly, scaling behavior of the size of polymer molecules with respect to the increase of their molecular weights [51]. To investigate this behavior, it is usually sufficient to apply some simple artificial models, which do not explicitly take into account the real chemical composition of polymeric segments. The first of these simple models, which is of interest for our consideration, is the freely-jointed Gaussian chain model.

The freely-jointed chain implies that each monomer within the polymer chain has a fix length, b, and the joints between the sequential monomers are completely flexible, i.e. the probabilities to find the polymer chain in any particular conformation are equal to each other. Such a chain can be generated by starting at one polymer end and attaching the monomers one by one with respect to the following probability:

$$p(r_i) = \frac{\delta(r_i - b)}{4\pi b^2}, \tag{3.1}$$

where δ represents the Dirac delta function and ensures that the monomer has a length, *b*, whereas the denominator comes from the normalization criteria. The size of the chain in any particular configuration can be described by the length of the end-to-end vector:

$$\mathbf{R} \equiv \sum_{i=1}^{M} \mathbf{r}_i. \tag{3.2}$$

The length of this vector is averaged over all possible conformations and can be used as a measure of the polymer size. In practice, it is usual to calculate the root-mean-square of the length vector:

$$R_0 \equiv \sqrt{\langle R^2 \rangle} = \sqrt{\left\langle \sum_{i,j} r_i \cdot r_j \right\rangle} = bM^{1/2}, \tag{3.3}$$

where *M* is a number of monomers in the chain. The last equality in eq. (3.3) comes from the fact that $\langle r_i \cdot r_j \rangle = 0$ for all $i \neq j$, since the monomers are considered to be uncorrelated. This power-law dependence is universal for all non-avoiding random walks and may differ from one model to another only in the proportionality constant, which in this case is equal to *b*.

Now, let us switch to the mesoscopic scale, where the polymers are viewed as a number of repeated coarse-grained segments. For this, the new probability distribution functions are defined though the end-to-end vector of segments, **r**, where each of them contains *m* monomers. These functions contain the information regarding the mesoscopic degrees of freedom and can be numerically evaluated in a recursive manner according the following equations:

$$p_m(\mathbf{r}) = \int d\mathbf{r}_1 d\mathbf{r}_2 p_{m-n}(\mathbf{r}_1) p_n(\mathbf{r}_2) \delta(\mathbf{r}_1 + \mathbf{r}_2 - \mathbf{r}), \tag{3.4}$$

where *n* is a positive integer, which is less than *m*.

The procedure of combining m monomers into larger units (in this case, segments), where the number of particles presented in the system is reduced down to N=M/m, is generally called coarse-graining. As a result, this routine replaces the *M* and *b* by N and statistical segment length, *a*:

$$a \equiv R_0 N^{-1/2} = bm^{1/2}, \tag{3.5}$$

where R_0 is defined such as $R_0 = aN^{1/2}$.

It is important to note that when the number of monomers in a segment is high enough (in limit, m → ∞), the probability distributions achieve the asymptotic limit of the Gaussian distribution:

$$p_m(r) \to \left(\frac{3}{2\pi a^2}\right)^{3/2} \exp\left(-\frac{3r^2}{2a^2}\right). \tag{3.6}$$

A second important model is the discrete Gaussian chain model, in which the oscillations of the bond lengths between the coarse-grained segments are described by the harmonic potential [52]. For this model, a single chain partition function is given by:

$$Z_0 = V(\int d\mathbf{b} \exp[-\beta h(|\mathbf{b}|)])^N, \tag{3.7}$$

where $h(x) = 3k_B T x^2 / (2b^2)$. The probability functions in turn can be described by Chapman-Kolmogorov equation [53]:

$$p_0(\mathbf{r}, j) = \int d\mathbf{b}_j \Phi(\mathbf{b}_j; \mathbf{r} - \mathbf{b}_j) p_0(\mathbf{r} - \mathbf{b}_j, j-1), \tag{3.8}$$

where $\Phi(\mathbf{b}_j; \mathbf{r} - \mathbf{b}_j)$ is a conditional probability density, which in absence of external fields tends to the Gaussian distribution.

Finally, for both analytical and numerical calculations of interest is the extension of the discrete Gaussian chain model, which is called the continuous Gaussian chain model. In this model, the polymers are viewed as a continuous, linearly elastic filament. Here, the coarse-grained trajectory may be specified by a function, **r** (*s*), where the parameter, $0 \le s \le 1$, runs over the polymer backbone such that the equal intervals of *s* have equal molecular weight. Generally, the continuous and discrete Gaussian chain models share the same chain and distribution function. However, the important advantage of the continuous model is that the equations for the probability calculation can be reduced to Fokker-Planck partial differential equations, for which a variety of numerical and analytical solution techniques is available [54, 55].

3.1.2 Gaussian chain in external field

In previous chapter we deal with a situation, when the forces, exerting on a polymeric chain, are neglected. Now, let us consider a case, when the polymers do experience interactions, which, in turn, may vary with respect to the position, **r**. In the field-based approach, these interactions are described by one or several potential fields, acting on the individual segments of a polymer chain, generally treated as "external". However, the fields of primary importance here are those that are generated self-consistently from the interactions with surrounding polymer segments [56].

The potential energy of a single chain in external field can be written as:

$$\begin{aligned} U(\mathbf{r}^{N+1}) &= U_0(\mathbf{r}^{N+1}) + U_1(\mathbf{r}^{N+1}) \\ &= \sum_{i=1}^{N} h(|\mathbf{r}_i - \mathbf{r}_{i-1}|) + k_B T \sum_{i=0}^{N} w(\mathbf{r}_i), \end{aligned} \tag{3.9}$$

where $\mathbf{r}^{N+1}$ is a coordinate vector. The second term in the expression accounts the interaction energy of each bead with the potential field $k_B T\, w(\mathbf{r})$ and can be expressed as:

$$\beta U_1(\mathbf{r}^{N+1}) = \int d\mathbf{r}\, w(\mathbf{r})\hat{\rho}(\mathbf{r}), \tag{3.10}$$

where $\hat{\rho}(\mathbf{r})$ is a microscopic density of segments, which is defined as follows:

$$\hat{\rho}(\mathbf{r}) = \sum_{i=0}^{N} \delta(\mathbf{r} - \mathbf{r}_i). \tag{3.11}$$

Furthermore, it is useful to define the ratio between the partition functions for the chain, placed in external field and the one for the ideal chain:

$$Q[w] \equiv \frac{Z[w]}{Z_0} = \frac{\int d\mathbf{r}^{N+1} \exp[-\beta U(\mathbf{r}^{N+1})]}{V(\int d\mathbf{b} \exp[-\beta h(|\mathbf{b}|)])^N}. \tag{3.12}$$

This ratio can be determined by using the definition of the normalized bond transition probability, given as:

$$\Phi(\mathbf{r}) = \frac{\exp[-\beta h(|\mathbf{r}|)]}{\int d\mathbf{r} \exp[-\beta h(|\mathbf{r}|)]} = \left(\frac{3}{2\pi b^2}\right)^{3/2} \exp\left(-\frac{3|\mathbf{r}|^2}{2b^2}\right). \tag{3.13}$$

As a result, the normalized partition function can be expressed as:

$$Q[w] = \frac{1}{V}\int d\mathbf{r} q(\mathbf{r}, N; [w]), \tag{3.14}$$

where

$$q(\mathbf{r}, 0; [w]) = \exp[-w(\mathbf{r})], \tag{3.15}$$

and

$$q(\mathbf{r}, j+1; [w]) = \exp[-w(\mathbf{r})]\int d\mathbf{r}' \Phi(\mathbf{r} - \mathbf{r}') q(\mathbf{r}', j; [w]). \tag{3.16}$$

Here, $q(\mathbf{r}, 0; [w])$ refers to the statistical weights for a chain of j+1 beads to have its end at position **r** and is commonly called a chain propagator.

For the continuous Gaussian chain model, the derivation scheme is similar, but with the condition that the microscopic segment density is changed to

$$\hat{\rho}(\mathbf{r}) = \int_0^N ds \delta(\mathbf{r} - \mathbf{r}(s)). \tag{3.17}$$

Finally, the propagators can be determined from the Fokker-Planck diffusion equation, given as:

$$\frac{\partial}{\partial s} q(\mathbf{r}, s; [w]) = \frac{b^2}{6}\nabla^2 q(\mathbf{r}, s; [w]) - w(\mathbf{r}) q(\mathbf{r}, s; [w]), \tag{3.18}$$

by using the initial condition

$$q(\mathbf{r}, 0; [w]) = 1. \tag{3.19}$$

3.1.3 Field-theoretical model of polymer blends

Now, let us show how a blend of homopolymers can be described in the frame of a field-theoretical approach. For this, we consider an incompressible mixture, which consists of n_A molecules of homopolymers of type A and n_B molecules of homopolymers of type B. Each of these K-type homopolymers has N_K statistical segments of length b_K, and an equal segment volume of v_0, where K corresponds to either A or B. Incompressibility in this case means that a sum of A and B segment densities is everywhere equal to $\rho_0 = 1/v_0$. The microscopic densities of K-type segments are defined as:

$$\hat{\rho}_K(r) = \sum_{i=1}^{n_K} \int_0^{N_K} ds\, \delta(r - r_i^K(s)). \tag{3.20}$$

The canonical partition function for the coarse-grained model of homopolymer blend can be written as:

$$\begin{aligned} Z_C(n_A, n_B, V, T) \propto & \frac{1}{n_A! n_B!} \prod_{j=1}^{n_A} \int D\mathbf{r}_j \prod_{k=1}^{n_B} \int D\mathbf{r}_k \\ & \times \exp(-\beta U_0[r^{n_A N_A + n_B N_B}] - \beta U_1[r^{n_A N_A + n_B N_B}]) \\ & \times \delta[\hat{\rho}_A + \hat{\rho}_B - \rho_0], \end{aligned} \tag{3.21}$$

where U_0 corresponds to the intermolecular short-range energetic contributions, and δ-function ensures the incompressibility condition.

In order to represent this function in field theory, we first introduce the new microscopic densities $\hat{\rho}_+$ and $\hat{\rho}_-$, defined as follows:

$$\hat{\rho}_\pm = \hat{\rho}_A(\mathbf{r}) \pm \hat{\rho}_B(\mathbf{r}). \tag{3.22}$$

This redefinition enables to rewrite the delta function as $\delta[\hat{\rho}_+ - \hat{\rho}_0]$, and define the interaction term U_1 as:

$$\begin{aligned} -\beta U_1[r^{n_A N_A + n_B N_B}] &= \frac{1}{4} v_0 \chi_{AB} \int d\mathbf{r}([\hat{\rho}_+(\mathbf{r})]^2 - [\hat{\rho}_-(\mathbf{r})]^2) \\ &= \frac{1}{4} v_0 \chi_{AB} \int d\mathbf{r}([\hat{\rho}_0{}^2 - [\hat{\rho}_-(\mathbf{r})]^2), \end{aligned} \tag{3.23}$$

where χ_{AB} is a Flory-Huggins interaction parameter. The quadratic interactions in $\hat{\rho}_-$ can be decoupled by means of the Gaussian functional integral:

$$e^{-\beta U_1} = e^{-\chi_{AB}(n_A N_A + n_B N_B)/4} \int Dw_- e^{\int d\mathbf{r}[\hat{\rho}_- w_- - (\rho_0/\chi_{AB}) w_-^2]}. \tag{3.24}$$

The delta function in turn can be written in exponential representation as:

$$\delta[\hat{\rho}_+ - \rho_0] = \int Dw_+ e^{-i\int d\mathbf{r} w_+(\hat{\rho}_+ - \rho_0)}. \tag{3.25}$$

By substituting eq. 3.24 and 3.25 into the eq. 3.21, we obtain the field-theoretic representation of the canonical partition function:

$$Z_C(n_A, n_B, V, T) = Z_0 \int Dw_+ \int Dw_- \exp(-H[w_+, w_-]), \tag{3.26}$$

with the effective Hamiltonian, given by:

$$H[w_+, w_-] = \rho_0 \int dr[(1/\chi_{AB})w^2_- - iw_+] \\ -n_A \ln Q_A[w_A] - n_B \ln Q_B[w_B]. \tag{3.27}$$

The fields w_K are defined as follows:

$$w_A \equiv iw_+ - w_-, \quad w_B \equiv iw_+ + w_-. \tag{3.28}$$

The single chain partition function Q_K is given by:

$$Q_K[w_K] = \frac{1}{V}\int d\mathbf{r} q_K(\mathbf{r}, N_K; [w_K]), \tag{3.29}$$

and the propagators, q_K, are derived from the following diffusion equations:

$$\frac{\partial}{\partial s} q_K(\mathbf{r}, N_K; [w_K]) = \left[\frac{b^2_K}{6}\nabla^2 - w_K(\mathbf{r})\right] q_K(\mathbf{r}, N_K; [w_K]). \tag{3.30}$$

Finally, the segment density operator can be computed as follows:

$$\hat{\rho}_K(\mathbf{r}; [w_K]) = -n_K \frac{\partial \ln Q_K[w_K]}{\partial w_K(\mathbf{r})} \\ = \frac{n_K}{VQ_K[w_K]} \int_0^N ds\, q_K(\mathbf{r}, N_K - s; [w_K]) q_K(\mathbf{r}, s; [w_K]). \tag{3.31}$$

3.1.4 Field-theoretical model of block-copolymers

Whereas the application of polymer blends represents the “classical” technology for fabrication of organic solar cells, there is an alternative strategy, based on the block-copolymers. Despite of the higher production costs, these materials permit to decrease the domain size to the order of exciton diffusion length, what significantly improves the exciton dissociation efficiency. Another advantage of this technology is that the block copolymers are able to form lamellar-like structures, what enables efficient charge delivery to the appropriate electrodes with minimum losses [57]. This approach is relatively new [58], and there is still a lot of room for improvement the performance of the devices. However, already now many authors expect a drastic change in solar cells efficiency, associated with the use of block-copolymers.

From the viewpoint of the field-theory, a treatment of block copolymers represents an extension of the model for linear homopolymer blends, which we have already discussed in chapter 3.1.3. The difference between these two models is that in the block copolymer mixtures only one type of polymeric chains is presented in the systems. Consequently, there is only one single-chain partition function $Q_K[w_A, w_B]$, which can be described as:

$$Q_K[w_A, w_B] = \frac{1}{V}\int d\mathbf{r} q_K(\mathbf{r}, N_K; [w_A, w_B]). \tag{3.32}$$

The canonical partition function has a similar form as the one for the homopolymer blend in eq. (3.21), but with the different effective Hamiltonian, which is given by:

$$H[w_+, w_-] = \rho_0 \int dr[(1/\chi_{AB})w^2_- - iw_+] - n\ln Q[w_+, w_-]. \tag{3.33}$$

Despite the fact that the equations for homopolymer blend and block copolymers look very similar, the single-chain partition function for block-copolymers has a significantly different non-local character than those for the blend [56]. This difference arises from the presence of a covalent bond between A and B monomers, and, as a result, influences the microphase separation, as shown in Fig. 3.1.

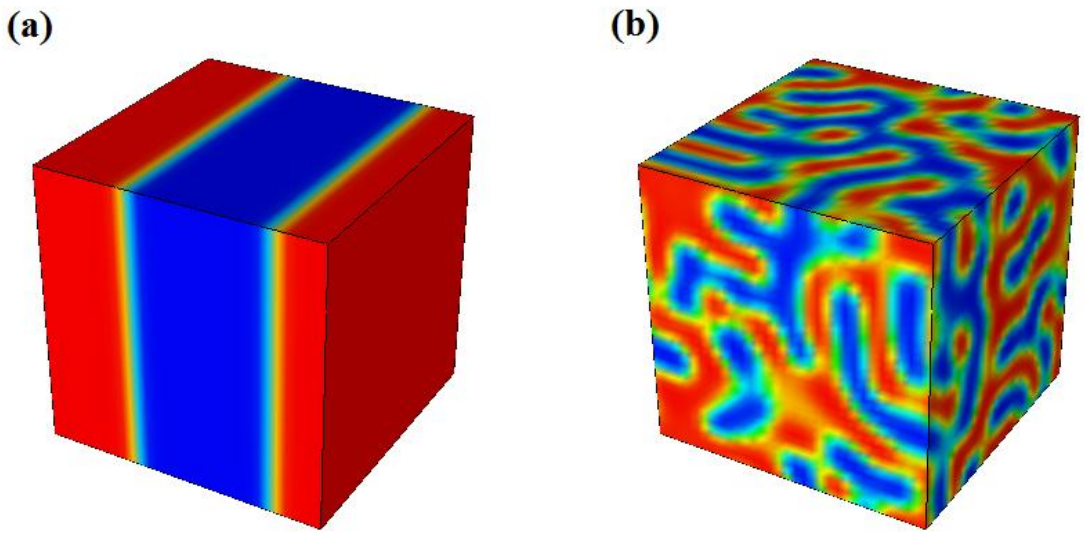

Fig. 3.1 Volume fraction profile obtained with $\chi_{AB}N = 8$ and $L_x = L_y = L_z = 32\,b$ for a) symmetric homopolymer blend and b) symmetric diblock copolymer. Red regions correspond to the majorities of component "A", while the blue ones – to the majorities of component "B".

3.1.5 General strategy for determining an SCFT solution

The field-theoretic models generally express the partition function as an integral over one or several potential fields $w(r)$

$$Z = \int Dw \, \exp(-H[w]), \tag{3.34}$$

where $H[w]$ is an effective Hamiltonian, which depends on the polymeric structure and molecular weight. An ensemble average of some observable value, A, is given by:

$$\langle A[w] \rangle = Z^{-1} \int Dw \, A[w] \exp(-H[w]), \tag{3.35}$$

whose direct evaluation requires the calculation of the partition function by using eq. (3.34). In practice, however, none of these integrals can be evaluated in closed form. One of the possibilities to solve these integrals is to apply some analytical approximations, which simplify the theory, and, then, evaluate the quantity of interest either analytically or numerically.

In this context, the most important approximation technique is the mean-field approximation, which can be calculated by using the SCFT technique. In this approach, it is assumed that a single field configuration $w^*(r)$ dominates the functional integrals in eqs. (3.34) and (3.35) [56], resulting in:

$$Z \approx \exp(-H[w^*]), \quad \langle A[w] \rangle \approx A[w^*]. \tag{3.37}$$

This field is obtained self-consistently by demanding that the Hamiltonian remains stationary with respect to the variations in $w(r)$:

$$\left. \frac{\delta H[w]}{\delta w(r)} \right|_{w=w^*} = 0. \tag{3.36}$$

The solutions of eq. (3.36) are generally called the saddle points. One of the approaches to find these saddle points is to view SCFT as a nonlinear optimization problem, in other words, to find the field configurations $w(r)$ that are extrema of the effective Hamiltonian. There are many different strategies for solving the nonlinear optimization problems, such as, for example, conjugated gradients method [56]. The most straightforward method, used in practice, is the explicit Euler scheme [59].

In order to generate the mean-field solution for eq. (3.36), it is useful to approximate the field $w^*(r)$ by a M-component vector $\mathbf{w}^* = (w_1^*, w_2^*, ..., w_M^*)^T$, representing the values of the field at certain lattice points. Moreover, it is expected that $\mathbf{w}^*$ is purely imaginary. Therefore, it is convenient to define a purely real vector $\boldsymbol{\mu} \equiv i\mathbf{w}^*(r)$, and determine already its values. With respect to the vector $\boldsymbol{\mu}$, the explicit Euler scheme assumes the following optimization algorithm:

$$\frac{\partial}{\partial t}\mu(r,t) = \lambda \frac{\partial H[\mu]}{\partial \mu(r,t)}, \tag{3.38}$$

where λ is a relaxation parameter. Using the effective Hamiltonian for the polymer blend model 3.1.3, eq. (3.38) can be modified as follows:

$$\begin{aligned} \boldsymbol{\mu}^{i+1}{}_{+} &= \boldsymbol{\mu}^{i}{}_{+} + \Delta t \lambda_{+}[\boldsymbol{\rho}_A(w^{i}{}_A) + \boldsymbol{\rho}_B(w^{i}{}_B) - \rho_0 \mathbf{e}] \\ \boldsymbol{\mu}^{i+1}{}_{-} &= \boldsymbol{\mu}^{i}{}_{-} - \Delta t \lambda_{-}[-\boldsymbol{\rho}_A(w^{i}{}_A) + \boldsymbol{\rho}_B(w^{i}{}_B) + \frac{2\rho_0}{\chi_{AB}}\boldsymbol{\mu}^{i}{}_{-}], \end{aligned} \tag{3.39}$$

where $\boldsymbol{\mu}_{+} \equiv i\mathbf{w}_{+}$, $\boldsymbol{\mu}_{-} \equiv \mathbf{w}_{-}$, which are used due to the slow convergence of the direct solution of eq. (3.38) near to $\boldsymbol{\mu}^{*}{}_{\pm}$. Therefore, the Euler scheme requires only the recalculation of segment density operator, achieved by solving the Fokker-Planck equations, given by eq. (3.30). The complete procedure for determining an SCFT solution, schematically depicted in Fig. 3.2, includes the following steps:

1. Set the initial values of the parameters $\boldsymbol{\mu}_{+}$, $\boldsymbol{\mu}_{-}$, and Δt;
2. Calculate the value of single chain partition function by solving the Fokker-Planck equations;
3. Compute the microscopic densities and polymer volume fractions;
4. Convergence check: if convergence is not reached, update the external field and repeat the steps (2)-(4); otherwise finish the simulations.

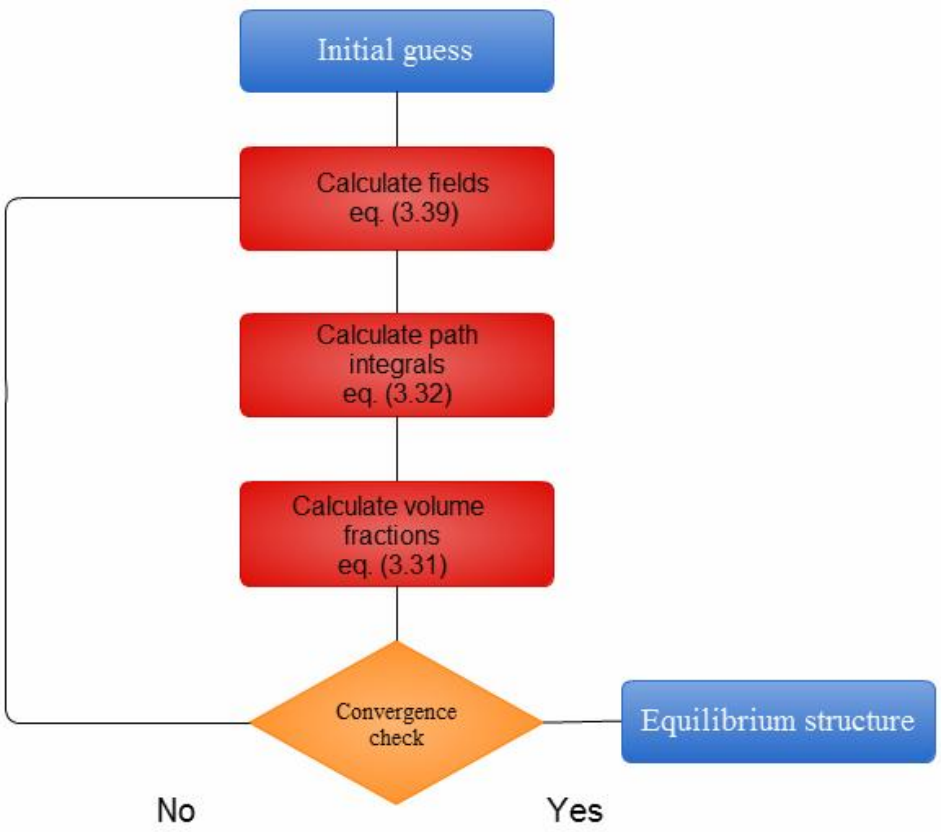

Fig. 3.2: Schematic representation of the procedure for determining an SCFT solution

3.2 Density biased Monte Carlo method

In order to investigate the influence of intermolecular mixing on the photovoltaic performance, the mesoscopic morphology needs to be transformed into the atomistic representation, which can be achieved by using the density biased Monte Carlo method [60]. In this approach, the generation of the respective atomistic morphology is based on the computed values of segment volume fractions, which are thought of as probabilities to find the *i*-th segment at a certain position **r**. More specifically, the procedure consists of the following steps [60]:

1. The first segment of a chain is placed by randomly choosing a point **r** within the simulation box, and the local volume fraction $\varphi_i(\mathbf{r})$ for the first segment is then compared to a random deviate p uniformly distributed in the interval [0,1). If $p \leq$

$\varphi_i(\mathbf{r})$, the segment is positioned at **r**; otherwise the step is repeated until an acceptable chain origin is obtained.

2. Assuming that the *i*-th segment of the chain has been placed at **r**', we randomly select a point **r** on the sphere $|\mathbf{r}-\mathbf{r}'|=a$, where *a* is the segmental length defined previously. As before, the (*i*+1)-th monomer is placed at **r** if $p \leq \varphi_{i+1}(\mathbf{r})$; otherwise the step is repeated until a statistically valid position for the (*i*+1)-th segment is obtained.
3. The steps 2 and 3 are repeated until the desired number of chains is placed within the simulation cell.

In Fig. 3.3 we show an example of the application of density biased Monte Carlo method to the morphology, obtained with the SCFT method. By analyzing the Figs. 3.3 (a) and (b) we can state that both mesoscopic and atomistic morphologies describe the same space separation of the polymeric chains. However, we note that the density biased Monte Carlo method does not contain a procedure to avoid the overlaps between the segments, arising from the lack of knowledge of the previously placed segment's positions. According to Sewell at al., this

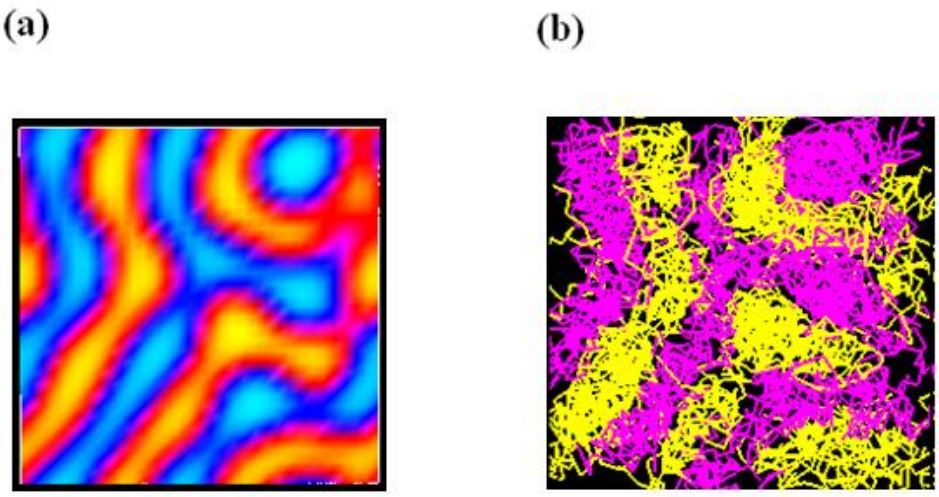

Fig. 3.3: Schematic illustration of the density biased Monte Carlo procedure: (a) mesoscopic morphology, obtained with the SCFT method (b) the atomistic representation of the same morphology, obtained by using density biased Monte Carlo method.

disadvantage can be overcome by including into the algorithm the excluded volume effect [61] or, alternatively, as we did it, by introducing the intermolecular interaction potentials between the monomers and equilibrating the system with the tools of molecular dynamics. The computational details of the second method can be found within chapters 5 and 6.

Results and discussion

4. Development and application of a novel multiscale simulation approach for studying the loss processes in polymer solar cell nanodevices

In the following chapters, we present our simulation approach for investigating the loss processes in organic photovoltaic devices. To this end, we start with the introduction of our DMC algorithm, which we apply to mimic the photovoltaic processes, occurring in the active layer of the solar cells. Then, we validate the implementation of our algorithm with excising experimental and theoretical data from the literature. Furthermore, we introduce the dynamical SCFT method, enabling to investigate the time evolution of the phase separation process. Then, we apply our simulation strategy to investigate the morphological effects in polymer-based solar cells. Finally, we demonstrate the predictive power of our algorithm by exploring the impact of the morphological defects, occurring within the phase separation process, on the photovoltaic properties of the corresponding devices at different degree of phase separation and various types of electric circuits.

4.1 State of the art of the algorithms for simulating the photovoltaic processes in organic solar cells

Most of the computer simulation approaches for investigating the photovoltaic behavior of solar cell devices are based on the drift-diffusion model [50, 62]. This model represents a continuum treatment of the system under investigation and enables the description of the charge carrier diffusion in the electric field under the energy gradient. The dynamic evolution of the model is obtained through the self-consistent solution of the continuity equations, which are usually coupled to the Poisson's equation to treat the electrostatic interactions. This approach has so far successfully been employed to investigate the photovoltaic behavior of inorganic materials and only recently has been adapted to organic devices. In the year 2003, Gregg and Hanna [50, 63] first demonstrated on a simple example the fundamental difference between inorganic and OPV-cell devices. In this work, they adapted the conventional one-dimensional drift-diffusion model of inorganic systems to the case of organic systems, where

the free charge carriers can only be generated at the DA interface. This technique enables the description of the diffusion of the charge carriers in polymer solar cells under the internal concentration gradients. However, it does not permit to take into account the generation, diffusion, and dissociation of the excitons. Barker *et al*. [50, 64] improved the drift-diffusion model for organic devices by explicitly incorporating the fraction of light, leading to charge separation at the DA interfaces, and could achieve in this way a good agreement with the experimental results. However, also in this model the exciton behavior was only included in an indirect way. In a further work Härter *et al*. [50, 65] considered a prototypical one-dimensional device with a broader DA-interfacial region, to study the consequences of blending on the solar cell performance. In the model they restricted the generation of electrons and holes to the interfacial region and allowed the charge carriers to migrate through the entire system by taking into account the existence of the interfaces. However, the effect of the morphology was here only included through a simple unidirectional change of the properties. Recently, Buxton and Clarke [50, 62, 66] developed a new simulation procedure on the basis of a two-dimensional drift-diffusion model to investigate the influence of the morphology on the photovoltaic behavior of phase-separated block-copolymer solar cells. In this technique the morphology of a diblock copolymer system is determined *a priori* with the mesoscopic Flory-Huggins-Cahn-Hilliard method, which relies on the mean-field (MF) approximation. The structural information is then used as input for the self-consistent solution of the continuity-transport equations for the electrons, holes, and excitons in conjunction with Poisson's equation. However, the general applicability of this method remains rather limited. On the one hand, the MF provides reliable information in the range of soft monomer interactions about the system, which makes the method applicable for a wide range of polymeric mixtures at low computational expense. On the other hand, the drift-diffusion model does not allow the explicit description of local particle processes, e.g., the loss processes of charge carriers through interaction with other charge carriers at bottlenecks and dead ends of the morphology. Thus, in the underlying continuum description of the system, local particle phenomena are only taken into account in an implicit way through the macroscopic parameters of the model [50].

4.2 Development of our algorithm for simulating the photovoltaic processes in organic solar cells

4.2.1 Development and implementation of the dynamical Monte Carlo algorithm

To explore the photovoltaic efficiencies of the OPV nanodevices, we developed an algorithm, reflecting the mechanism of the photocurrent generation in organic solar cells and, at the same time, allowing the explicit description of local particle processes. In our simulations, we considered three types of mobile particles, i.e., electrons, holes, and excitons. To describe the motion of these particles, we adopted the conventional DMC algorithm, presented in chapter 2.6. In Fig. 4.1 we visualize the structure of our algorithm, which we implemented in C language. According to this scheme, we start our simulations with a generation of exciton at the randomly chosen grid point inside the polymeric morphology. The diffusion of this exciton within the material may result either in the exciton dissociation at the DA interface with the formation of an electron and a hole or exciton decay. Once the exciton dissociation event has occurred, we proceed with the treatment of the charge motion. In our algorithm, depending on their local structural environment and situation the electron and hole can either move within the appropriate phases through a hoping process between the adjacent sites or annihilate through bimolecular charge recombination. In addition, we take into account the possibility of the charge collection in case, where the charges reach the first monolayer near to the appropriate electrode. In order to determine, which event will be selected, we compute the corresponding waiting times by using eq. (2.40) and store them to the event sequence. After the calculations of waiting times for all possible events, the event with the smallest waiting time is executed and removed from the queue of events. In our simulations, we allow exciton generated in both D- and A-phases with a constant rate, which is taken from experimental measurements, while the exciton decay rate is taken to be equal to the inverse value of the exciton life time. Moreover, we describe the exciton diffusion as a hopping process by using the Förster formalism, described in chapter 2.1. The hopping rate of

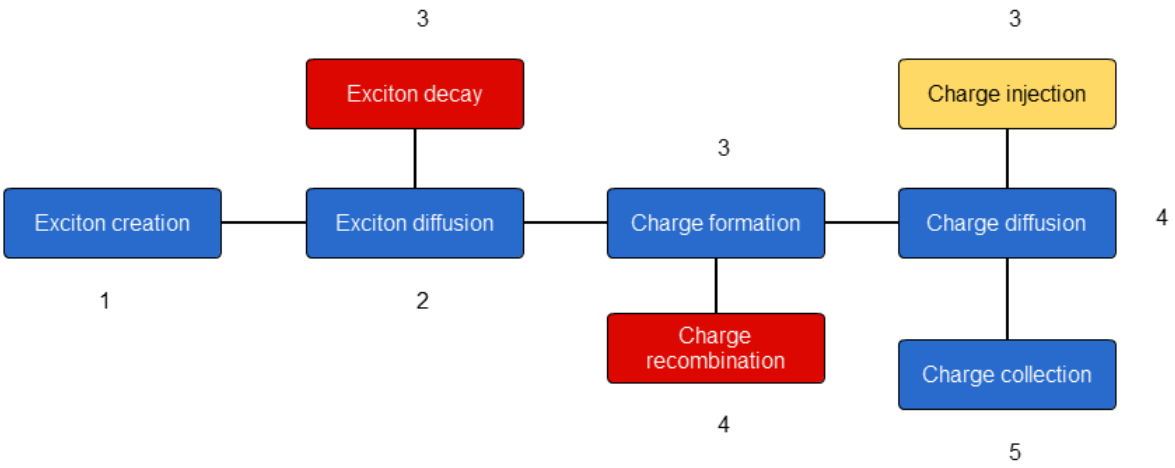

Fig. 4.1: Schematic representation of the developed DMC algorithm for simulating the photovoltaic processes in organic solar cells. The pathway through the blue rectangular blocks describes the mechanism of photocurrent generation in organic photovoltaic devices, while the red rectangular blocks indicate the possible sources of exciton and charge losses. The yellow rectangular block reflects an additional source of charges in the system, arising from the charge injections from the corresponding electrodes.

charge carriers is calculated by using the formula of the Marcus theory [67, 68]:

$$\omega_{ij} = V_{hop} \exp\left[-\frac{(E_i - E_j + \lambda)^2}{4\lambda k_B T} \right], \tag{4.1}$$

where E_i and E_j refer to the energies of hopping sites i and j, respectively, while λ is the reorganization energy corresponding to twice the polaronic binding energy [69].

The prefactor V_{hop} is obtained by using the Einstein relationship [67] and is given by

$$V_{hop} = \frac{6 k_B T \mu_{e/h}}{q a^2} \exp\left[\frac{\lambda}{4 k_B T} \right], \tag{4.2}$$

where $\mu_{e/h}$ is the mobility of the electrons/holes with charge q in both polymer species. The energy of the electron, created either by exciton dissociation or by injection, at the hopping site i is defined as [70]:

$$E_i = \varphi_w + \Delta_{inj} - eFx_i - \frac{e^2}{16\pi\varepsilon_0\varepsilon_r x_i}, \tag{4.3}$$

where φ_w represents the work function of the electrode, Δ_{inj} is the injection barrier, F is the net field, resulting from the built-in voltage and applied bias, x_i is the distance from the

contact, and *e* is the charge magnitude. The final term in eq. (4.3) takes into account the effect of the polarization of the polymers in presence of the electrodes (image charge effect). Note that an equivalent expression was used to describe the hole transport. To take into account the Coulombic interactions between the charge at site *i* with all other charges within the system, we added to the energy difference in eq. (4.3) the following contribution [70]:

$$\Delta E = \sum_{j=1}^{n} \frac{qe}{4\pi\varepsilon_0\varepsilon_r r_{ij}}, \tag{4.4}$$

where *n* is the total number of other charges in the system with $q = +e$ for electron-electron and hole-hole repulsion as well as $q = -e$ for electron-hole attraction, while ε_0 and ε_r describe the permittivity of vacuum and organic materials, respectively. Finally, to take into account the presence of the dark current, we include an additional step of charge injection from the electrodes to the corresponding phases inside the polymeric morphology. The rate of this process is determined with the Marcus theory by taking the value of the injection barrier, resulting from the difference between the Fermi level of the electrodes and the corresponding energy levels of the material, is taken as the energy change.

4.2.2 Validation of the dynamical Monte Carlo algorithm: Ising spin model

In order to verify the quality of our implementations, we reproduced the simulation results of Watkins *et al* [21], who first investigated the impact of the polymeric morphology on the efficiency of nanostructured polymer-based solar cells. In this approach, the morphology is represented as a set of Ising spins, whose distribution is associated with the phase separated morphology of donor- and acceptor-polymers. The interaction energy between the different kinds of spins is defined according to the Ising spin Hamiltonian, which for the energy of site i is given as

$$\varepsilon_i = -\frac{\mathrm{J}}{2} \cdot \sum_j \left(\delta_{\mathrm{s_i},\mathrm{s_j}} - 1 \right), \tag{4.5}$$

where $\delta_{\mathrm{s_i},\mathrm{s_j}}$ is the Kronecker delta-function, while $\mathrm{s_i}$ and $\mathrm{s_j}$ refer to the spins occupying the sites i and j, respectively. The simulation of the phase separation process starts with a configuration where two kinds of spins, which are designated either as spin-up or spin-down,

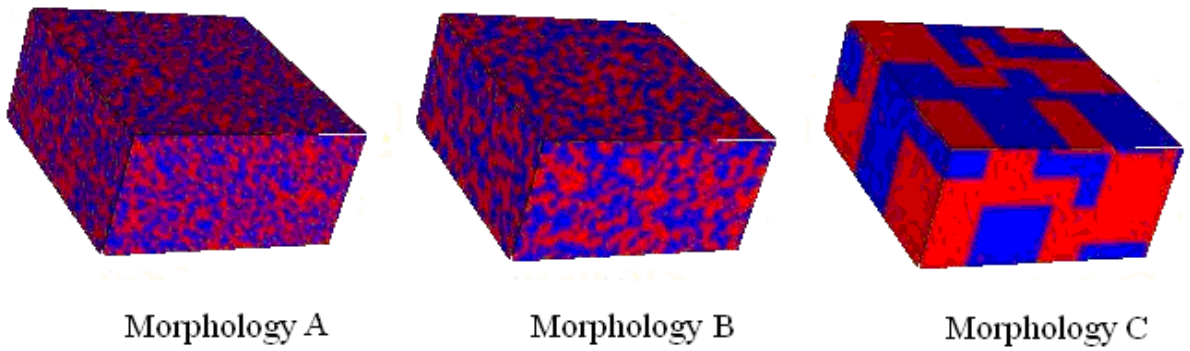

Fig. 4.2 Morphologies, obtained by treating the phase separation process of a mixture of D/A polymers with Ising spin model by using Kawasaki dynamics.

are randomly distributed over the corresponding lattice. In the next step, a random pair of neighboring spins is selected, and, under certain acceptance criteria, both spins may change their values to the opposite ones, e.g. a spin-up may become a spin-down and vice versa. Since the free energy of the system minimizes with the increase of the domain sizes, by the system evolves in time by providing a set of morphologies with the different degree of phase separation. This procedure is more generally known as Kawasaki dynamics.

In Fig. 4.2 we show the resulting morphologies, obtained for a coupling constant of J=1, at different degree of the phase separation process. In Fig. 4.3 we plot the corresponding results from DMC simulations, which are in perfect agreement with the results of Watkins *et al* [21]. As expected, at low interfacial area, corresponding to large-scale phase separation in morphology C, we observe that the internal quantum efficiency is limited by low exciton dissociation efficiency, representing the ratio of the number of dissociated excitons to the number of generated excitons. For such a morphology, the excitons tend to decay before reaching an interface without the formation of free charge. In this case, however, the charge transport efficiency, reflecting the ratio of the number of charge carriers exciting the device versus twice the number of the dissociated excitons, is nearly 100 %. This can be associated with the presence of continuous percolating pathways, enabling efficient delivery of generated charges to the electrodes. By contrast, at high interfacial area, i.e. in case of small-scale phase separation in morphology A, the situation is just the opposite: charge transport is limited by a small domain size, which causes the recombination of charges before they reach the electrodes, whereas there are almost no losses in exciton dissociation. As a result, a maximum

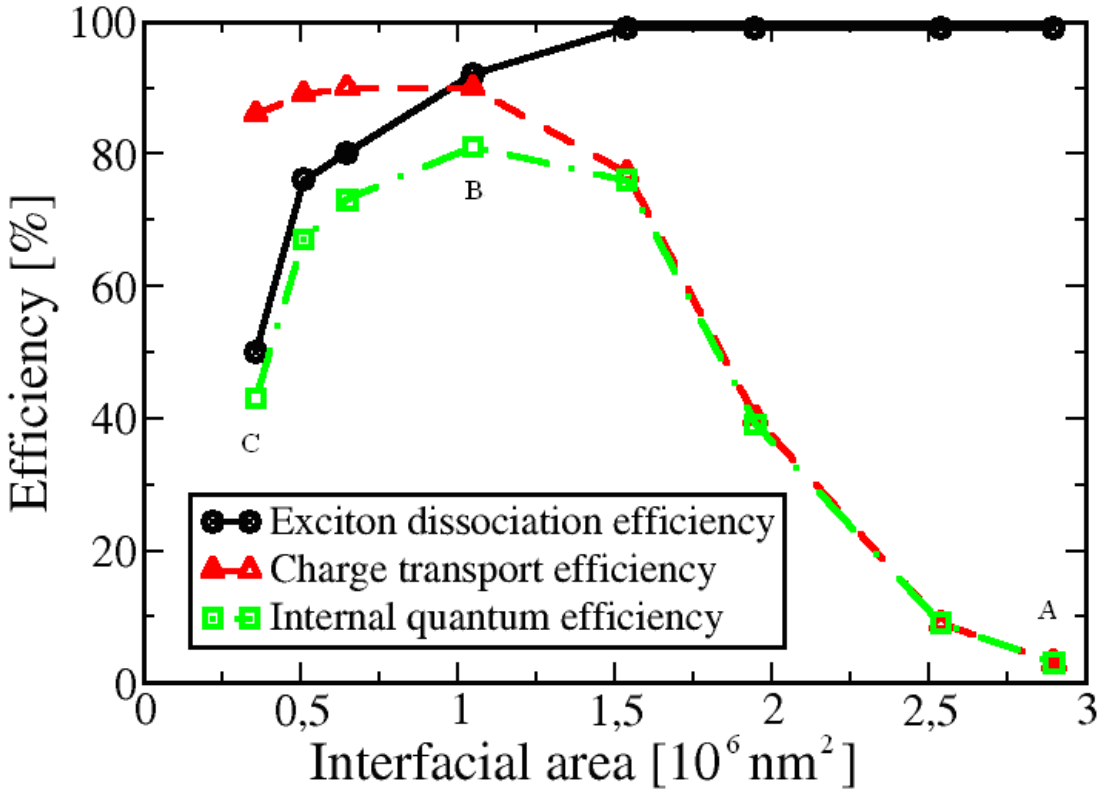

Fig. 4.3: EDE, CTE, and IQE as a function of interfacial area between DA domains, obtained from DMC simulations using the morphologies generated during the phase separation process with Ising spin Hamiltonian.

of internal quantum efficiency (Morphology B), which refers to the ratio of the number of charge carriers collected at the electrodes versus twice the number of generated excitons, is observed for the intermediate range of the interfacial area, corresponding to a optimal compromise between exciton dissociation and charge transport efficiencies.

By analyzing the results, obtained with the method of Watkins *et al*, we conclude that the Ising model useful results for the description of IQE behavior as a function of the interfacial length between the D/A domains. Moreover, it reliably describes the current-voltage characteristics in agreement with experiment measurements. However, a main disadvantage of this model is that it does not take into account the effects of polymer architecture and interactions during the phase separation process; in other words, it cannot answer the question which polymers should be used to obtain the respective morphology with the optimal solar cell performance. In order to account these effects, a more realistic polymer

model for the simulations of the phase separation process is required. The description of such a model will be a subject of the following chapters.

4.2.3 Dynamical SCFT approach for generating the nanoscale polymeric morphology

In this thesis, we introduce a novel simulation approach, which permits an explicit description of exciton- and charge-motion and, at the same time, enables to take into account the polymeric architecture and composition. To achieve this goal, we coupled the above mentioned DMC algorithm to the mesoscopic field-theoretic method, which was represented in chapter 3.1.5. However, we point out that the described SCFT technique is used to obtain the equilibrium morphology for a given polymer composition and does not allow to study the polymer phase separation process. To describe the dynamics of polymer phase separation, one uses the dynamical SCFT methods, which are based on the coupling of the SCFT algorithm to a time-dependent diffusion equation. The resulting technique represents a method to simulate diffusion dynamics of the polymeric segments driven by the gradient of the chemical potential, where the conformational entropy is taken into account through the path integral [71]. Depending on the type of the diffusion equation, the dynamical SCFT approach exists in several versions, however, in case of our simulation approach, we made use of the Ginzburg-Landau (TDGL) method [50, 72]. This method bases on the Cahn-Hilliard-Cook (CHC) nonlinear diffusion equation, which for an incompressible binary DA-polymer blend results in the following equation [50, 72, 73]:

$$\frac{\partial \phi(\mathbf{r},t)}{\partial t} = \nabla \cdot \left\{ M \nabla \frac{\delta F[\phi(\mathbf{r},t)]}{\delta \phi(\mathbf{r},t)} \right\} + \eta(\mathbf{r},t). \tag{4.6}$$

Here, $\phi(\mathbf{r},t)$ represents the local monomer concentration on a certain grid point **r**, M is the mobility coefficient, while η (**r**, t) corresponds to a thermal noise with a zero mean value and a variance, given by the fluctuation-dissipation theorem. For the calculation of the free energy of the polymer blend in eq. (4.6), the following equation has been used [50, 72]:

$$\frac{F[\phi(\mathbf{r},t)]}{k_B T} = \int d\mathbf{r} \left[\frac{f_{FH}[\phi(\mathbf{r},t)]}{k_B T} + \kappa(\phi) |\nabla \phi(\mathbf{r},t)|^2 \right], \tag{4.7}$$

with

$$\frac{f_{FH}[\phi(\mathbf{r},t)]}{k_B T} = \frac{\phi(\mathbf{r},t)}{N_D}\ln\phi(\mathbf{r},t) + \frac{1-\phi(\mathbf{r},t)}{N_A}\ln[1-\phi(\mathbf{r},t)] + \chi\phi(\mathbf{r},t)[1-\phi(\mathbf{r},t)]. \tag{4.8}$$

In the last two expressions, f_{FH} is the Flory-Huggins (FH) free energy of mixing, χ is the Flory-Huggins parameter, describing the interactions between the monomers of different type, while N_D and N_A refer to the degrees of polymerization of the components D and A of each polymeric chain, respectively. Note, that the second term in eq. (4.7) energetically penalizes the occurrence of concentration gradients and induces the coarsening of the domains [50, 66]. The coefficient κ for an incompressible polymer melt can be expressed as

$$\kappa(\phi) = \frac{1}{36}\left[\frac{l^2{}_D}{\phi(\mathbf{r},t)} + \frac{l^2{}_A}{1-\phi(\mathbf{r},t)}\right], \tag{4.9}$$

where l_A and l_B are the segment lengths of D- and A-polymer segments, respectively.

4.2.4 The field-based solar cell algorithm

In order to explore the performance of OPV cells as a function of the polymeric morphology for different compositions and architectures of polymer chain, we applied our simulation algorithm in the following way:

1. Calculation of the polymeric morphology by solving the SCFT equations;
2. Partitioning of the morphology for solar cell simulation;
3. Execution of the photovoltaic processes by performing the DMC simulations on the obtained morphology.

In Fig. 4.4 we provide a schematic illustration for our simulation algorithm. In the first step, we specify the parameters, defining the polymer model, such as the polymer chemical

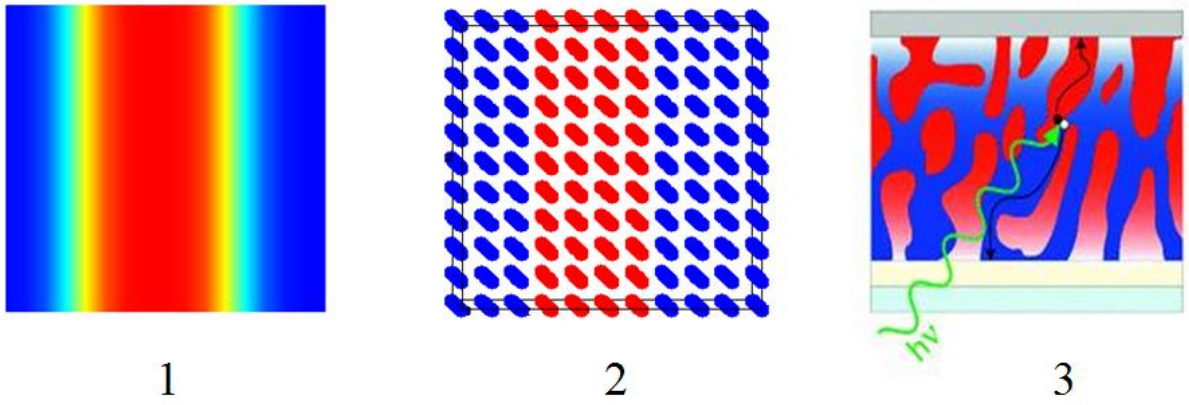

Fig 4.4: Schematic illustration of our field-based solar cell algorithm. The procedure consists of three steps: (1) determination of the polymer morphology by computing the SCFT solution, (2) definition of the lattice for solar cell simulation, and (3) performing the DMC simulations.

structures, interaction parameters between the different types of monomers, etc. Depending on the problem under consideration, we choose an appropriate method for obtaining the polymeric morphology, which can either be the dynamical or static SCFT method. Furthermore, by subsequently determining the corresponding SCFT solution, we obtain the distribution of the polymer volume fractions on the lattice, which we associate with the polymeric morphology. In the second step, we specify the lattice for solar cell simulations, which enables to simulate the elementary photovoltaic processes, related to excitons and charges. To accomplish this, we assume that the majority component at each lattice site determines whether the site belongs to the electron-conducting or hole-conducting phase. This approximation is needed due to the lack of information on the type of polymer chains in the field-based representation and is a presumably reasonable for highly phase-separated polymer-blend morphologies. In the final step, we performed the DMC simulations on the obtained morphologies, as described in chapter 4.2.2, by taking into account the individual conductive properties of the materials, obtained either experimentally or using theoretical methods.

4.3 Application of the field-based solar cell algorithm for studying the loss processes in polymer solar cells

By analyzing the properties of our simulation approach, we note that the algorithm combines the advantages of the mean-field approximation, to treat the polymer phase separation for a specific polymer mixture, and the DMC technique, enabling to track each elementary particle involved and, hence, explicitly describe their transport properties with respect to the local environment. To demonstrate the predictive power of this algorithm, we investigated the impact of the morphological characteristics of a novel phase-separated nanostructured DA-polymer blend on its photovoltaic properties at different degree of phase separation and various types of electric circuits. Our simulation results revealed that the disjunction of percolation pathways leads to the creation of dead ends, resulting in charge carrier losses through bimolecular charge recombination. Moreover, we observed a decay of the exciton dissociation efficiency near to the structural defects, caused by a high charge accumulation. From these observations, we concluded that both the charge carrier loss and the exciton loss phenomenon lead to a dramatic decrease in the internal quantum efficiency. Finally, by analyzing the photovoltaic behavior of the nanostructures under different circuit conditions, we showed that the dark current significantly determines the solar cell performance.

4.3.1 Computational details

In our simulations, we considered a DA-polymer blend composed of poly(perylene-diimide-alt-dithienothiophene) (PPDI-DTT) and bis(thienylenevinylene)-substituted polythiophene (biTVPT), whose chemical structures are present in Fig. 4.5. To compute the morphologies, resulting from, the dynamics of the phase separation process, we made use of the dynamical SCFT method, implemented in the program package OCTA [50, 71, 74]. In the calculations we set a system's temperature of T = 298 K and a lattice size of 32 × 32 sites with a lattice constant of a_0 = 1 nm as well as periodic boundary conditions applied in all directions. To solve the system of CHC equations (4.6), (4.7) and (4.8), we used the finite-

difference technique with a mobility parameter of M = 10. For the polymer model, we considered a system, composed of a symmetric DA-homopolymer blend with $N_D = N_A$ = 10, as well as a Flory-Huggins interaction parameter χ = 0.5. To perform the numerical integration, we used a time step of 0.01 with a maximum number of simulation steps of 5000. To obtain the equilibrium configuration that would be extracted from the phase-separation process of the DA-polymer blend at infinite times, we used the static SCFT method.

In the DMC simulations, we allowed the exciton creation at randomly chosen sites of the lattice with a constant rate ω_{cre} = 900 s^{-1} nm^{-2}, which was calculated from the AM1.5 solar spectrum with illumination of 90 mW/cm^2 and the absorption spectrum of the polymer blend [75, 76]. The exciton hopping rate from the lattice site i to a nearby site j was determined using the Förster theory, given in eq. 2.7, while the exciton-localization radius was taken to be R_0 = 10 nm. The prefactor $\omega_e R_0^6$ = 2 ps^{-1} nm^6 and exciton recombination rate ω_{dec} = 0.002 ps^{-1} were selected to

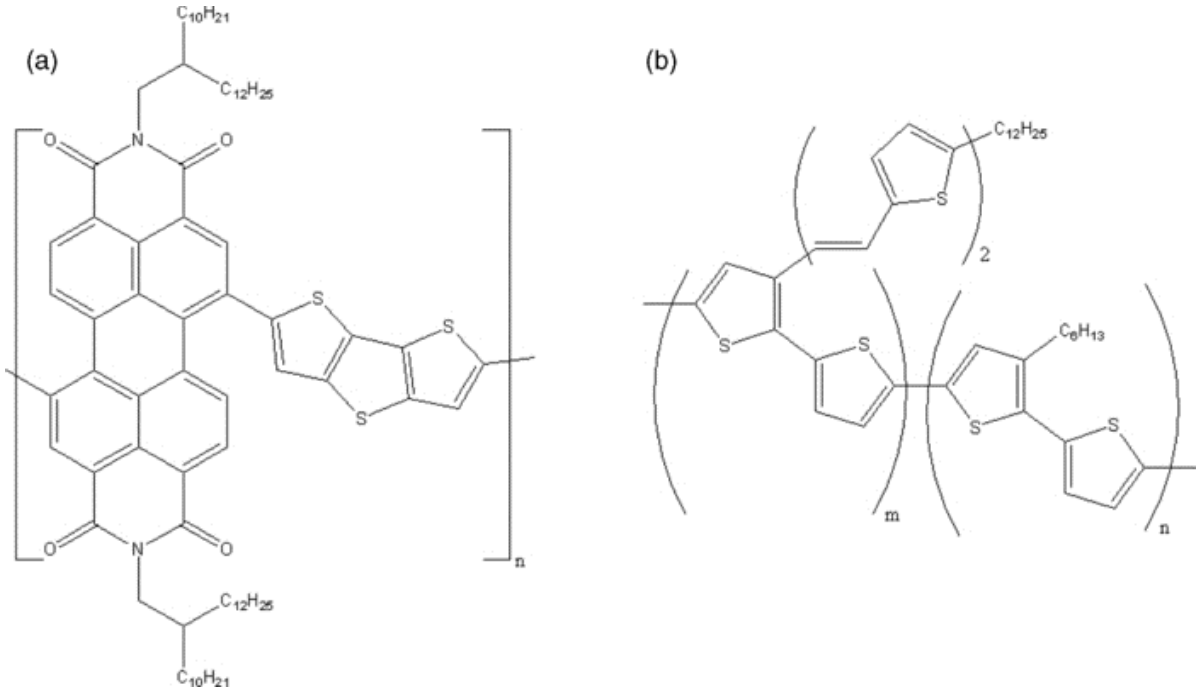

Fig. 4.5: Chemical structure of the DA-polymer blend PPDI-DTT-biTV-PT composed of (a) poly(perylene diimide-alt-dithienothiophene) and (b) bis(thienylenevinylene)-substituted poly-thiophene.

ensure the experimental values of exciton diffusion length (~10 nm) and lifetime (~500 ps). Moreover, the excitons on the lattice were allowed to jump within a radius of 5 nm in either the hole- or electron-conducting phase. The mobility of the electrons/holes with charge q in both polymer species is taken as $\mu_{e/h} = 10^{-3}$ cm^2 V^{-1} s^{-1}. Note, that in our simulations we assumed the electrons and holes to have equal mobility and, thus, we chose for both charge carrier types $V_{hop} = 1.06 \times 10^{-2}$ ps^{-1} and a material of dielectric constant $\varepsilon_r = 3.5$. To treat the long-range tail of the electrostatic contribution, we have cut the Coulomb potential at $r_c = 10$ nm and shifted the function to zero. In addition, we assumed that, if an electron and hole are located on adjacent sites, they can recombine with the rate $\omega_{rec} = 10^{-6}$ps^{-1}. At each lattice site, we imposed a single occupancy constrain for the excitons as well as the charge carriers. Finally, we considered the system to be equilibrated when the deviations in the values of exciton dissociation efficiency, charge transport efficiency, and exciton lifetime did not exceed the predefined error of 0.01% within a certain time range at the end of the simulations.

To study the influence of the dark current on the device performance, we have taken into account three different circuit conditions. In our simulations, the open circuit corresponds to the device operation condition, in which only the photo-generated charges are present in the system. This condition describes the behavior of a system, corresponding to the region near to the zero values of the applied bias on the current-voltage curve, as described in chapter 1.2. Furthermore, the real circuit refers to the case, in which both photocurrent and dark current are taken into account. This type of circuit is usual for the region of applied bias, corresponding to the maximum of device power. Finally, by the short circuit we imply the case, when the injected charges compensate the excess of one type of the charges in the active layer, i.e. the system is kept electro-neutral. This circuit is usually not observed in experiment and used in our simulations to study the effect of charge imbalance. The presence of the dark current was mimicked by performing the charge injections from the Fermi levels of the electrodes to the corresponding polymeric phases. Thus, at each electrode site, i.e., at a junction between electron conductor and cathode or hole conductor and anode, a charge carrier can be injected at a time interval determined by its characteristic injection rate. The injection rate was calculated using the Marcus formula in eq. (4.1) by considering that the difference in the energies $E_i - E_j$ equals the energy barrier of $E_{IB} = 0.4$ eV [75].

4.3.2 Results and discussion

We start the analysis of our simulation results by considering the dynamical evolution of the polymeric system during the phase separation process, composed of the DA-polymer blend PPDI-DTT-biTV-PT. In Fig. 4.6 we show the corresponding morphologies, obtained by using the dynamical SCFT method. Here, with the morphologies we mean the space distribution of the volume fractions of the A- monomer type, changing as a function of the simulation time. Our results show that with increasing simulation time the morphology attains an increasing degree of phase separation, causing a change in configuration from the disordered (A) to the lamellar-like nanostructure (I). Moreover, we observe that the phase separation process begins with creation of the isolated islands consisting of one type of polymers (B), which under the dynamical evolution of the system tend to enlarge their size though the formation of percolation pathways. At the same time, we see that the formation of the islands leads to point defects in the nanostructure, such as the defect in the upper right corner of the diagrams (B-F). Moreover, for the morphologies C and D we see that several A phases are completely disconnected from the rest of the phases, resulting in formation of the dead ends. However, at the transition from the morphology E to F, the A phase at the inclusion becomes continuous, whereas the D phase becomes fully continuous only at the transition from the morphologies F to G.

Next, in Fig. 4.7 we visualize the corresponding results for the charge transport efficiency, exciton dissociation efficiency, and internal quantum efficiency, obtained for the morphologies previously introduced as a function of interfacial length between the phase-separated domains. These results were obtained under the different device operation conditions, namely, under the open-circuit, real-circuit, as well as short-circuit conditions. In Fig. 4.7 (a) we show that for all circuit conditions with increasing interfacial length the EDE steadily increases in the range from 60 to 95 nm, corresponding to the morphologies from G to I. For the morphologies ranging from A to F, however, the quantity undergoes a change in a slope and increases more slowly as a function of interfacial length, than in case of the morphologies range G-I. By contrast, from Fig. 4.7 (b) we deduce that the CTE decreases with increasing interfacial length for all three device operation

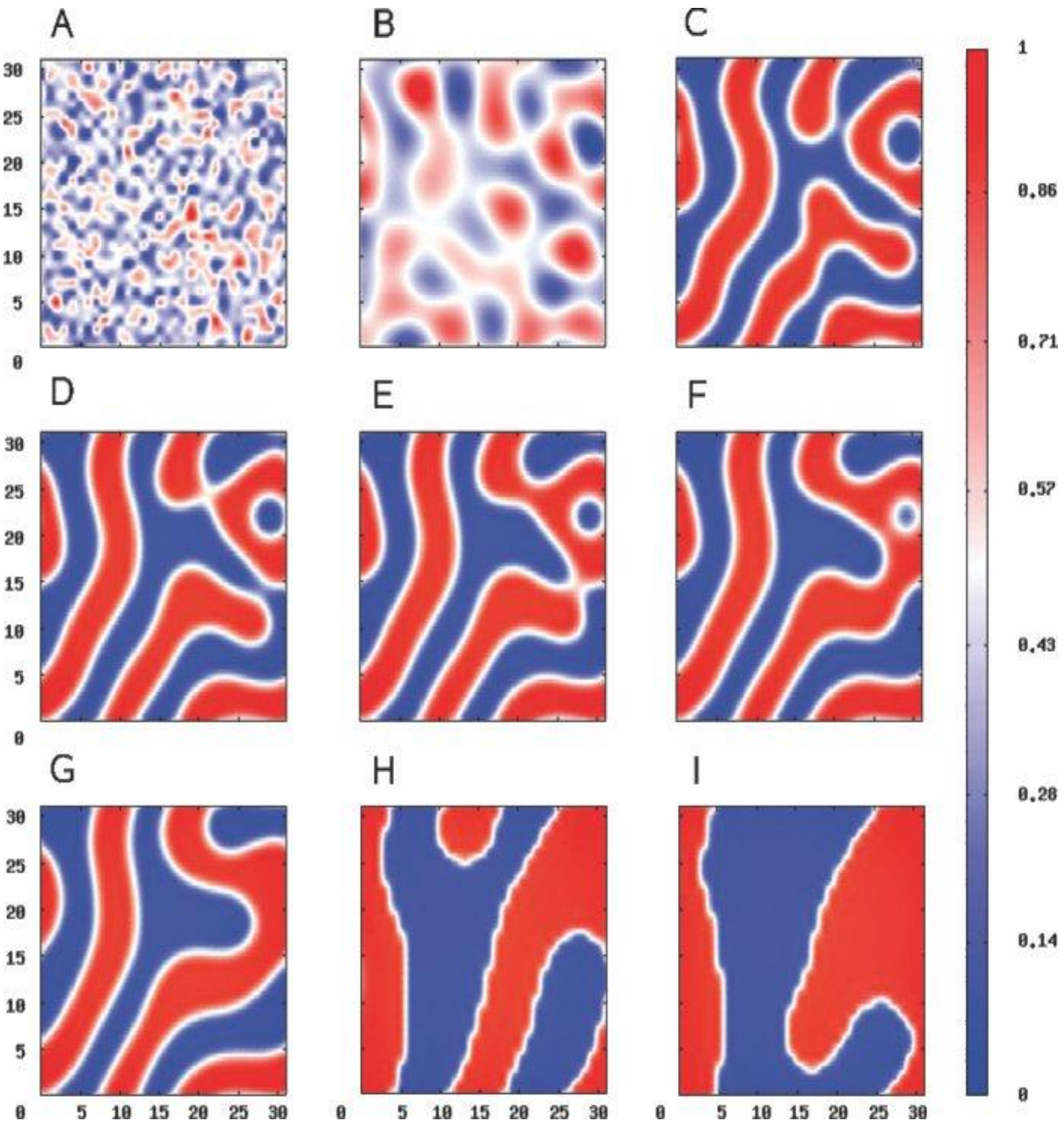

Fig. 4.6: Morphologies of the DA-polymer blend PPDI-DTT-biTV-PT at different scale of phase separation as a function of the volume fractions of the monomer types obtained by using the dynamical SCFT method [red: A phase (electron conducting); blue: D phase (hole conducting)].

conditions. Thus, after a slow steady decrease starting from 100% efficiency in the range from 60 up to 95 nm (I-G), the curves undertake a sharp drop in efficiency of about 60% at an interfacial length of 100 nm under real-circuit and open-circuit conditions (G-D). Moreover,

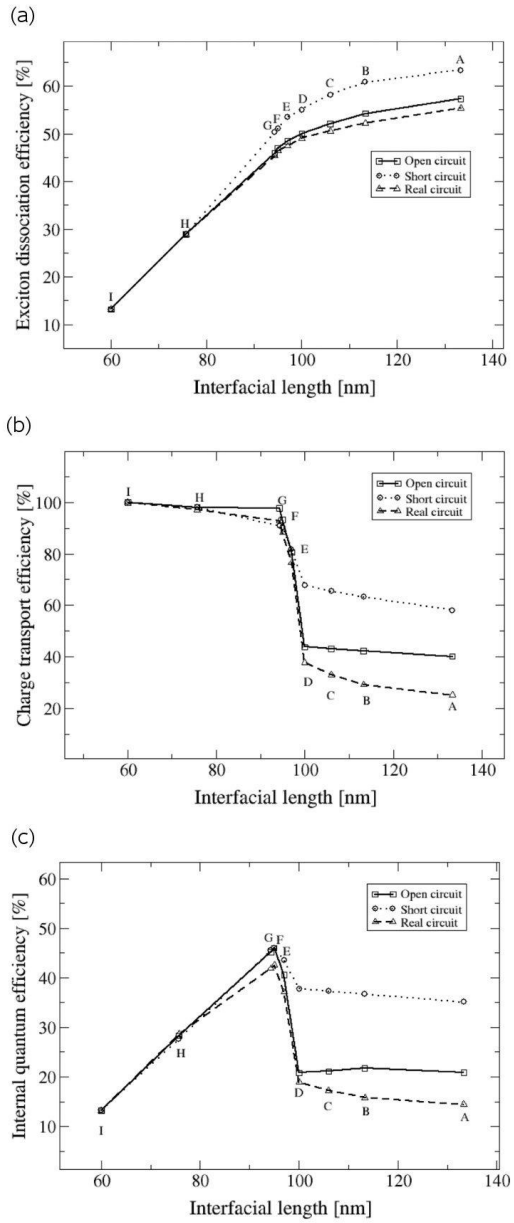

Fig. 4.7: Exciton dissociation efficiency (a), charge transport efficiency (b), and internal quantum efficiency (c) of the phase-separated DA-polymer blend PPDI-DTT-biTV-PT as a function of interfacial length under open-circuit, short-circuit, as well as real-circuit conditions, obtained by using dynamical SCFT method.

we observe that the largest losses in efficiency take place at the transition between the morphologies E and D. By contrast, in the short-circuit case the CTE at the same interfacial length undergoes only a smooth decrease of about 20%. In all three cases the regimes of major efficiency loss are followed by a range of slow steady decrease with diminishing degree of phase separation of the DA-polymer blend up to the disordered morphology A [50].

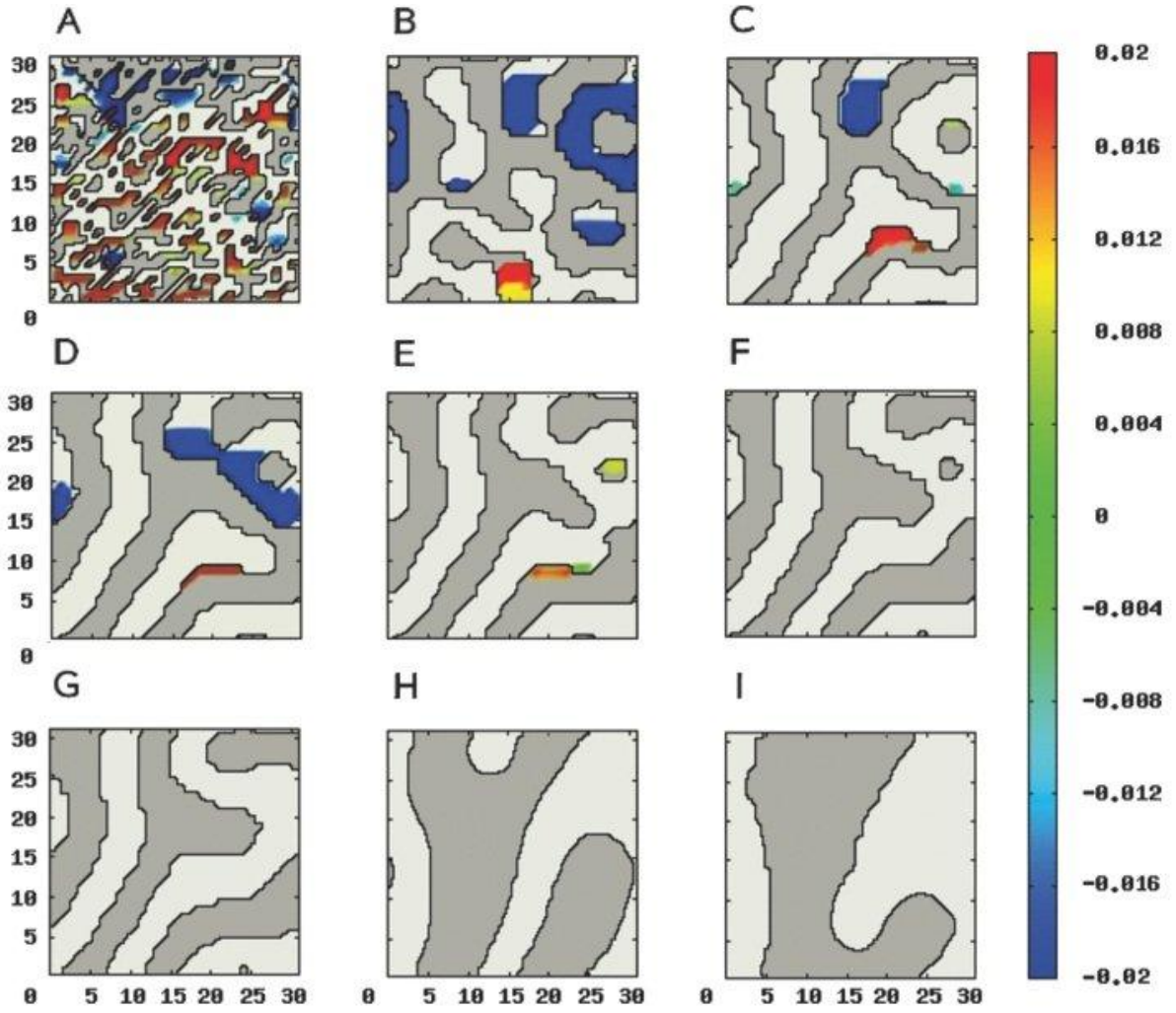

Fig. 4.8: Charge density of the phase-separated DA-polymer blend PPDIDTT-biTV-PT for morphologies with different scale of phase separation under real-circuit conditions, obtained by using the dynamical SCFT method [light grey: A phase (electron conducting); dark grey: D phase (hole conducting)]. Electrodes are applied in horizontal direction for all morphologies.

Next, we analyze the simulation results of the IQE, visualized in Fig. 4.7 (c). We observe that the quantity for all three circuit conditions has a maximum at an interfacial length of 95 nm, which corresponds to the morphology F. With decreasing degree of phase separation the quantity experiences a sharp drop of about 25% under open-circuit and real-circuit conditions, whereas in the short-circuit case the drop in efficiency amounts only to 10%. The sharpest decline in the IQE in all cases takes place in the range of interfacial lengths

between 97 nm and 100 nm, which corresponds to the range of morphologies between D and F. By comparing these results to the ones of the EDE and CTE in Figs. 4.7 (a) and 4.7 (b), we conclude that at low interfacial lengths the IQE is primarily restricted by a low EDE, whereas at high interfacial lengths the IQE is essentially limited by a low CTE. At the maximum IQE, the best compromise between the efficiencies of exciton dissociation and charge transport is found, which results in the maximum device performance.

Although overall the curve shapes for all chosen devise operation conditions are similar, we notice that both the EDE and the CTE are affected by variations due to the presence of the dark current. While for the highly phase-separated morphologies H and I, these changes can be considered as insignificant, the difference in the values between the efficiencies for the range of morphologies A-G under the chosen circuit conditions steadily increases as a function of the interfacial length. Thereby, we observe that both EDE and CTE reach their highest values for the open-circuit condition. These simulation results reveal that the charge imbalance together with the presence of dark current causes the significant reduction of both EDE and CTE, resulting in the lowering of the value of IQE. Moreover, we see that with increasing number of point defects in polymeric morphology, the reduction of the IQE becomes stronger. Therefore, we conclude from this investigation that the dark current needs to be taken into account adequately in the computer simulation of loss processes of polymer solar cell devices.

To study in more detail the causes for the changes in the IQE with the scale of phase separation of the polymer blend, we analyze the corresponding distributions of the charge densities, obtained under real-circuit and short-circuit conditions for the previously introduced morphologies and depicted in Figs. 4.8 and 4.9. In case of the disordered morphology A, we see regions of strong charge accumulations near to the point defects distributed allover the space for both circuit conditions. These accumulations are due to the small phase thickness, causing that only a few excitons are lost on the route to the DA interface. Thus, most of the excitons become separated into the free charge carriers, which, due to the lack of continuous percolation pathways to the electrodes, accumulate and then recombine in the confined region of space. Therefore, a major performance-limiting factor of such morphologies is their low charge transport capacity. In case of the morphologies B to D with moderate degree of phase separation, we observe that the charge carriers are captured and accumulated near to the

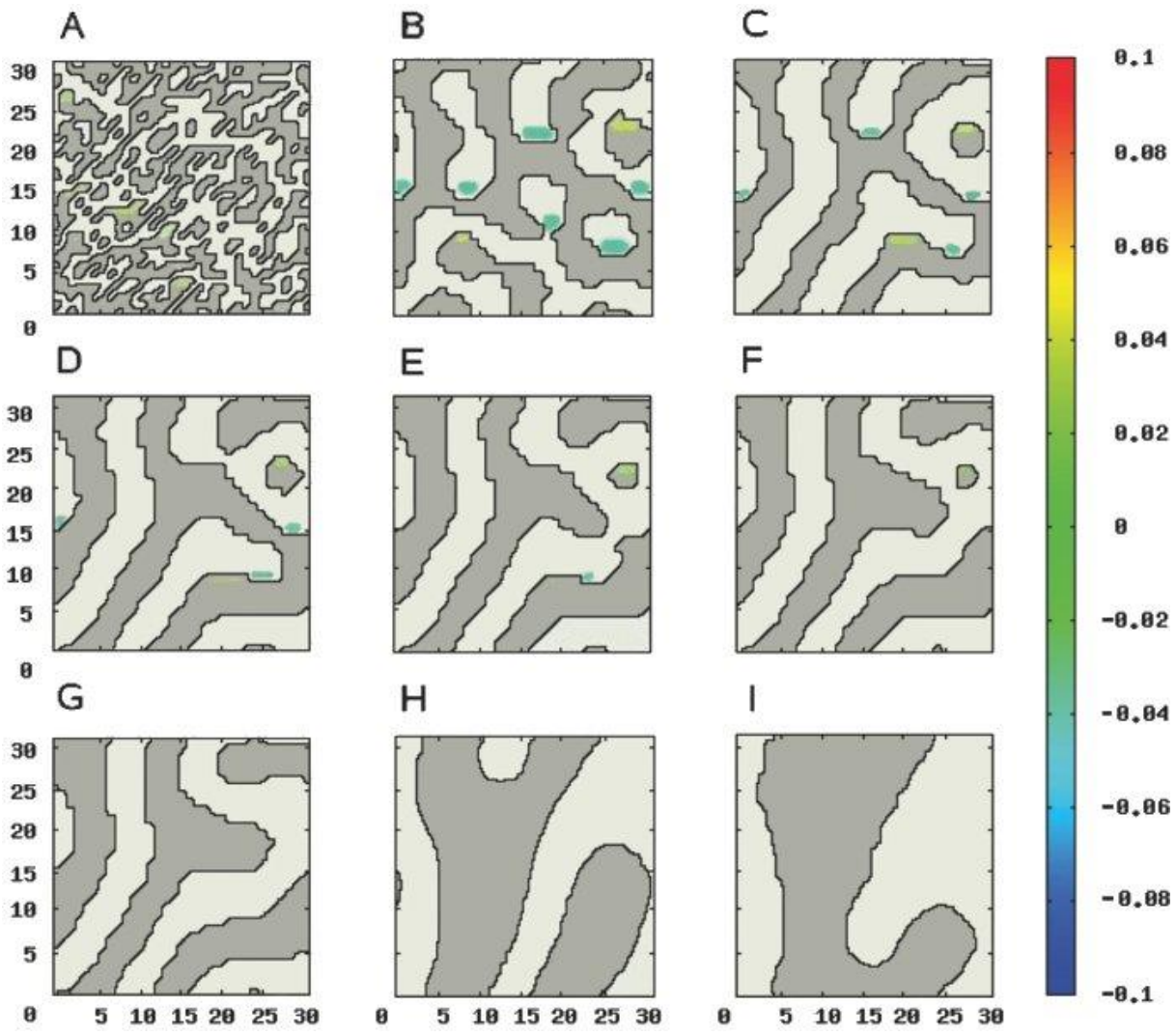

Fig. 4.9: Charge density of the phase-separated DA-polymer blend PPDIDTT-biTV-PT for morphologies with different scale of phase separation under short-circuit conditions, obtained either with the DMC-CHC-TDGL (AH) or the DMC-CHC-SCFT method (I) [light grey: A phase (electron conducting); dark grey: D phase (hole conducting)]. Electrodes are applied in horizontal direction for all morphologies.

several dead ends and bottlenecks, severely reducing their efficiency of charge transport to the electrodes. In particular, we see that at the point defects and at the dead ends in the upper left and right corner of the diagram a significant amount of electrons is accumulated. This relates to the fact that the charges under the influence of the electrical field, resulting from the difference in electrode work functions, are trapped in these defect structures and can only decay through charge recombination at the DA interfaces. Similarly, the holes are strongly

concentrated in a notch, formed by the D phase, and remain trapped in this region, due to the influence of the external electrical field and the Coulombic attraction to the nearby accumulated electrons. Moreover, we deduce from morphology C that isolated inclusions, which are fully disconnected from the electrodes are not able to function as effective charge traps. In conclusion, we see that the charge transport is severely hindered and, thus, the IQE is severely reduced in cases where the A- and D-phases are partially discontinuous, but remain connected to the electrodes to some extent. This demonstrates the important influence of the charge injection at the electrodes on the charge accumulation at the defect structures and the overall CTE, as confirmed by Fig. 4.7 (b). It should be also mentioned that the high charge transport efficiency for the short-circuit case, in comparison to the real-circuit and open-circuit case, correlates with the reduction of the area, belonging to the accumulated charges in the range of morphologies A-D.

To investigate the impact of defects and circuit-type an the photovoltaic performance in more detail, in Table 4.1 we further consider the ratio of the total number of charge losses versus the total number of generated charges v_{TL} for the morphologies D and E, for which the

Morphology	ν_{TL} **(%)**	ν_{IR} **(%)**	ν_{ER} **(%)**	ν_{TC} **(%)**
D (sc)	32.2	21.0	9.5	1.7
D (rc)	62.2	47.2	3.1	11.9
D (oc)	56.2	45.0	. . .	11.2
E (sc)	18.4	16.4	1.7	0.3
E (rc)	23.4	19.6	1.5	2.3
E (oc)	19.6	17.6	. . .	2.0

Table 4.1: Ratio of the number of lost charges through the number of generated charges for the DA-polymer blend PPDI-DTT-biTV-PT in case of the morphologies D and E under open-circuit (oc), short-circuit (sc), as well as real-circuit (rc) conditions, obtained with the DMC-CHC-TDGL method. The total ratio of lost charges ν_{TL} is decomposed in contributions from charge losses resulting from internal recombinations ν_{IR}, external recombinations ν_{ER}, as well as trapped charges ν_{TC}.

largest change in IQE is observed. Moreover, we consider that ν_{TL} can be spitted into there contributions, such as:

$$\nu_{TL} = \nu_{IR} + \nu_{ER} + \nu_{TC}, \tag{4.10}$$

where ν_{IR} refers to the recombinations, in which only the photo-generated charge carriers are involved (internal recombinations), ν_{ER} is the recombination type, in which one of the charge carriers has been injected from the electrode (external recombinations), and ν_{TC} corresponds to the type of losses due to the charge trapping inside the morphology (trapped charges). Thus, from the analysis of the data, we conclude that for all investigated systems the largest contribution to the charge losses comes from the internal recombination process. Thereby, we observe a strong correlation between the amount of the trapped charges and the value of internal recombination. This observation can be explained by comparing the rates of charge hopping and charge recombination processes, which define the probability of the event occurrence. Although the charge hopping rates are dependent on the local environment, the prefactor in the Marcus formula of 1.06×10^{-2} ps^{-1} is larger than the charge recombination rate by four orders of magnitude. Therefore, the charge hopping process is a much more probable event. However, if the charges are captured at the point defects, the charge recombination becomes the only available event, whose occurrence is accelerated due to the Coulombic attraction of the opposite charges to the region. Furthermore, by analyzing the dependence of the external recombination process on the circuit type for the morphologies D and E we observe that largest number of the losses takes place under the short-circuit condition. However, at the same time, we see the reduction of the ν_{TC} with respect to the open-circuit condition by 9.5 % and 1.7 % for the morphologies D and E, respectively. Thus, due to the mentioned correlation between the ν_{TC} and ν_{IR}, we can state that in the electro-neutral systems the external recombination reduces the number of charge losses, resulting from the internal recombination. In contrast, for the real-circuit case we see the increase of ν_{TC} compared to the open-circuit condition. Therefore, we conclude that the charge accumulation process does not only occur due to the morphological defects, but it is also affected by the circuit conditions.

In order to support our findings on the influence of charge trapping on the device performance, we computed the distributions of the exciton dissociation frequency as well as

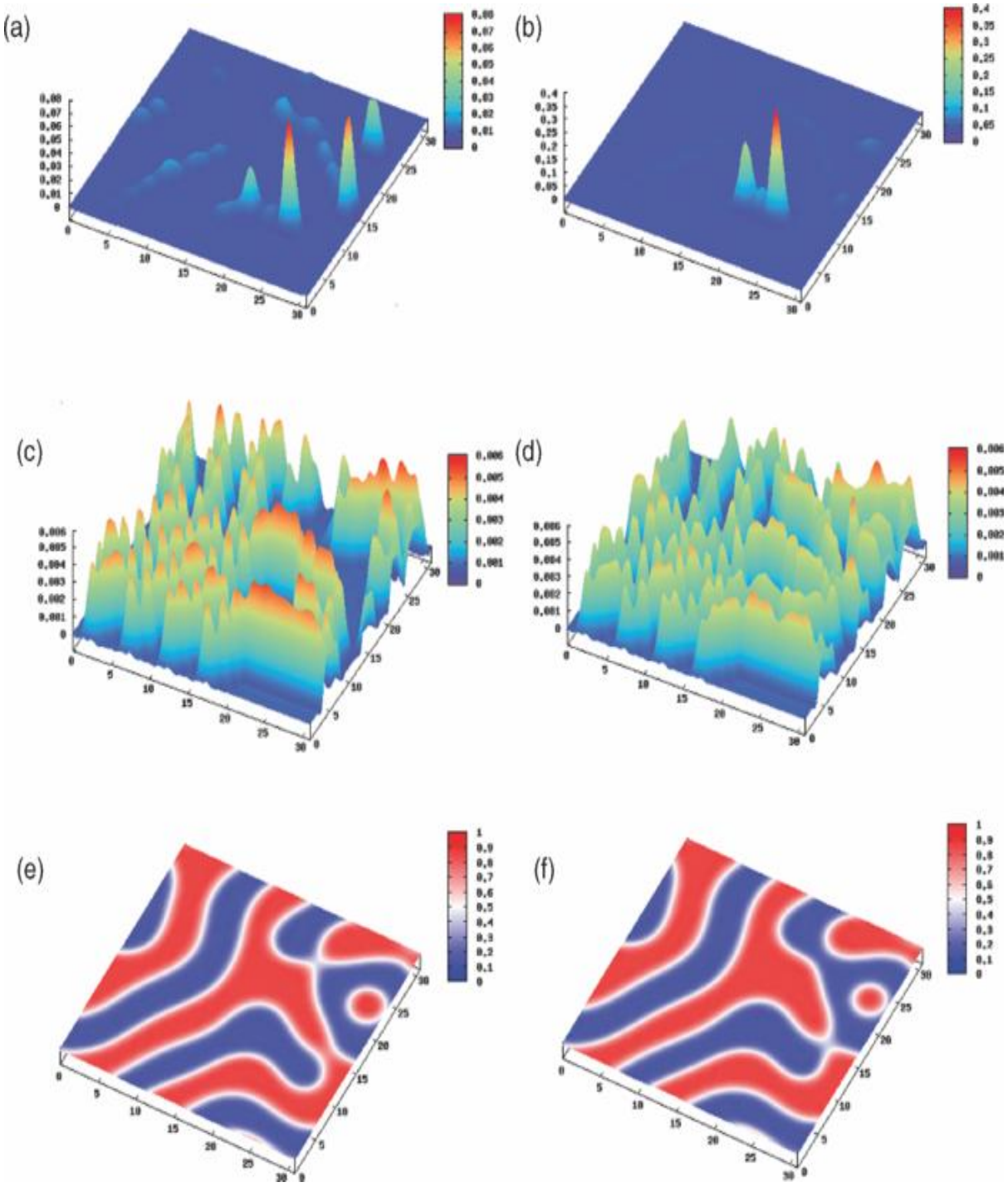

Fig. 4.10: Frequencies of charge recombination (a, b) and exciton dissociation (c, d) as a function of the volume fractions of the monomer types (e, f), obtained with the DMC-CHC-TDGL method, for the DA-polymer blend PPDI-DTT-biTV-PT in case of the morphologies D (left) and E (right) under real-circuit conditions [red: A phase (electron conducting); blue: D phase (hole conducting)].

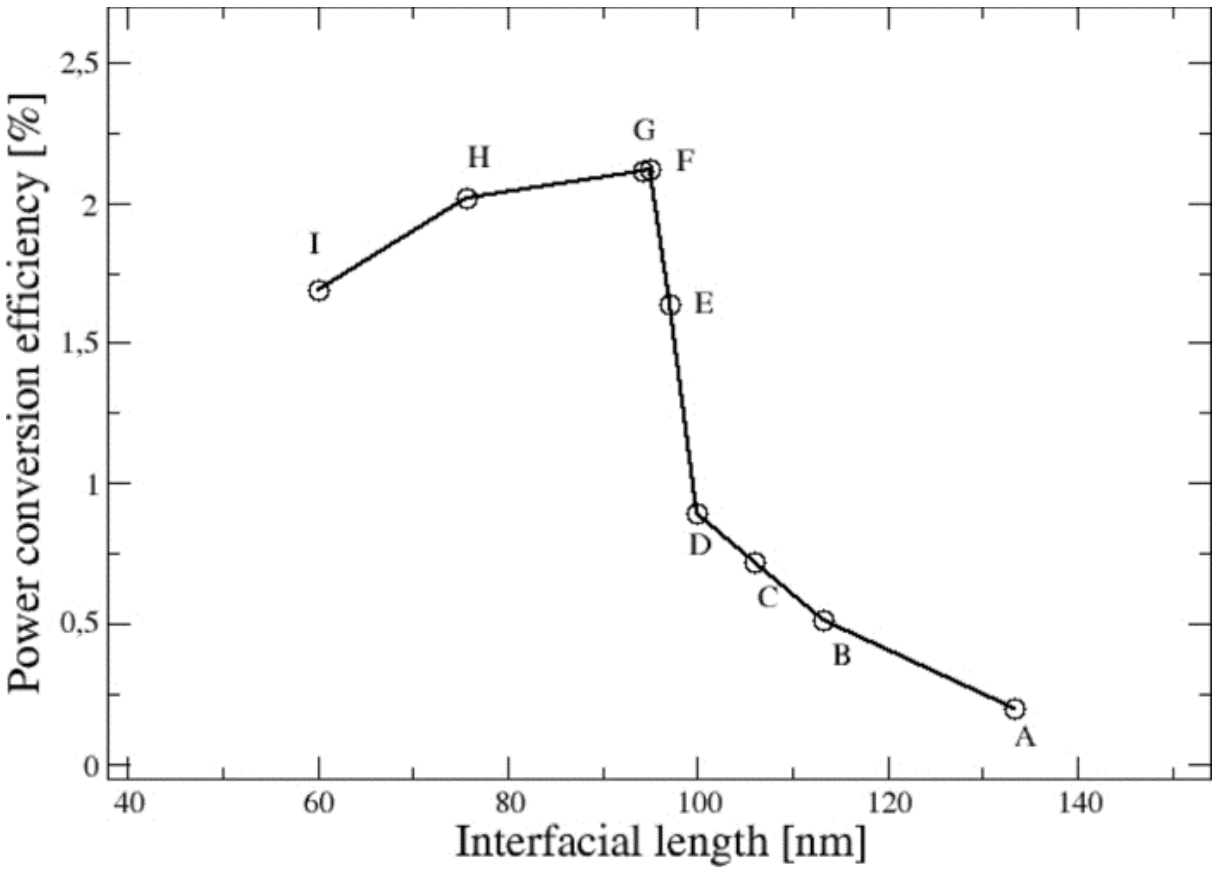

Fig. 4.11: Power conversion efficiency for the DA-polymer blend PPDI-DTTbiTV-PT as a function of interfacial length under real-circuit conditions, obtained with the DMC-CHC-TDGL method.

the charge recombination frequency for the morphologies D and E. In Fig. 4.9 we visualize the corresponding results, obtained under the real-circuit operation condition. Our results demonstrate that the charge recombination take place primary near to regions of charge accumulation. Moreover, by considering the space distribution of the exciton dissociation frequency, we conclude that the polarization of the DA interface due to the presence of the trapped charges significantly reduces the value of the EDE, which explains the slowing of the slope of the EDE curve as a function of interfacial length for the highly disordered morphologies.

In addition to the investigation of IQE behavior at different scale of phase separation, we computed the values of power conversion efficiency for the obtained morphologies under the real-circuit condition, which are plotted in Fig. 4.9. By comparing the dependences of the IQE and PCE as a function of interfacial length, we observe that both curves exhibit the same

maximum, corresponding to the morphology F. According to our previous discussion, the maximum in this nanostructure is explained by the disappearance of the electron- and hole-traps through the formation of continuous percolation pathways, allowing a nearly unperturbed flow of the charge carriers to the electrodes. In such an optimal morphology almost no charges are accumulated or lost due to charge recombination, while an optimal phase thickness for exciton dissociations is guaranteed. Consequently, the elimination of the nanoscale defect structures from morphologies D to F causes an increase of about 1.23 % in the PCE, 24 % in the IQE, and 55 % in the charge transport efficiency under real-circuit conditions. However, beside the similarity, we should also acknowledge the difference in behavior of the IQE and PCE curves. By comparing the Fig. 4.7 (c) and Fig. 4.9, we see that the increase of the PCE for the range of morphologies G-F is smoother than the corresponding one for the IQE curve, while the drop of the PCE due to lowering of CTE (A-F) is much sharper. This observation indicates that for the optimization of PCE under real-circuit conditions, we must ensure highly efficient charge transport within the materials.

In summary, from our simulation results, we conclude that the polymeric morphology influences the performance of OPV cells in the following way. First, the morphological defects, more specifically, the bottlenecks, isolated inclusions, and dead ends, resulting from the polymer phase separation process, causes the accumulations of charge carriers in the respective regions. These charge accumulations are induced by the increase of the Coulombic attraction between the opposite charges and can only decay through bimolecular charge recombination. Thereby, we observe that the larger the area, belonging to the trapped charges, is, the more events of bimolecular charge recombination between photo-generated charges are taking place. Moreover, our results suggest that the presence of the dark current accelerates the trapping of the charges near to the defects, and only the artificially imposed electro-neutral condition reduces the number of charge accumulations, and, hence, by changing the materials of the electrodes, we can achieve a higher device performance for the same polymeric nanostructure. Finally, we see that the accumulated charges influence not only the charge transport across the active layer, but also the exciton dissociation efficiency. This can be deduced from the reduction of exciton dissociation frequency near to the regions of the charge accumulations, as shown in Figs.4.9 (c) and (d).

Furthermore, we should mention that the results of our simulations are in agreement with several experimental findings. For instance, Snaith *et al.* [77] found through the composition analysis and photoluminescence emission spectroscopy experiments on PFB/F8BT-polymer blends that the process of charge transport and not the process of charge generation is the limiting factor of the device performance. We should also point out in this context that several recent experimental and theoretical studies [21, 50, 62, 66, 78, 79, 80] have demonstrated that structural characteristics can strongly affect the processes of charge generation and recombination as well as charge transport to the electrodes. Moreover, it is well-established that structural inhomogeneities, such as bottlenecks and dead ends, generally are created during the process of fabrication and can have a significant influence on the photovoltaic efficiency of nanostructured DA-polymer blends [50, 66, 81]. To eliminate such inhomogeneities in the experiment, different techniques have been conceived in the past decades, which permit to produce idealized morphologies free of defects. One strategy is to rearrange the nanophases using electrical fields. Russell *et al.* [50, 66, 82] could demonstrate in this way that defect-free nanostructures of diblock copolymers can be generated. A further procedure is controlled annealing. By applying this technique to PFB/F8BT blends, McNeill *et al.* [50,83] observed a dependence of the dynamics of charge generation on the degree of phase separation. They found that the device performance for a phase-separation length of 20 nm is optimal. In further studies it has been speculated that charge transport can also be affected by intra-molecular defects, such as kinks and chemical impurities [50, 84]. Such defects may increasingly be important in confined regions of the morphology with strong variation in composition of the DA-polymer blend, i.e., in bottlenecks and dead ends. Moreover, it is also worth emphasizing that blend systems are generally limited in their usefulness for flexible device applications due to their morphological instability [50, 85], conferring poor mechanical properties and thermal stability [50, 86]. They are often kinetically trapped in metastable states and their domains are known to migrate thermally, causing the disruption as well as aggregation of domains on timescales relevant for OPV applications. This may result in the formation of domains of microscopic or even macroscopic size in the D- and A-material. Moreover, their instability and low interpenetrability can reduce the interfacial area between both materials, increasing the diffusion length excitons must travel before charge separation can occur. In ultrathin polymer-blend films the morphological

evolution might further be stimulated by surface deformation modes [87], induced through the release of residual stresses resulting from the fabrication process, non-equilibrium interactions with other device components, an externally applied mechanical strain or electrical fields [50].

It is worth noting that the set of morphologies, which we studied previously, represents the snapshots of the polymer phase separation process. On the one hand, the energy change during the polymer phase separation process is relatively small, which leads to relatively long lifetimes of the intermediate polymeric configurations. In particular, this is a reason why a degree of point defects is observed in experimental morphologies. On the other hand, these structures are metastable, which potentially counteracts the possibility to construct the OPV nanodevices with the outdoor lifetime of several years, basing on polymer blends. To stabilize the morphology of the active layer, one possibility is to make use of block copolymers. Below the order-disorder transition temperature, they form a network of physically stable cross-links by accomplishing a thermodynamic phase-separation process, providing long-time stable morphologies with finer scale and higher performance compared to polymer blends [88].Thus, Sun *et al.* [89] reported that a photovoltaic device composed of a thin film of a donor-bridge-acceptor-bridge-type block copolymer shows a significant performance improvement over its corresponding DA blend, more specifically, the open-circuit voltage *Voc* increased from 0.14 to 1.1 V and the short-circuit current *Jsc* increased from 0.017 to 0.058 $mAcm^{-2}$ under identical conditions. They explained the major improvements in the photovoltaic properties by the block-copolymer phase-separation process and molecular self-assembly that leads to a reduction of the exciton and charge carrier losses. In another work Lindner *et al.* [90] compared the performance of a block-copolymer device, composed of blocks of the hole conducting poly(vinyl-triphenyl-amine) and electron-conducting poly(perylene-bisimide-acrylate), to a device made from a blend with identical composition and phase thickness. They demonstrated that the photovoltaic properties of the block copolymer significantly surpass those of the blend device. In particularly, the device performance parameters *Jsc* and *Voc* were found to improve from 0.028 $mAcm^{-2}$ and 0.525 V for the blend to 0.19 $mAcm^{-2}$ and 0.865 V for the block copolymer, respectively. Moreover, the PCE was increased by one order of magnitude from 0.007% in the polymer blend to 0.07% in the block-copolymer device. However, it is well known that even with block-copolymer technologies perfect

periodic domain ordering is generally achieved only over nano-sized regions [87], thereby in the larger size-scales the structural defects can be also observed.

To estimate the influence of defects on the performance of OPV cells in block-copolymers, we applied our algorithm to the case of diblock- and triblock-copolymer systems. However, because the main part of this research was performed in a collaborative manner, we report here only the summary of the simulation results. Note, that the detailed description of the results can be found elsewhere [91]. In this work, we studied the systems composed of DA-diblock- and ADA-triblock-copolymers and compared their photovoltaic performance as a function of the interaction strength between the monomers, chain architecture as well as external mechanical loadings. By considering the block-copolymer systems, which provide long-time stable thin-film nanostructured morphologies with optimal physical properties for flexible applications, we deduced that in the range from low up to intermediate χ-parameters an increasing number of continuous percolation paths with growing interaction strength between the monomers are formed. In this parameter range, the CTE and IQE increase up to a maximum, characterized by a minimum in the number of charge losses due to charge recombination. In the regime of high χ-parameters both block-copolymer systems form nanostructures with a large number of bottlenecks and dead ends, leading to a large number of charge losses due to charge recombination, charge trapping, and a deterioration in exciton dissociation. These loss mechanisms lead to a significant drop in the CTE and IQE for both types of block-copolymer systems in this parameter range. Moreover, by comparing the IQE curves of both polymer systems, we deduce that the diblock-copolymer system possesses a slightly higher IQE than the triblock-copolymer system over the whole range of χ-parameters. This essentially relates to its larger CTE, which is not compensated by the higher EDE in the triblock-copolymer case. By further subjecting the triblock-copolymer morphology with the highest IQE to different mechanical loads, we find that the photovoltaic performance of the material decreases with increasing external mechanical stress, caused by a growing number of charge losses due to charge recombination and charge accumulation. Finally, we have also demonstrated on the example of a system of triblock copolymers that the process of charge trapping in defects can be reversed by changing the polarity of the electrodes, which might confer these materials the ability to be used as charge storage media [31].

5. Photocurrent contribution from inter-segmental mixing in donor-acceptor-type polymer solar cells

In the present chapter we focus on the exploration of the influence of DA mixing as well as chemical changes in polymeric structure on the performance of organic photovoltaic nanodevices. We start with the description of recent experimental and theoretical findings, concerning the role of DA mixing in the performance of organic solar sells. Next, we introduce a novel particle-based solar cell algorithm, developed for studying the elementary photovoltaic processes in OPV cells on the atomistic scale, and apply it on a lamella-like phase separated PFB-F8BT blend. Furthermore, we compare the obtained data with the results of field-based solar cell algorithm, applied on the same polymeric morphology. From this comparison, we assess the impact of DA mixing on the EDE, CTE, IQE, and current density profile. Finally, we explore the causes of the deterioration of the device efficiency, associated with the photo-oxidation of the polymers [92].

5.1 Influence of DA mixing on the performance of organic solar cells

In chapter 4, we have shown that the field-based multiscale solar cell algorithm can efficiently be used to explain the reasons of the exciton and charge loss phenomena, occurring within a polymer bulk heterojunction at the mesoscale. Moreover, on the examples of diblock- and triblock-copolymers we have demonstrated that it provides an efficient tool for the minimization of exciton- and charge-losses through the control of the polymer phase separation process. However, the scope of application of our algorithm can easily be extended to the cases, encountered in experiment at the production and postproduction stages. By taking the advantages of SCFT approach within the SUSHI engine, we can use the various versions of the algorithm for solving the tasks of practical interest, such as, for example, the treatment of large morphologies, obtained in agreement with the predefined preparation conditions in three dimensional space [71]. This research is already carried out in our group and its results will be presented elsewhere. The goal of the present work is to devise a more

realistic model for the description of elementary photovoltaic processes in polymer solar cells. The problem, we have to face with the field-based solar cell algorithm, is that the polymeric morphology is associated with a set of the grid points, where each of these grid points represent either a D- or A-phase. In other words, the DA domains inside the phase separated nanostructure in the field-based algorithm are assumed to be pure. By contrast, in the experimental morphologies, the D- and A-polymers are usually mixed. We believe that this approximation may potentially affect the photovoltaic performance of polymer solar cells.

From the experimental side, the importance of D/A mixing optimization is often considered as an important factor, determining the performance of polymer solar cells. However, the exact role of the mixed regions in the efficiency of OPV devices is still not well-understood. For example, Bartelt *et al*. [93] have recently reported that the presence of the minor component in the pure domains increases the number of percolating pathways for the corresponding charge carriers, reducing in this way the probability of bimolecular charge recombination. At the same time, the results of time-resolved electrostatic force microscopy measurements, obtained by Coffey and Ginger [78], suggest that due to the mixing of the D- and A-components the domain centers, but not the visual interface, provide the highest contribution to the generated photocurrent. Other studies revealed that the presence of the mixed regions in the bilayer-like morphologies lowers the efficiency. For instance, Yan *et al*. [94] observed that increased DA mixing improves the exciton dissociation efficiency but, at the same time, decreases the charge transport efficiency across the region. As a result, the authors observe a dramatic deterioration of the internal quantum efficiency with increasing DA mixing.

From the theoretical side, the effect of the DA interfaces in OPV cells has first been investigated by Gregg and Hanna [63, 92], who adapted the conventional 1-dimensional drift-diffusion model of inorganic systems to the organic case. Their model takes into account that electrons and holes in OPV cells are generated at the DA interfaces and that they diffuse along internal concentration gradients within the system. However, this approach does not permit to treat the generation, diffusion and dissociation of the excitons explicitly, which strongly depends on the interface characteristics, i.e. inter-mixing of the D- and A-type of monomers. In a further work Härter *et al*. [65, 92] considered a prototypical 1-dimensional device with a broader DA-interfacial region, to study the consequences of blending on the

solar cell performance. In their model they restricted the generation of electrons and holes to the interfacial region and described the mixing of the segments at the DA interfaces by approximating the error function occurring in the solution of the mass-diffusion equation. The migration of the charges carriers through the entire system was simulated by solving the coupled Poisson and continuity equations and by taking into account the existence of the DA interfaces. However, their approach did only allow to investigate the effect of mixing at the DA interfaces in an approximate way at the continuum level [92].

5.2 Improvement of the field-based algorithm with respect to the DA mixing: particle-based algorithm

In order to estimate the influence D/A mixing on the photovoltaic efficiencies, our field-based algorithm required several improvements. The reasons for this are summarized in the following. First of all, in our simulations we assumed the phase-separated morphologies, obtained by the SCFT technique, to be a sufficiently accurate description of the polymer composition at equilibrium. As was shown previously, the SCFT solution represents a distribution of polymer volume fractions over the simulation lattice, whereby each lattice grid contains both polymer with non-zero concentrations. However, this morphology cannot directly be used for the solar cell simulation, as long as the DMC parameters, for example, the charge mobility as a function of polymer concentration, are not known. Another problem is that according to several studies, the properties, characterizing the charge transport phenomenon, such as, for example, the charge mobility, are highly sensitive to the mutual orientation of the conjugated segments in the material [95, 96]. In particular, the presence of the minority fraction the phases increases the distances between the segments of the same type, which leads to the decrease of the charge transport rates and, hence, causes an increase of charge losses.

To take into account the presents of DA mixing in polymeric morphology, we developed a novel particle-based solar cell algorithm, enabling to switch from the mesoscale to the particle representation. The algorithm consists of the following steps:

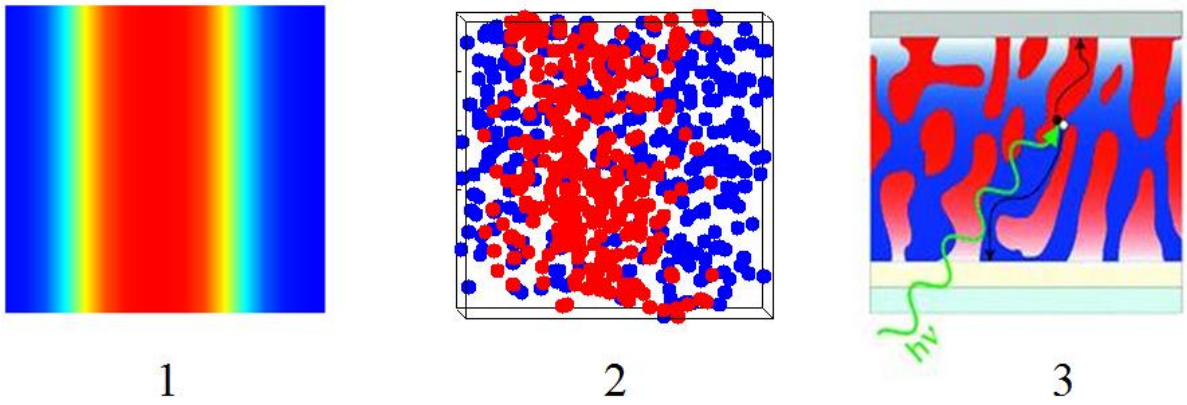

Fig 5.1: Schematic illustration of our particle-based solar cell algorithm for the determination of the photovoltaic performance with respect to the polymer composition. The procedure consists of three steps: (1) determination of the SCFT solution, (2) performing the field to particle transformation and equilibration of the obtained structure, and (3) performing the DMC simulations.

1. Calculation of the polymeric morphology by using the SCFT technique;
2. Performing the field to particle transformation and equilibration of the obtained structure;
3. Performing the DMC simulations using the resulting structure in particle representation.

In Fig. 5.1 we provide a schematic illustration for our particle-based algorithm. The simulations, based on this algorithm, start with the determination of the SCFT solution for a given polymeric mixture, exactly as in case of the field-based solar cell algorithm, introduced previously. In the second step we perform the field-to-particle transformation, using the density biased Monte Carlo technique, as we described in chapter 2.6. This provides a CG representation of the morphology. Furthermore, we transform the CG structure to the FG representation of our system, which we equilibrate with the tools of molecular dynamics. Finally, we perform the DMC simulations on the resulting FG structure.

To simulate the elementary photovoltaic processes on the structure in particle representation, the DMC algorithm also required several improvements. As a first modification in DMC algorithm, we take into account the effect of energetic disorder for the

diffusion of excitons. To this end, we modified the expression for the exciton hopping rate from site i to a nearby site j, obtained from the Förster theory, resulting in the following equation [92, 97]:

$$\omega_{ij} = \omega_{ex} \left(\frac{r_0}{r_{ij}} \right)^6 f(E_i, E_j), \tag{5.1}$$

where r_{ij} denotes the distance between the hopping sites i and j, whereas r_0 is the exciton localization radius and w_{ex} is the hopping-attempt frequency. The function

$$f(E_i, E_j) = \begin{cases} \exp\left[-\frac{(E_j - E_i)}{k_B T} \right] & \text{if } E_j > E_i \\ 1 & \text{if } E_j < E_i \end{cases}, \tag{5.2}$$

describes the influence of the site energies E_i and E_j on the exciton hopping rate, whereas k_B is Boltzmann's constant and T is the system temperature.

The second improvement in the DMC algorithm relates to the calculation of the prefactor in the Marcus formula or, more specifically, to the determination of the charge transfer integral. This parameter is highly sensitive to the relative position as well as orientation of the conjugated segments with respect to each other in the bulk polymer blend [46] and determines the efficiency of the charge transport within the material to a large extent. In our previous simulations, we avoided the explicit calculation of this parameter by using the Einstein relationship. However, in case of the full-atomistic morphology, the application of this approximation is rather questionable. To enable the explicit calculation of the parameter, we coupled the DMC algorithm to the quantum-chemical simulation package and computed the charge transfer integrals for all possible pairs of hopping sites within the certain cut-off radius by using the dimer projection method of Valeev *et al*, as we described in chapter 2.4.

5.3 Application of the particle-based algorithm for studying the influence of DA mixing on the performance of OPV cell

In present chapter, we describe the results of the study of the influence of the local segmental composition and chemical defects on the photovoltaic properties of DA-polymer

solar cells. In order to investigate the impact of DA mixing on OPV performance, we compare the simulation results, obtained from the field-based algorithm with the results, generated with the particle-based algorithm at atomistic resolution. To assess the suitability of the different representations, we explore the regions promoting charge generation and the pathways for charge transport with a particular focus on the region near to the DA interface. With our new particle-based algorithm, we show that the mixed regions in the PFB-F8BT blends provide a much higher contribution to the photocurrent than the region in close proximity to the visible domain boundaries. Finally, by making use of the advantages of the particle-based approach of the explicit description of the polymeric chains, we investigate the effect of photo-degradation of the fluorene moiety in the F8BT phase on the device performance [92, 98].

5.3.1 Computational details

For our simulations we consider a lamellar-like phase-separated polymer blend, composed of homopolymers of poly(9,9-dioctyluorene-co-bis-N,N-(4-butylphenyl)-bis-N,N-phenyl-1,4-phenylene-diamine) (PFB) and poly(9,9-dioctyluorene-co-benzo-thiadiazole) (F8BT), whose chemical structures are visualized in Fig. 5.2. To generate the equilibrium polymeric morphology, we used the static SCFT method and calculated a system composed of a symmetric AB-homopolymer blend with polymerization indices $N_A = N_B = 10$ and the segment lengths $b_A = b_B = b$ as well as the Flory-Huggins interaction parameter χ of 0.337. Moreover, we chose a discrete lattice of size 16×16 with a spatial mesh width of $\Delta x = \Delta y = 1$ in units of the polymer segment lengths. For the numerical integration of the Fokker-Plank equation, we used a contour step size of $\Delta s = 0.1$ and computed the distribution of the polymer volume fractions with a relative accuracy of 10^{-5}. To compute the morphologies, we made use of the program package OCTA [71, 99]. The equilibrium distribution of the polymer volume fractions over the simulation lattice was used to obtain the three dimensional field-based morphology. The equilibrium morphology within the atomistic representation was obtained by performing a mapping of the morphology, determined from the SCFT calculations, using the density-biased Monte Carlo method [100, 101]. From this procedure,

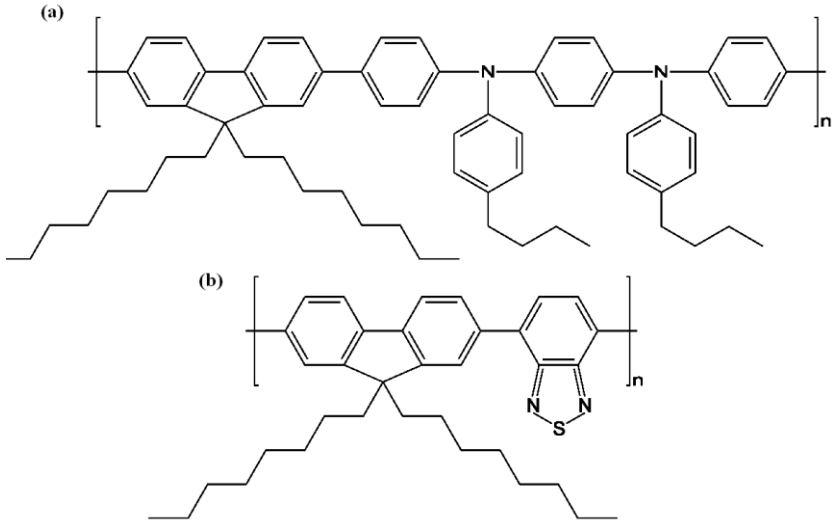

Fig. 5.2: Chemical structures of the DA-polymer blend, composed of (a) poly(9,9-dioctyluorene-co-bis-N,N-(4-butylphenyl)-bis-N,N-phenyl-1,4-phenylene-diamine) [PFB] and (b) poly(9,9-dioctyluorene-co-benzo-thiadiazole) [F8BT].

we gained the explicit coarse-grained (CG) representation of the polymer chains, which possess the same volume fractions as the SCFT-equilibrium structure. Furthermore, we accomplished a mapping of several intermediate CG structures by stepwise increasing the level of structural specification and performing a minimization for each of the configurations. To equilibrate the resulting full-atomistic structure, we performed a canonical Brownian dynamics simulation for 100 ps using a high friction coefficient of 3000 amu ps^{-1} [102]. Subsequently, we performed an equilibration with the molecular dynamics (MD) simulation method, using the GROMACS simulation package version 4.5.4 [103] in conjunction with the all-atom optimized potentials for liquid simulations (OPLS-AA) force-field [104, 105]. In addition, in our simulations we used full particle-mesh-Ewald electrostatics with a cutoff radius of 2.5 nm and computed the van-der-Waals interactions, using a shift function with the same cutoff radius. To generate an isothermal-isobaric ensemble with a temperature of 298.15 K and a pressure of 1 atm, we equilibrated the system over a period of 5 ns and then performed a production run of 2 ns. During both simulation phases, the system was coupled to a Nose-Hoover-thermostat with Δt = 1 ps and a Parrinello-Rahman barostat with Δp = 1 ps [106]. For the numerical integration of the equations of motion, we took the leapfrog integrator with the time-step of 1 fs. From the production phase, we chose 25 configurations,

obtained after each time interval of equal length of 80 ps. We noticed that after the equilibration phase the system size relaxed to an average box length of 10.7 nm. Therefore, we adjusted the size of the equilibrium field-based morphology to this value.

In our dynamical Monte Carlo simulations, the excitons were created at randomly chosen sites in the morphology with a constant rate of w_{cre} = 900 $s^{-1}nm^{-2}$, which has been determined from the AM1.5 solar spectrum with an illumination of 90 mW cm^2 and the absorption spectrum of the polymer material [92, 107, 108]. The parameter $\omega_{ex} r_0^6$ = 0.3 $s^{-1}nm^6$ as well as the exciton recombination rate ω_{dec} = 0.002 ps^{-1} were selected, to reproduce the experimental values of exciton diffusion length (~5 nm) and lifetime (~500 ps) [109]. Moreover, the excitons were allowed to hop within a radius of 3 nm in the hole- and electron-conducting phase. In both simulation approaches the charge carriers were allowed to hope within a radius of 2 nm in either the hole- or electron-conducting phase. To evaluate the prefactors in the Marcus formula for our particle-based algorithm, we made use of the dimer-projection method, developed by Valeev *et al*. and implemented within the program package VOTCA-CTP [110]. In our simulations, we calculated the charge transfer integrals for all possible pairs of hopping sites within the cutoff radius of 2 nm for each configuration from the MD trajectory. For the quantum-chemical calculations, we used the density-functional (DFT) theory with the Perdew-Burke-Ernzerhof (PBE) functional (DFT-PBE) method [111] and the basis set 6-311G*, implemented within the Gaussian03 package [112]. The prefactor for the field-based simulations was calculated by using the Einstein relationship with the mobility parameter, taken for both charge types as $\mu_{e/h}$ = 10^{-8} $m^2V^{-1}s^{-1}$ [92]. The energetic disorder of the material was described by Gaussian distributed density of states (DOS) of width σ = 0.062 eV [97]. To take into account the difference in the energy due to the Coulombic interactions of the charge with all other charges in the system, we made use of the following formula [92]:

$$\Delta E_{ij}^C = E_j^C - E_i^C, \tag{5.4}$$

with

$$E_i^C = \sum_{j=1}^{n} \frac{qe}{4\pi\varepsilon_0\varepsilon_r r_{ij}}, \tag{5.5}$$

where n is the total number of other charges in the system and e is the elementary charge with q = +e for electron-electron and hole-hole repulsion as well as q = -e for electron-hole attraction. The parameter ε_0 designates the vacuum permittivity, whereas ε_r = 3.5 is the relative permittivity of the material. Moreover, we treated the long-range tail of the electrostatic contribution by using periodic boundary conditions, similar to the Ewald summation technique. The image charge effect was included through [92, 97]

$$\Delta E_{ij}^{I} = \frac{e^2}{16\pi\varepsilon_0\varepsilon_r}\left(\frac{1}{x_i} - \frac{1}{x_j}\right), \tag{5.6}$$

where x_i and x_j denote the distances from the respective electrodes. Moreover, the influence of the build-in potential difference on the charges was taken into account as follows:

$$\Delta E_{ij}^{F} = e\left[\xi_{\text{ext}} - \xi_{\text{int}}\right](x_i - x_j), \tag{5.7}$$

where ξ_{ext} = 0 V m^{-1} is the external electric field. The internal electric field, which is caused by the built-in voltage resulting from the difference in work functions of the electrodes $\Delta\phi$ = 0.5 V, was included through $\xi_{\text{int}} = \Delta\phi / d$, where d defines the distance between the electrodes. The reorganization energy λ_{ij} was assumed to be twice the polaron binding energy λ_{ij} = 0.25 eV [109]. In addition, we ensured that the charge can recombine with the rate w_{rec} = 10^{-6} ps^{-1}, in case an electron and a hole are located on adjacent sites.

To calculate the charge current density at position **r** at time t, we made use of the following equation [92]:

$$\mathbf{J}(\mathbf{r},t) = \rho(\mathbf{r},t)\,\mathbf{v}_d(\mathbf{r},t), \tag{5.8}$$

where $\mathbf{v}_d(\mathbf{r},t)$ is the average drift velocity of the charges and

$$\rho(\mathbf{r},t) = q\,n(\mathbf{r},t), \tag{5.9}$$

is the charge density with n (**r**; t) as the number density and q as the charge.

Finally, we considered the system to be equilibrated, when the deviations in the values of the exciton dissociation efficiency, charge transport efficiency and exciton lifetime did not exceed the preset error of 0.1 % within a certain time-span in the production phase of the simulation.

5.3.2 Results and discussion

We start the analysis of our simulation results by considering the structural characteristics of the phase-separated PFB-F8BT blend. In Figs. 5.3 (a) and 5.3 (b) we plot the corresponding morphologies for the field-based and particle-based simulations, respectively. Both calculation procedures provide the lamella-like nanostructures, consisting of three phase separated domains, oriented vertically. Moreover, by analyzing the space distributions of the hopping sites, we see that the domain sizes in both morphologies are identical. However, instead of the sharp boundaries, which we observe in case of the field-based morphology, the atomistic structure is characterized by a region of smooth change of the monomer concentrations between the pure phases, possessing large number of DA contacts. From this results, we conclude that by replacing the particle-based with the field-based algorithm, we retain the sizes and the space distribution of the D/A domains, but, at the same time, we lose a significant part of the information concerning the interfacial structure. However, from Fig. 5.3 (c) we deduce that the distributions of the volume fractions in the SCFT morphology and the full-atomistic structure are in good agreement.

In the next step, we calculated the values of the exciton dissociation efficiency, charge transport efficiency, and internal quantum efficiency for both the field-based and particle-based morphologies. The resulting values together with the values of the exciton diffusion lengths are summarized in Table 5.1. Due to the small interfacial area, the value of EDE for the field-based morphology reaches only 21 %. At the same time, because of the absence of the morphological defects in the field-based representation, which, as we have shown in chapter 4, are responsible for the charge losses, all generated charge carriers are efficiently collected at the electrodes. By contrast, the value of the EDE for the particle-based morphology with the same domain sizes is about 2.95 times higher, than for the field-based morphology, whereas the observed reduction of the CTE reaches 30 %. From As a result, we find that the neglect of the DA mixing within the polymeric morphology leads to an underestimation of the resulting value of IQE by the factor of 2.1. Moreover, we deduced from the table that there is a reduction of the exciton diffusion length by 3 nm in the particle-based representation, which might indicate the extensive exciton dissociation away from the visual domain boundaries. To study the last phenomenon in more detail, we computed the

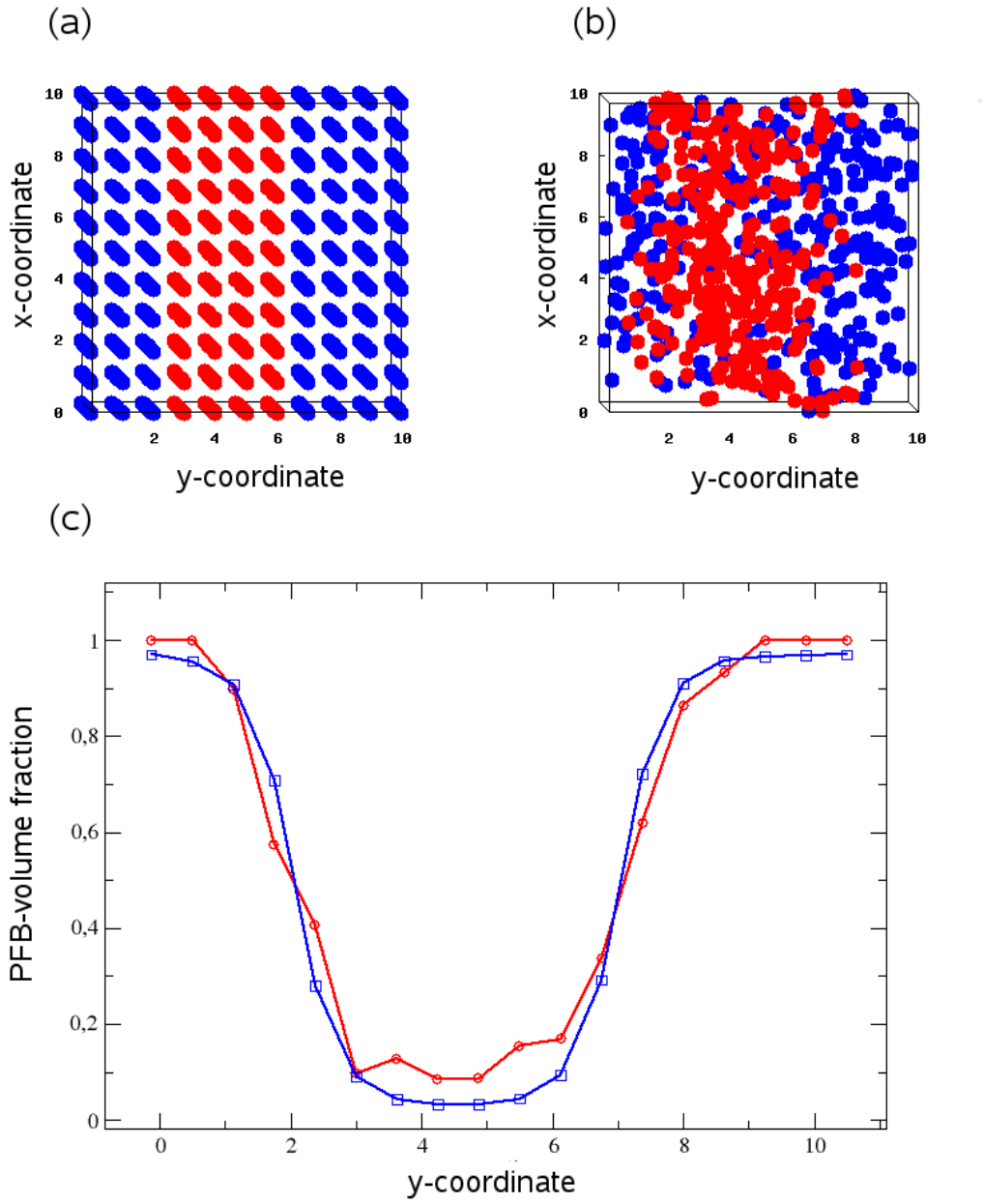

Fig. 5.3: Spatial distribution of the D- and A-type of monomers of the lamellar-like DA-polymer blend PFB-F8BT, obtained for the (a) field-based or (b) atomistic approach [red: A-phase majority contribution (electron-conducting); blue: D-phase majority contribution (hole-conducting)]. (c) PFB-volume fraction of the lamellar-like DA-polymer blend PFB-F8BT as a function of the grid number in vertical direction to the DA interface, obtained either from the atomistic (red curve) or field-based approach (blue curve).

spatial distributions of the exciton dissociation frequency for both field-based and particle-

Morphology	EDE (%)	CTE (%)	IQE (%)	D_{exc} (nm)
Field-based	21.0	100.0	21.0	8.1
Particle-based	61.9	70.0	43.3	5.1

Table 5.1: Exciton dissociation efficiency EDE, charge transport efficiency CTE, internal quantum efficiency IQE as well as exciton diffusion length D_{exc}, calculated either for the field-based or particle-based morphology

based morphologies. The resulting data is provided in Figs. 5.4 (a) and (b), respectively. Unlike in the field-based morphology, in which the exciton dissociation is restricted to occur only at the visual DA boundaries, we observe in our particle-based simulations the presence of the exciton dissociation events almost all over the structure. Moreover, we calculated the frequency of the exciton dissociation events as a function of PFB volume fraction and visualized the resulting data in Fig. 5.4 (c). By analyzing the curve, we pointed out that the maximum of exciton dissociation frequency of 0.0023 is observed at the visual domain boundaries, corresponding to the PFB volume fraction of 0.5. However, in the range of PFB concentrations from 0.1 to 0.8, we see that the quantity oscillates between the values 0.0016 and 0.0023. These simulation results support our previous statement that the exciton dissociation mainly takes place away from the visual DA domain boundaries. Moreover, we explain the relative reduction of the exciton dissociation frequency by the slowing down of the charge motion across the region, causing in turn the losses of available DA contacts. This conclusion is supported by the experimental findings of Coffey and Ginger [78, 92], who observed through time-resolved electrostatic force microscopy on their PFB-F8BT blends that slower charging, takes place near the microscale domain boundaries and that the bulk of the photocurrent is generated in regions away from the visible domain interfaces. They inferred from their observations with regard to the long-standing debate of whether the mesoscale domain interfaces or the domain centers [113] are responsible for most of the photocurrent generation in these model blends that it is the domain centers. Moreover, they deduced from their data that the composition of the phase separated domains can have a potentially stronger effect on the device performance than the observable mesoscale film morphology and that

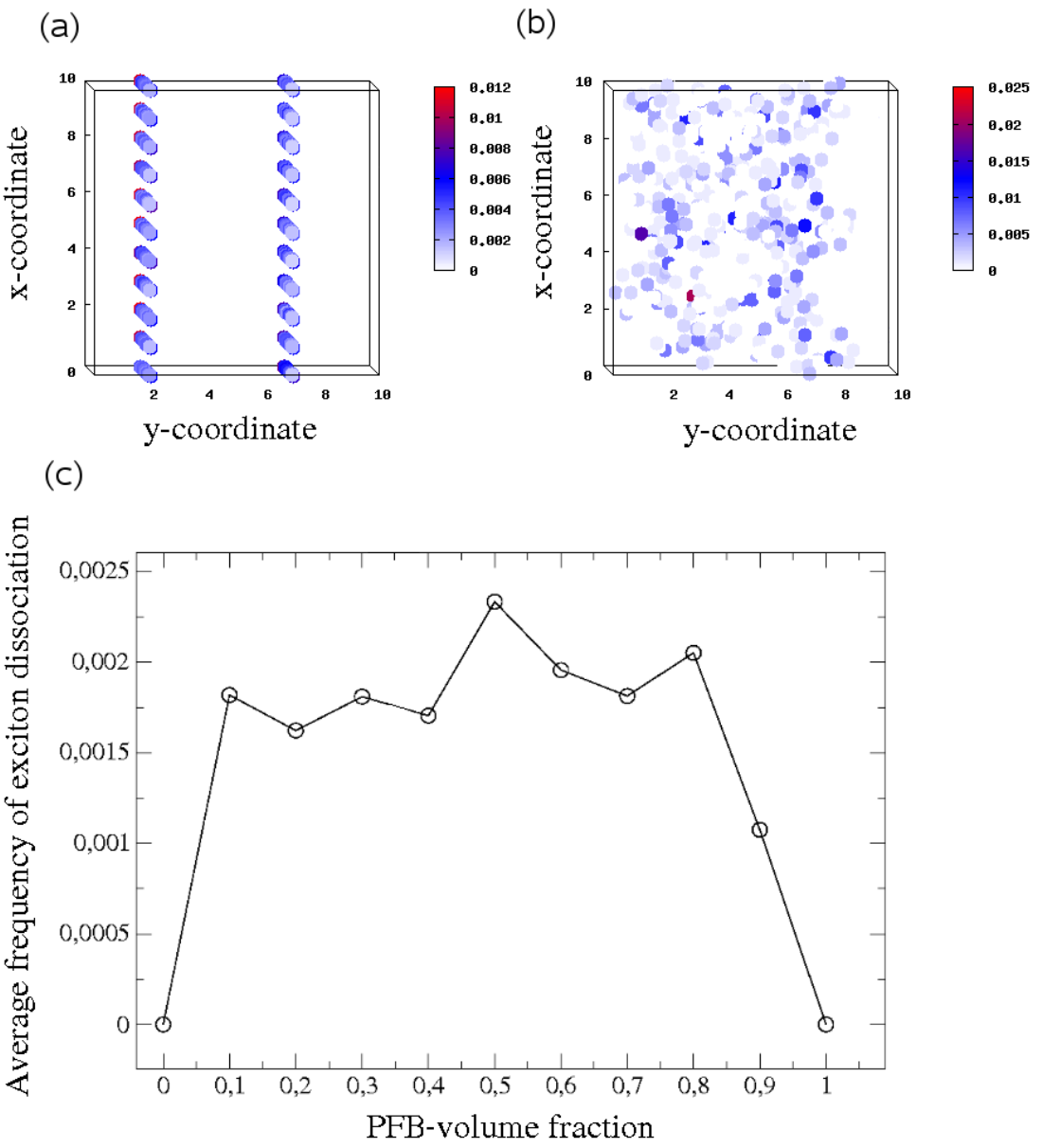

Fig 5.4: Spatial distribution of the exciton dissociation frequency of the lamellar-like DA-polymer blend PFB-F8BT, obtained for the (a) field-based or (b) atomistic approach. (c) Average frequency of exciton dissociation of the lamellar-like DA-polymer blend PFB-F8BT, obtained from the atomistic approach, as a function of the PFB-volume fraction.

optimizing the charge carrier transport and recombination rates within these domains through controlling the domain composition could improve the photovoltaic performance [92].

Furthermore, to investigate the influence of the DA mixing on the flow of charge carriers across the polymeric morphology in more detail, we calculated the values of current

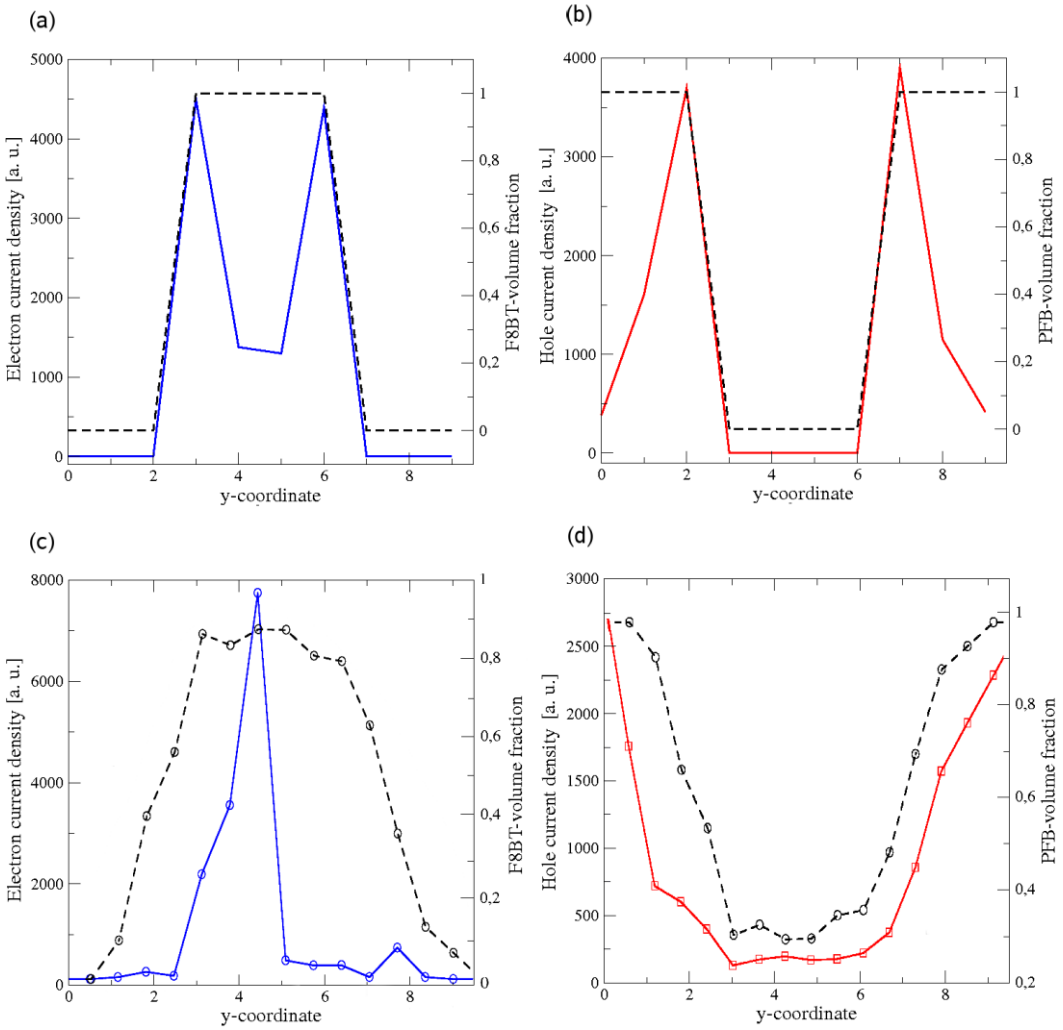

Fig. 5.5: Current densities (solid line) and volume fractions (dashed line) from the lamellar-like DA-polymer blend PFB-F8BT as a function of the y-coordinate, vertical to the DA interface. (a) Electron current density or (b) hole current density in conjunction with the corresponding volume fraction of the charge-transporting monomers, obtained by using the field-based approach. (c) Electron current density or (d) hole current density in conjunction with the corresponding volume fraction of the charge-transporting monomers, obtained by using the particle-based approach.

densities over the morphologies for both electrons and holes as a function of the y-coordinate. The resulting distributions together with the distributions of volume fractions of the corresponding polymers are plotted in Fig. 5.5. Our results suggest that the main contribution to the photocurrent in the field-based simulations comes from the DA boundaries, as shown in

Figs. 5.5 (a) and 5.5 (b). We explain this effect by the electrostatic attraction between adjacent electrons and holes in both phases along the interface, accompanied by the neglect of the mixing of the D- and A-type of monomers in the calculation of the charge transfer rates. By contrast, the highest values of the current density in case of the particle-based morphology are observed in the centers of the DA domain for both electron and hole motion, as depicted in Figs. 5.5 (c) and 5.5 (d). This is caused by the increase of the distances between the monomers of the same type with increasing degree of mixing in the polymer blend, leading to the decrease of the electronic coupling between the sites. As a consequence, the slowing of the charges near to the DA interface causes the increased number of charge recombination events. These findings are confirmed by the experimental investigations of Marohn *et al*. [92, 114], who studied PFB-F8BT films using photopotential fluctuation spectroscopy. From their data, they deduced that the inter-mixing of phases leads to electron trapping in F8BT inclusions of PFB-rich regions, resulting in a poor mobility of the electrons and, ultimately, in a decreased efficiency of the solar cell device. Moreover, these results explain the reduction of the CTE in the particle-based morphology [92].

To summarize, we observed that the DA mixing is responsible for the doubling of the IQE in the lamellar-like nanostructures in comparison to the morphology with the same domain size, but without consideration of the minority fraction. The main source of the IQE increase was found to be the extensive exciton dissociation away from the visual domain boundaries. Moreover, by analyzing the distributions of the current densities over the field-based and particle based morphologies, we deduced that the mixing of D- and A-monomers provides the driving force for the charge diffusion to the domain centers, in agreement with the findings of McGehee [115]. These simulation results indicate that the highest contribution to the collected photocurrent in the lamella-like nanostructure comes from the domain centers and may question a number of simulation results, earlier published in the field, where the effect of DA mixing was not taken into account.

In the following let us discus in which cases the field-based or particle-based simulation approach should be used for investigating the photovoltaic processes in organic solar cells. From the previous investigations, we deduce that this depends on the system size and properties under investigation. This requires an algorithm with an appropriate scale of representation and specification level. Moreover, in present chapter, we showed that for the

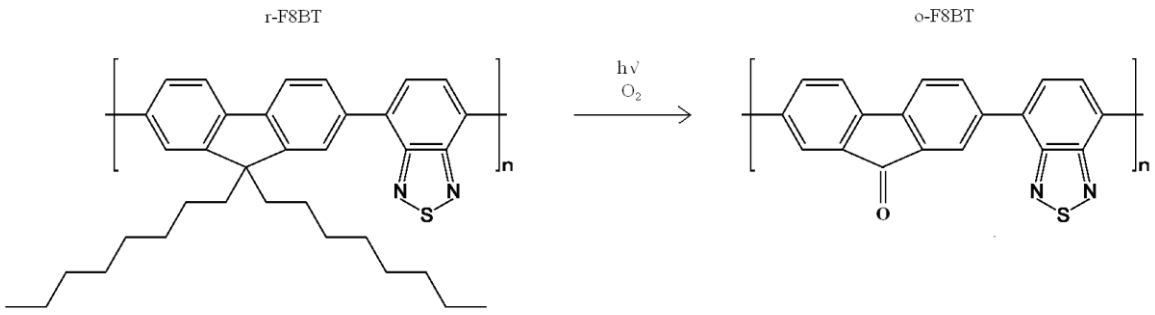

Fig. 5.6: The process of F8BT photo-oxidation, leading to the formation of the corresponding fluorenone derivative.

small lamellar-like nanostructures the field-based algorithm provided a poor description of the system behavior. However, we expect that both field-based and particle-based algorithms come into agreement for the morphologies with larger domain sizes and smaller DA interface. We should also note that the particle-based simulation approach requires significantly more computational efforts, which limit the scope of application to systems with the sizes of about 20 nm. On the other hand, there are various effects, which cannot be studied at the classical level of description without using the transport parameters, obtained from quantum calculations. One of these effects, the photo-oxidation of the polymeric chains, will be considered in this chapter.

To study the influence of photo-oxidation on the solar cell performance with our particle-based algorithm, we generated a set of nanoscale morphologies, stepwise increasing the average concentration of photo-oxidized F8BT monomers from 0 % to 40 %. In Fig. 5.6 we provide the underlying chemical reaction of the photo-oxidation of F8BT monomers. The results of the corresponding solar cell simulations are shown in Fig. 5.7 (a). From the graph, we deduce that the efficiency of electron transport process decreases about 30 % through increasing the concentration of fluorenone defects in the F8BT phase from 0 % to 40 %. This shows that photo-oxidation has a major influence on the CTE of such polymer solar cells. To demonstrate that this deterioration of the CTE is caused by charge trapping induced by keto-defects, we show in Fig. 5.7 (b) the ratio of the numbers of inter-molecular through intra-molecular hops as a function of the fraction of photo-oxidized F8BT monomers for the

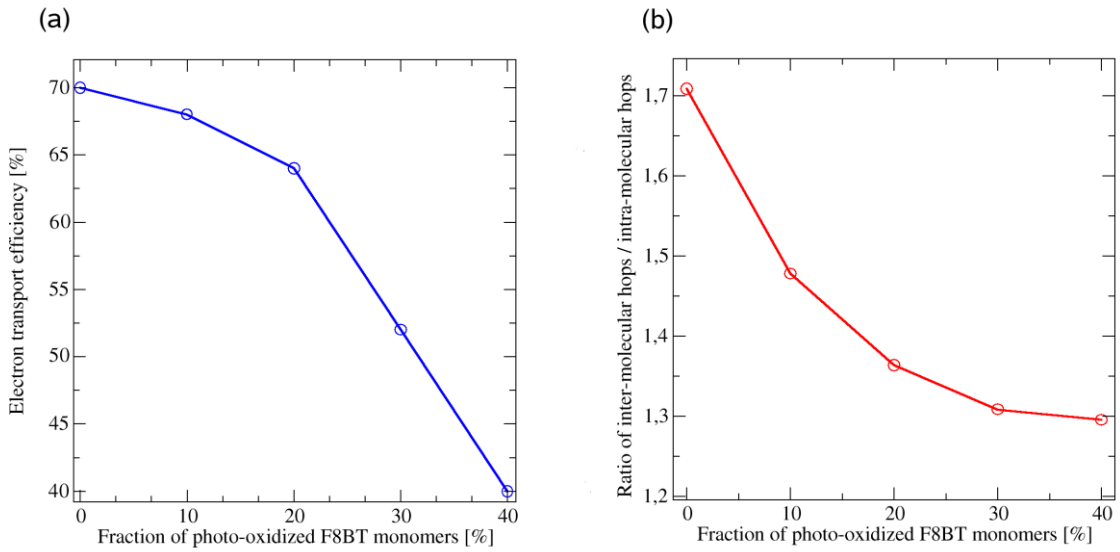

Fig 5.7: (a) Electron transport efficiency and (b) ratio of the numbers of inter-molecular hops through intra-molecular hops as a function of the fraction of photo-oxidized F8BT monomers for the lamellar-like DA-polymer blend PFB-F8BT.

lamellar-like DA-polymer blend PFB-F8BT. We observe that the quantity decreases with growing concentration of fluorenone defects. From these findings, we conclude that the keto-defects lead to a localization of the electron transport on the same chains, which can be interpreted as a keto-induced charge trapping on the polymer chains [92]. For the considering PFB-F8BT blends, the influence of the photo-oxidation on the photovoltaic performance was studied by Reid *et al*. [92, 98], who found using time-resolved electrostatic force microscopy that the overall device efficiency decreases rapidly with increasing duration of light- as well as air-exposure. We note that our results are in agreement with the experimental findings of Reid *et al*. [98]. Moreover, they are supported by the results of Noh *et al*. [116, 117], who has demonstrated on fluorene-based field-effect transistors that photo-oxidation of the fluorene units leads to electron-trapping through the formation of fluorenone defects, reducing the charge carrier mobility. However, in all these works the trap formation kinetics could not be resolved as a function of the local morphology [92, 98]. In Fig. 5.8 we show the spatial distributions of the current density, associated with the motion of electrons (ECD), resulting either from the intra-molecular or inter-molecular hops for the lamellar-like polymer-blend

PFB-F8BT with F8BT in the photo-oxidized form (o- F8BT) and reduced form (r-F8BT). We point out that by the photo-oxidized case we imply our simulation results, obtained on the morphology with the fraction of fluorenone-type of monomers of 40 %. From the Figs. 5.8 (a) and 5.8 (b), we deduce that the intra-molecular ECD of the o-F8BT phase is higher compared to the one of the r-F8BT phase. This relates to the fact that the oxygen on the fluorenone leads to an attraction of the electron density on the bridging unit between two benzo-thiadiazole (BT) units. As a result, this increases the probability of intra-molecular charge transfer and, thus, augments the intra-molecular ECD on the polymer chains. Moreover, a keto-defect causes an overall contraction of the electron density on the respective o-F8BT-polymer chain and in this way leads to a reduced coupling between BT units on different chains compared to the r-F8BT species. As a consequence, this results in a reduced inter-molecular ECD in case of the o-F8BT form compared to the r-F8BT form, as can be concluded from the Figs. 5.8 (c) and 5.8 (d). Moreover, by subsequently comparing the intra- and inter-molecular ECDs of the photo-oxidized and reduced species, we infer that an increase in the intra-molecular contribution to the ECD goes along with a decrease of the respective inter-molecular contribution. Since in both cases the inter-molecular hopping events are the rate-limiting processes determining the overall ECD, this antagonistic effect causes that the CTE deteriorates about 30 % in the o-F8BT case with a fraction of 40 % of photo-oxidized F8BT monomers compared to the r-F8BT case, as revealed in Fig. 5.7 (a) [92]. This results agree well with the quantum-chemical calculations of Van Vooren *et al*. [118], who showed that, despite the large separation between two adjacent BT units on the same chain (ca. 1.3 nm between the centers of the BT units), the corresponding charge transfer integral has a significant magnitude as a result of through-bond coupling via the bridging fluorene units. The electronic coupling associated with inter-chain transport strongly depends on the relative positions of the BT units, where the largest values are found for quasi-cofacial structures with the two BT units pointing in the same direction. By contrast, inter-chain transport for F8BT polymers in an alternate configuration is much less efficient although it is assisted by slight delocalization of the LUMO level over the fluorene units. This situation is encountered in the

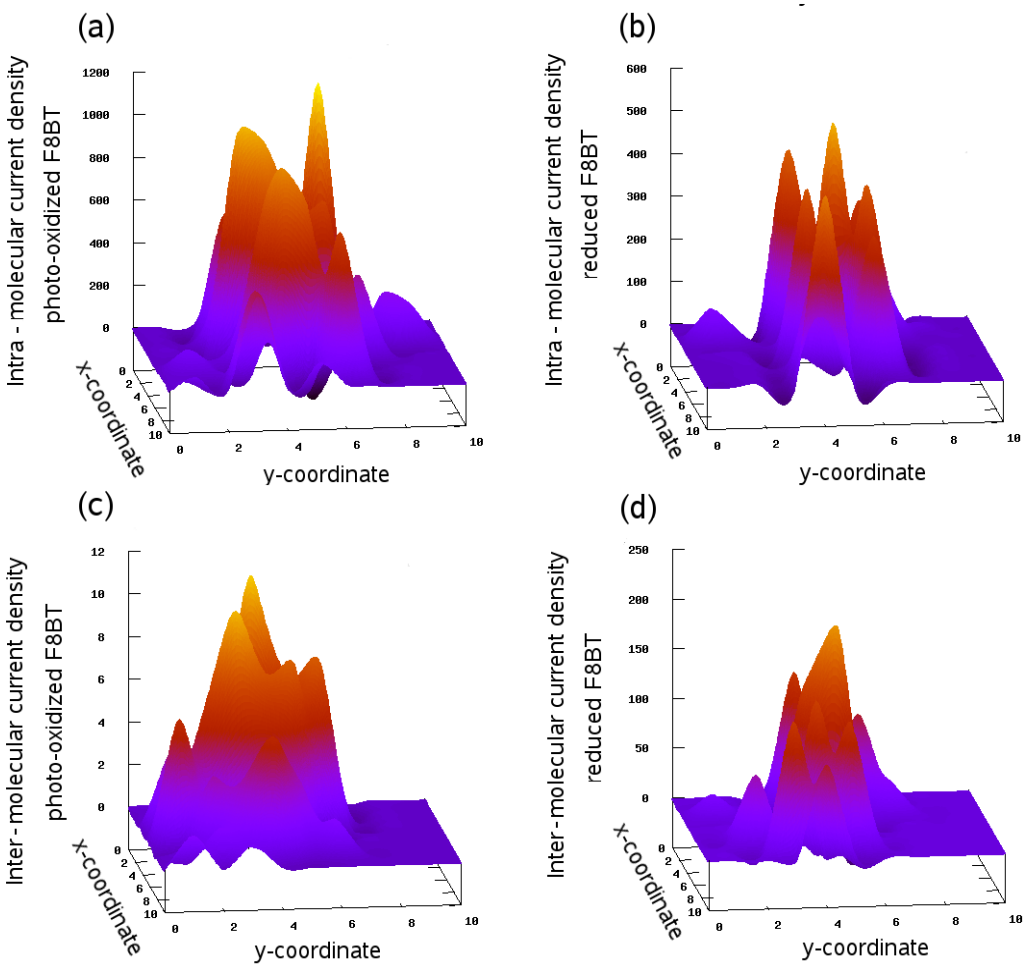

Fig 5.8: Spatial distribution of the intra-molecular contribution to the electron current density for the lamellar-like DA-polymer blend PFB-F8BT with F8BT in the (a) photo-oxidized form and (b) reduced form. Spatial distribution of the inter-molecular contribution to the electron current density for the lamellar-like DA-polymer blend PFB-F8BT with F8BT in the (c) photo-oxidized form and (d) reduced form. The results for the photo-oxidized case correspond to a fraction of photo-oxidized monomers from F8BT of 40 %.

polymer blend, considered in our work. There, many different non-ideal non-cofacial configurations render the inter-chain electronic transport less effective than the intra-chain electronic transport. Moreover, in the photo-oxidized case the keto-defect on the bridging fluorene moiety causes that the electronic coupling between different BT units on the same chain becomes stronger, which improves the intra-chain electronic transport but impairs the inter-chain electronic transport at the same time. This effect results in the keto-induced

trapping of electrons on the same chain, reducing the overall efficiency of electron transport [92].

6. Improvement of organic photovoltaic performance via chemical control of interfacial structure between D- and A-phases

In present chapter we examine the possibility to enhance the performance of polymer based solar cells by changing the composition of DA-mixed regions. To achieve this goal, we vary the degree of tapering at the chemical junction of the D- and A-block of the diblock-copolymer molecules and study its influence on the device efficiency. To this end, we start by describing of morphology optimization procedure from the theoretical and experimental sides and show the disagreement between both approaches. Furthermore, we introduce our novel CG-to-FG transformation technique, enabling to treat large monomeric units. Finally, we show and analyze the solar cells simulation results and identify the optimal degree of tapering for the photovoltaic performance.

6.1 Tapered block-copolymer technology for solar cell optimization

The optimization of nanoscale polymeric morphology is a well-known strategy, permitting to achieve a significant increase in the performance of BHJ organic solar cells for a given polymer composition. During the last decade, several production and post-production treatment techniques were extensively discussed in the literature, primary, in experimental studies. Among these techniques, the thermal annealing, the solvent annealing, and the alignment under the electrical field can be considered as the most important approaches. Moreover, together with the successes of these experimental techniques, the growing computational power of supercomputers induced many theoretical studies with the goal of exploring the influence of polymer morphology on the performance of organic photovoltaic devices. The advantage of theoretical approach is that it enables to investigate the influence of specific characteristics on the device efficiency. The question is only which characteristics should be optimized to enhance the performance of OPV cells? The problem is that the experimental studies cannot distinguish between the contributions of different effects, and, in this sense, the morphology optimization means the entire complex of changes, associated with

an application of different production and post-production treatment techniques. Since the fabrication processes cannot be fully reproduced in theory, in this case, the morphology optimization usually means the optimization of D- and A-domain sizes and the geometry of the active layer. On the one hand, this point of view is supported by the experimental evidences, suggesting that the losses of the excitons and charge-carriers can be minimized by keeping the polymer domain sizes in the range of exciton diffusion length (~10 nm) [119]. On the other hand, several recent studies indicate that the composition of the visual D and A domains, varying due to the mixing of the D- and A- polymers, can be even of greater importance [120, 121, 121].

In the previous chapter we have shown the impact of DA mixing at the interface by comparing the field-based and the particle-based simulation strategies. These results revealed that by neglecting the existence of mixing regions, the important information on the system behavior is lost, since the presence of the component minorities drastically changes the values of EDE, CTE, and even shifts the maximum of current density from the interfacial regions to the centers of domains. In present chapter, we develop this concept further and examine the possibility to improve the device efficiency by controlling the interfacial structure between the D- and A-phases. However, if we assume that the transport properties of excitons and charge-carriers are dependent on the phase composition, a molecular description of large polymeric systems will be required. For this, we will introduce a novel simulation technique to bridge the length- and time-scales of interest. With this new approach, we investigate the photovoltaic efficiency of the device, whose active layer consists of tapered block-copolymers with different length of tapered middle block.

A chain of a tapered block-copolymer molecule represents a linear block-copolymer, composing of two regular outer blocks and a middle block, in which the monomers of the end blocks are statistically distributed at the interface between the blocks. In the past decades, these molecules have been investigated in context of their outstanding physical properties in comparison to the standard diblock- and triblock-copolymers, such as, for instance, the low order-to-disorder transition temperature [123]. In application to solar cell technology, the tapered block-copolymers are also considered as promising materials due to their ability to form bi-continuous double-gyroid nanostructures [124]. However, no investigations of the tapered block-copolymer solar cells with a specific focus on the changes of the phase

composition on the local scale were performed up to now. At the same time, several investigations have been performed for studying the physical and chemical properties of tapered block copolymers. Of interest in this regard are the experimental results of Hodrokoukes *et al.* [125], who studied the influence of composition gradients on the microdomain structure. The authors point out that tapered block-copolymers can efficiently be used to control the polymer compatibility, and, hence, the interfacial structure, at the synthesis level. Moreover, they observed that for certain chain architectures, the phase separation process of the tapered block-copolymers results in the formation of lamellar-like nanostructures. In addition, Kuan *et al*. [126] have recently shown that the tapering of the diblock-copolymer can be achieved with retaining the initial phase-separated polymeric morphology. All these results together with the results of Yan *et al*. [94], already discussed in chapter 5.1, indicate that by controlling the length of the tapered middle block, the efficiency and mechanical stability of the diblock-copolymer photovoltaic devices may potentially be improved already at the synthesis level.

6.2 Coarse-grained to fine-grained transformation for the tapered block copolymers

To perform solar cell simulations for the tapered block-copolymer systems, we improved a part of our particle-based solar cell algorithm, enabling the transformation between CG and FG structures. The first reason, why these improvements were required, was the difficulty of performing the transformation for large monomer units by using the standard methods. In these methods, it is assumed that the CG to FG transformation can be carried out in two steps: (1) the atoms, corresponding to the FG structure, are placed into a certain Van-der-Waals radius around the center of mass of the CG bead and (2) the resulting structure is optimized to prevent the overlap of the atoms. For small monomers, containing less than 10 atoms, the procedure works well, however, when the number of atoms reaches the 147, as we have it in case of the monomer of PFB, the resulting value of the potential energy is so large (more then 10^{20} kJ/mol in comparison to the value of ~10^{5} kJ/mol for the equilibrium structure) that the energy minimization procedure cannot even be started. In our previous research, we overcome this problem by introducing the intermediate CG structures, stepwise

increasing the level of molecular specification. This solution, however, was also far from the ideal, since it required the determination of the interaction parameters for every newly introduced CG bead. We notice that these parameters can be obtained by using the program package VOTCA [127]. However, according to our experience, the calculation of the correct CG interaction parameters, especially, the Lennard - Jones parameters, is a very time consuming procedure, which for the non-spherically symmetric monomers may not always properly work. Moreover, the use of approximate parameters might also lead to changes in the conformation of the polymeric chain and cause significant rearrangement of the polymers within the morphology.

On the other hand, to get an equilibrium distribution of polymeric chains at the atomistic scale we made use of MD simulations. The problem is that the standard MD simulation approach together with the energy minimization procedure implies that all bonded and non-bonded interactions between the atoms are specified before the simulations are carried out. This information is usually stored in a separate file, which is called the topology file. To construct such a file, the GROMACS simulation package provides a tool, which requires the sequence of atoms and the bonds between them as an input parameter. However, due to the statistical nature of the polymeric sequences in tapered block copolymers, neither the sequence of atoms nor the bonds between them can be predefined. Moreover, some of the existing computational tools enable to construct the molecular topology by analyzing the atomistic coordinates, but the search algorithms in these tools are based on the analyses of the distances between the atoms. Consequently, for these methods, the equilibrium structure of the polymeric chain is required. As we have shown during the discussion of the CG to FG transformation, the equilibrium structure of the polymers can be obtained only after the energy minimization procedure, and, therefore, these methods are also not appropriate for our investigations.

To solve both of the outlined problems, we developed a tool, enabling the CG to FG transformation for the tapered block-copolymer systems. The procedure consists of the following steps:

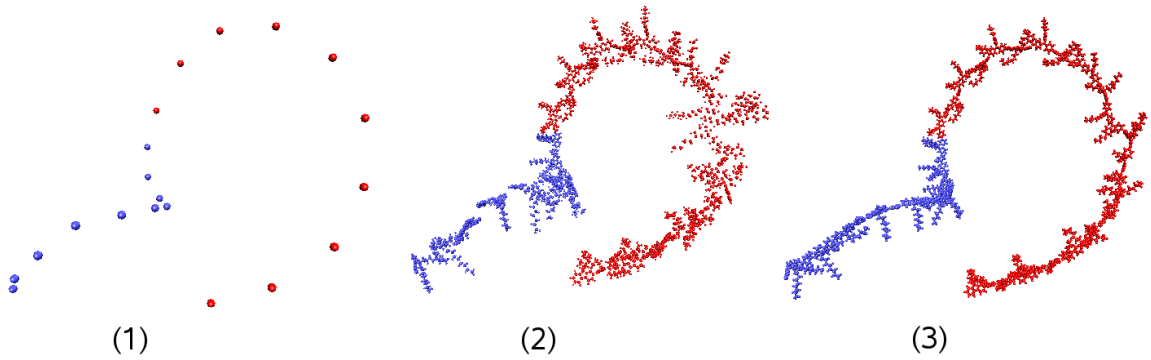

Fig. 6.1: Illustration of the steps of CG to FG transformation procedure for the tapered block-copolymer chain $D_9R_2A_9$, composed of PFB and F8BT units: (1) sequence formation, (2) generation of FG structure, and (3) optimization through minimization.

1. Random tapering of the middle block on the CG polymeric structure by replacing the D- and A-monomers with the opposite A- and D-monomers, respectively, with the probability of 0.5;
2. Replacement of the CG beads by the corresponding equilibrium structures of FG monomers, ensuring the right orientation of the monomers;
3. Optimization of the resulting structure through minimization.

In Fig. 6.1 we show the results for the CG to FG transformation of tapered block-copolymer chain $D_9R_2A_9$, composed of PFB and F8BT units, obtained by using our algorithm. We start with the analysis of the monomeric sequence of the diblock copolymer under consideration, for which we perform the modifications, associated with tapering. For every monomer inside the tapered middle block, we generate a uniformly distributed random number X [0, 1] and compare it to the value of the acceptance probability of 0.5, ensuring in turn the equal average concentrations of both types of monomers in the system. In case if the random number exceeds the value of 0.5, we switched to the next CG bead. Otherwise, we replaced the monomer by the monomer of opposite type, i.e. the D-monomer was replaced by the A-monomer and vice versa. As soon as we have generated the CG structure of the tapered polymeric chain (Fig. 6.1 (1)), we performed the CG to FG transformation. To get the right orientation of the monomers, we partitioned the chain into three parts: the first part, corresponding to the first monomer of PFB, the second part, consisting of all the other

monomers, except the last monomer, and the third part, represented by the last F8BT monomer. Furthermore, we performed the optimizations of four structures, corresponding to the first monomer of PFB, the intermediate monomer of PFB, the intermediate monomer of F8BT as well as the last monomer of F8BT. Each of the optimized monomer structures was placed inside the corresponding CG bead by superpositioning the centers of mass of the CG beads and the monomers. Next, we performed the rotations of every monomeric unit with respect to the tangent vectors, which we computed for the corresponding CG beads. Moreover, we associated the tangent vectors for the first and the third part of the polymeric chain with the directions of the neighboring bonds, whereas the vectors for the monomers in the second part were calculated by using the coordinates of the previous and the next CG beads. In Fig. 6.1 (2) we visualize the resulting FG structure. Finally, we performed the optimization of the structure, provided from step (2), through the energy minimization. The resulting structure (3) was plotted in Fig. 6.1 (3). Note, that unlike in the above mentioned standard methods, the convergence criteria for the energy optimization procedure in this case was reached very rapidly, since only the small rearrangements, associated with the adjustment of the bonds between the monomers, were required. Moreover, we demonstrated that the resulting FG polymeric chain perfectly matched the initial CG structure.

Concerning the issue of the topology construction for the tapered block copolymers, this problem is also solved within our algorithm. Since we subsequently introduce the monomers with the predefined atom sequences, for the topology of the entire polymeric chain, we replicated the atomic sequence for the given monomers and stored them to a separate file. The same procedure was performed for the bond sequences. The only necessary modifications of the resulting file were renumbering the atoms in the appropriate order and adding the connections between the monomers. By using this data, the complete topology file can be constructed by making use of the standard tool of the GROMACS simulation package.

6.3 Simulations of photovoltaic performance of the tapered-block copolymer solar cells

In the following we study the potential the tapered block-copolymer technology to improve the IQE of block-copolymer solar cells, which relies on the concept of controlling the

width of interfacial area between the D- and A- domains. To study the dependence of the device efficiency on the polymeric morphology, we applied the recently developed particle-based algorithm, which is based on the combination of dynamical Monte Carlo method and the particle-based structure from the polymer field theory. To investigate the influence of the interfacial width on the IQE, we generated a set of atomistic-resolved lamellar-like nanoscale morphologies, which differed from each other through the composition of the D- and A-phases. As we will show in the following, our simulation results show that for the systems, consisting of the polymers with the relatively small length of the tapered middle block, the IQE can be improved by 25 % due to the increase of EDE, while the further increase of IQE is hampered by the weak charge transport across the disordered domains. Moreover, by investigating the size dependence of the effect, we found that the increase of IQE of the tapered block-copolymer systems compared to diblock-copolymers reaches 39 % by increasing the system size about 5 times.

6.3.1 Computational details

In our study we focused on the system PFB and F8BT, connected together as block-like polymer chains. As in case of polymer blends in chapter 4 we started with the generation of the nanoscale polymeric morphologies for the diblock-copolymer $D_{10}A_{10}$. To accomplish these simulations, the Flory-Huggins interaction parameter between the monomers was computed from the corresponding Hildebrand solubility parameters, resulting in the value of 0.337 [92]. Moreover, for the numerical integration of the Fokker-Plank equation, a two-dimensional space grid of 10 x 20 nm^2 was used. Furthermore, by using the computed equilibrium segment densities and density biased Monte Carlo technique, we transformed the obtained field-based morphology to the particle-based representation. To accomplish the transformation, we associated the conjugated segments in the field-representation with the single D- and A-monomers in the particle-representation. As a result, the coarse-grained representation of the equilibrium morphology, mimicked by the space distribution of 80 diblock-copolymer molecules, was obtained.

To obtain the atomistic representation of the polymeric chains, we made use of the CG to FG mapping technique, introduced in chapter 6.2. In our simulations, we introduced the atomistic details by inserting the monomers in their equilibrium geometries at the positions of the corresponding coarse-grained beads, ensuring both the connections between the appropriate atoms of different monomers and the right orientation of the obtained chains. This procedure was accomplished by the rotation of the initial monomer structures with respect to the tangent vector, computed for every CG bead. Moreover, the tapering of the initial diblock copolymer was also introduced at this stage. Note, that by the tapering of the diblock molecules we assume the modification of the polymeric chain, leading to the formation of the polymer architecture of the general form $D_{10-k}R_{2k}A_{10-k}$, where R refers to a tapered middle block of different length with equal average concentration of the D- and A-monomers, while k is an integer number. The energy of the obtained FG structure was minimized with the parameters, taken from the OPLS-AA force-field [128]. After the minimization, the morphologies were equilibrated under NpT ensemble by using the Nose-Hoover with Δt = 1 ps thermostat and Parrinello-Rahman barostat with Δp = 1 ps [129]. In our simulations, the equilibration phase took 5 ns at 298.15 K. Furthermore, to take into account the effect of thermal fluctuations on the device efficiency, we sampled 25 configurations from 2 ns of the production phase with the equal time intervals of 80 ps.

The efficiencies of the photovoltaic process were estimated by performing DMC simulations, which means use of the first reaction method [92], on every sampled configuration. Exciton generation rate of $2 \cdot 10^{-6}$ ps^{-1} was computed from PFB-F8BT absorption spectra under AM 1.5 illumination, while the exciton motion was described by Förster theory, described in chapter 2.1. The dependence of charge transport rates on the properties of the environment was described by the equation of Marcus theory (see chapter 2.5), while the site energy difference was calculated with respect to the build-in field, the Coulombic interactions between the charge-carriers, and the image charge effect [92]. The value of reorganization energy of 0.25 eV was assumed to be independent on the local environment changes. The charge transfer integrals were calculated by using the dimer projection method with the well-established ZINDO approximation [36]. The charge recombination rate of 10^{-6} nm was taken from the literature [21].

Polymer type	A	B
PFB	4.3	$1.2*10^{-4}$
F8BT	5.7	$8.4*10^{-6}$

Table 6.1: The dependencies of the transfer integrals on the distances between the monomers in the PFB-F8BT lamellar-like nanostructure, obtained by assuming the exponential fit function J(r) = A*exp(-B*r).

To study the dependence of the efficiency improvement on the system size, we calculated the distributions of the transfer integrals over the simulation trajectories as a function of the distances between the corresponding monomers. Furthermore, these dependencies were fitted by assuming the exponential decay of transfer integrals as a function of the distances and used to replace the quantum chemical calculations. The resulting parameters were summarized in Table 6.1. In addition, to obtain the atomistic morphologies of larger sizes, we replicated the equilibrium morphologies with respect to the direction of the electrodes an appropriate number of times.

6.3.2 Results and discussion

We start the analysis of our simulation results by considering the phase separation process of the PFB and F8BT system previously introduced. The field-based morphology, corresponding to the $D_{10}A_{10}$ diblock-copolymer system is shown in Fig. 6.2 (a). By analyzing the diagram, we observe that for the given system size and polymer composition, the resulting morphology is a lamellar-like nanostructure with 7 separate D- and A-domains, oriented vertically. However, instead of the sharp interfaces between the D/A domains, we see smooth changes in the polymer concentrations already for the diblock-copolymer system. This observation is caused by the relatively low value of the χN – product, defining the degree of phase separation in the SCFT. On the other hand, it shows that the mixed regions are present even in the ordered morphologies. Furthermore, by analyzing the results of the density biased

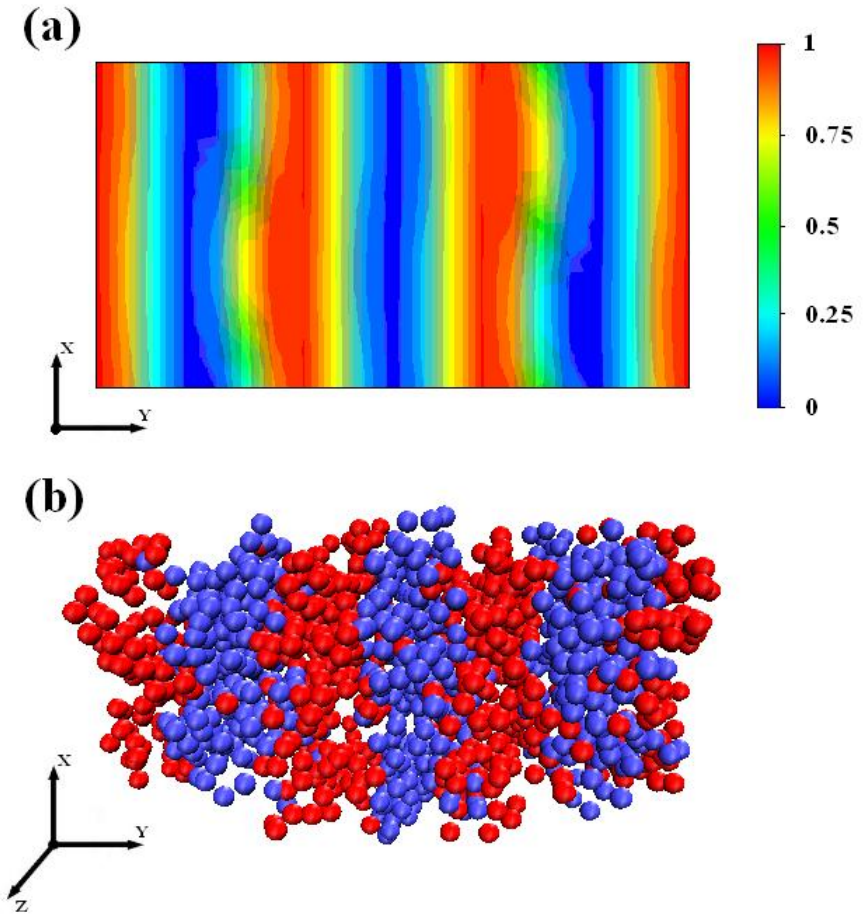

Fig. 6.2: Spatial distribution of the D- and A-type of monomers of the lamellar-like DA-block copolymers PFB-F8BT, obtained by the (a) SCFT simulations and (b) density biased Monte Carlo [red: A-phase majority contribution (electron-conducting); blue: D-phase majority contribution (hole-conducting)]

Monte Carlo procedure, which we depict in Fig. 6.2 (b), we conclude that the obtained particle-based morphology perfectly matches the morphology in the field representation. This indicates that by combining the SCFT and the density biased Monte Carlo method, we can cope with the time-scales of practical interest for the particle-based systems. At the same time, we note that the equilibration phase leads to the reduction of the absolute size of the particle-based morphology from 20 nm to 17.6 nm with respect to the y-direction. We point out that the change of the system size was observed due to the missing experimental density value for the PFB-F8BT tapered block copolymer, required as input parameter for MD simulations. Moreover, Ayogi *et al.* mention that the resulting gyration radii in the Gaussian

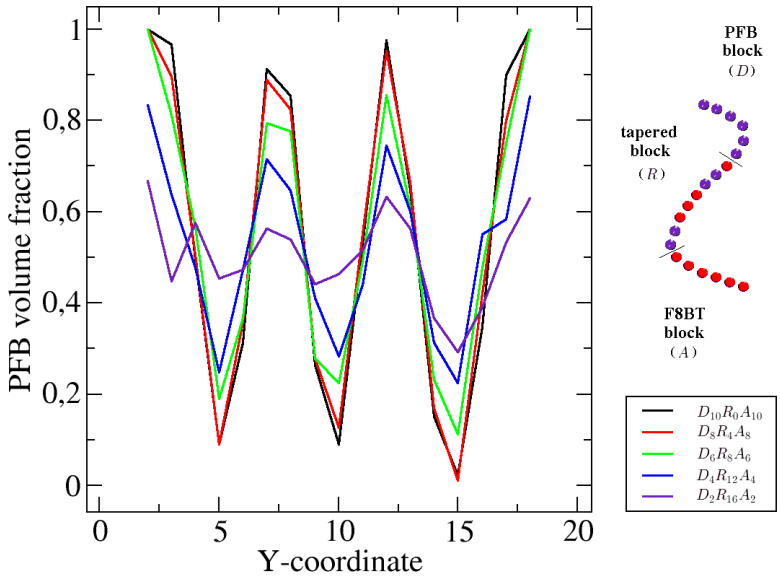

Fig 6.3: PFB volume fraction as a function of the y-coordinate in a lamellar-like DA-block copolymer PFB-F8BT for different length of the tapered middle block. Note that the y-direction represents the orientation parallel to the electrodes.

chain model and the explicit particle chain of polymers are different. They suggested that the ideal agreement between the particle-based and the field-based morphologies can be achieved by modifying the number of polymeric segments in the particle-based chain. This optimization remained beyond the scope of this thesis, however, the size matching between both representations might be part of a later work.

In the next step, we analyze the change of the polymer composition caused by the introduction of the tapered middle block of different length. To this end, we plot in Fig. 6.3 PFB volume fraction as a function of the y-coordinate for different lengths of the tapered middle block. Our results show that the tapering of the diblock-copolymer leads not only to the change of the interfacial structure, but also to the increase of mixing between the D- and A- monomers inside the visual DA domains. Moreover, we find that in cases where the lengths of the tapered blocks are in order or less than the lengths of the end-blocks, this mixing inside the phases can be considered as insignificant. In particular, for the $D_6R_8A_6$ copolymer system the maximum concentration of the opposite component inside the D/A domains reaches only 22 %, which should result in a minor reduction of the CTE. Finally, a further increase of the tapered block length leads to the strong mixing between the D- and A-

monomers, which may cause the weak a deteriorated charge transport across the corresponding phases.

In order to identify the nature of the changes in the device efficiency, associated with the increase of intermixing between the lamellar-like oriented D- and A-domains, we calculated the values of the EDE, CTE, and IQE for each of the generated morphologies. In Fig. 6.4 we visualize the EDE, CTE, and IQE as a function of the length of the tapered middle block. The results of our simulations reveal that the increase of interfacial mixing between the D- and A-segments leads to a rapid grow in the EDE from 55% to 86 %. However, we observe that after a tapered block length of 8, the curve undergoes a change in slope. In contrast, by analyzing the behavior of the CTE curve, we see that the increase of the tapered block length up to 8 causes a minor change in the value from 97 % to 83 %, while the further increase of the intermixing between the D- and A-materials leads to a drastic decay of the CTE from 83 % to 22%. The behavior of the EDE was expected, since it is *a priori* proportional to the number of the available D-A contacts. However, the reason for the changes in slopes of both EDE and CTE curves lies in the slowing of charge transport motion across the mixing regions. This, in turn, causes the accumulation of charge carriers near to the D-A interface, which both reduces the number of available contacts due to the imposed single occupation condition as well as increases the probability of bimolecular charge recombination. These simulation results are supported by the early study of Yan *et al* [94] on the bilayer-like solar cells, who found that increased DA mixing improves the exciton dissociation efficiency but, at the same time, decreases the charge transport efficiency across the region. However, due to the difference in the polymeric structures and the morphologies, we observe the maximum of the IQE for the system $D_6R_8A_6$, instead of the steady decrease in the value. Moreover, from the viewpoint of the performance improvement, we find an increase of the IQE by 25 % with respect to the untapered case. Besides, the observed reduction of exciton dissociation for the highly mixed morphologies correlates with the experimental findings of Collins et al [16]. In this work, they concluded that a mixed phase is not beneficial to exciton dissociation, but rather polymer access to pure agglomerates is important for efficient charge separation in this system.

On the other hand, the studied systems were restrained by the electrodes, and, hence, they were not periodic with respect to this direction. Therefore, we can expect that the value

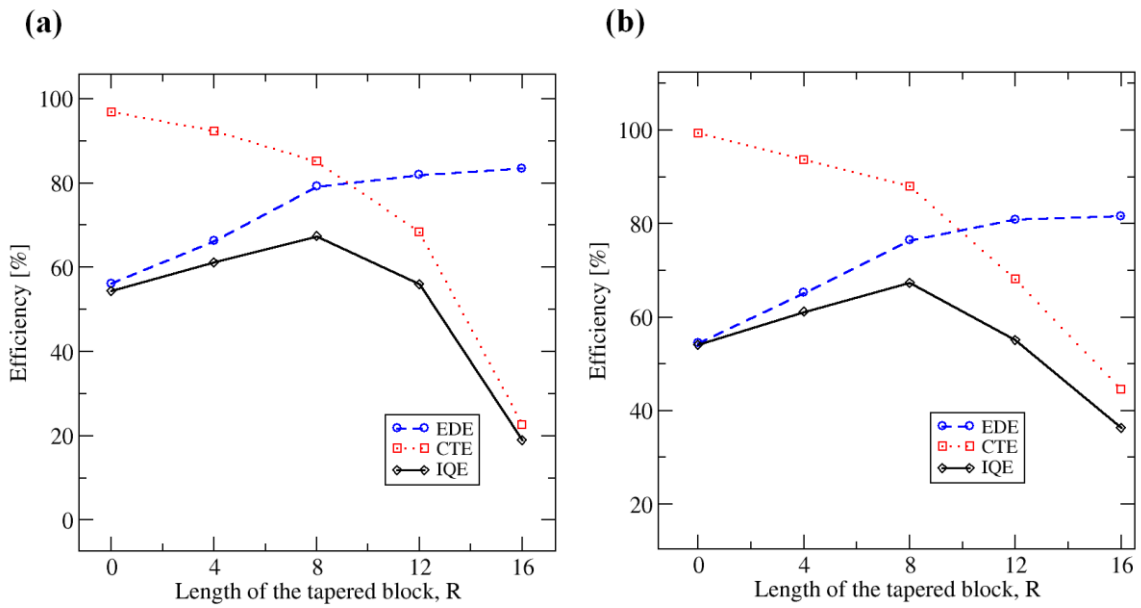

Fig. 6.4: (a) EDE, CTE, and IQE in the lamellar-like nanostructures, corresponding to the block copolymers PFB-F8BT with the different length of the tapered block. (b) The same quantities, obtained by using the parameterized values of charge transfer integral.

of the IQE improvement is size dependent. To study this effect in more detail, we eliminated in our particle-based algorithm the quantum-chemical calculation part by parameterizing the values of transfer integrals as a function of distances between the monomers. We started with the analysis of the quality of this approximation by calculating the efficiencies of the previously introduced tapered block-copolymer system, obtained this time by using the parameterized values of the transfer integral. In Fig. 6.4 (b) we visualize the corresponding simulation results. By comparing the results of Fig. 6.4 (b) with Fig. 6.4 (a), we conclude that the values of the EDE, CTE, as well as IQE for both parameterized and unparameterized cases are in perfect agreement for the ordered morphologies with the tapered middle block length less than 8. However, for the disordered morphologies with large middle tapered block length $D_4R_{12}A_4$ and $D_2R_{16}A_2$ the quantities deviate in the values. In particular, for the morphology $D_2R_{16}A_2$ the CTE in the parameterized simulations is overestimated by a factor of 2. From these observations, we conclude that the applied approximation can efficiently be used in case the morphology possesses a relatively small interfacial region with low mixing of D- and A-

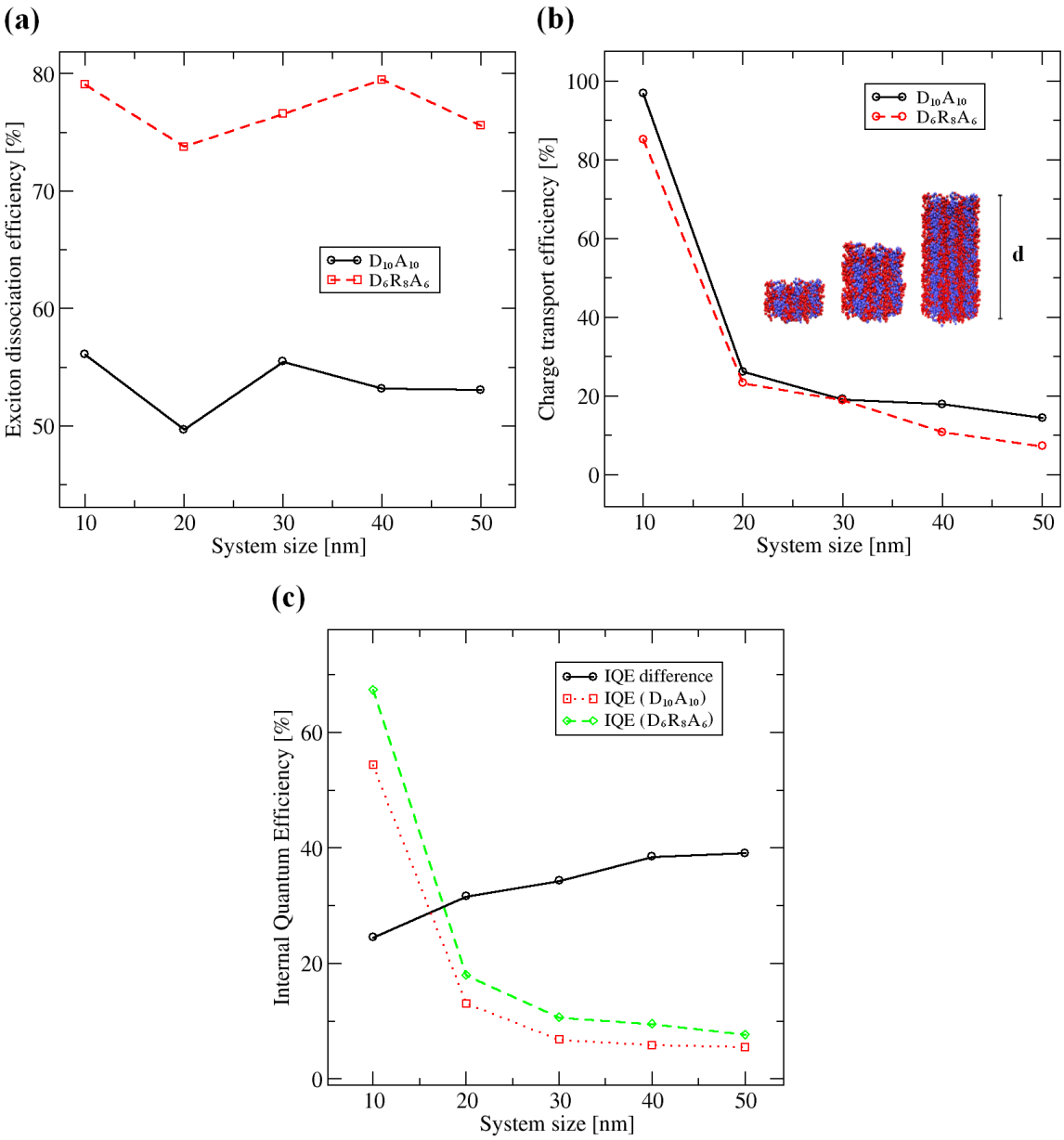

Fig. 6.5. The dependences of EDE (a) and CTE (b) as the functions of the system size, obtained for the morphologies, corresponding to diblock-copolymer $D_{10}A_{10}$ and tapered block-copolymer $D_6R_8A_6$. The resulting values of IQE as well as the improvement of the device efficiency are visualized in figure (c).

monomers. With larger interfacial mixing and larger degree of mixing, additional parameters in the fit function, characterizing the orientation of the monomers, could improve the convergence in the values. However, we point out that for both the $D_6R_8A_6$- and $D_{10}A_{10}$-block

copolymers the values of the EDE, CTE as well as IQE, calculated either directly or by eliminating the quantum chemical calculation part, are identical.

Furthermore, to study the dependence of the IQE on the system size, we increased the size of $D_6R_8A_6$ and $D_{10}A_{10}$-block copolymer morphologies in direction of the DA-interface and calculated the values of the EDE, CTE and IQE for each of the morphologies. The results of these simulations are shown in Fig. 6.5. With increasing system size in direction of the DA-interface, we observe oscillations of the EDE around their average values of 76 % for $D_6R_8A_6$ and 56 % for $D_{10}A_{10,}$ respectively. By contrast, in case of CTE we see a drastic decrease of CTE from 97 % to 15 % and from 83 % to 8 % for the polymers $D_{10}A_{10}$ and $D_6R_8A_6$, respectively. The relatively steady behavior of the EDE can be associated with the small exciton diffusion length of 5.1 nm and system symmetry. By contrast, we explain the rapid change of the CTE with the increase of the morphology size from 10 to 20 nm by the fact that a significant fraction of the free charge carriers in the small morphology is generated in proximity to the electrodes. At the same time, the further decrease of the CTE is related to the increase of the pathway lengths, which enhances the probability of charge recombination. As a result, we see the steady decrease of the IQE for both the $D_{10}A_{10}$ and $D_6R_8A_6$-block copolymers as a function of system size, which is in agreement with the earlier theoretical findings of Casalegno *et al* [57], obtained on the MDMO-PPV and PCBM polymer blend systems. Finally, we observe the systematic increase of IQE difference between the untapered $D_{10}A_{10}$-diblock copolymer- and tapered $D_6R_8A_6$-block copolymer-system, which for the largest system size of 50 nm tends to the value of 39 %. By afterwards considering in Fig. 6.5 (c) the corresponding relative change in the IQE of the tapered D6R8A6-block-copolymer system with regard to the untapered D10A10-diblock-copolymer system, we conclude that the efficiency of the tapered solar-cell system with regard to the untapered case steadily increases with system size. For the largest system size considered in this work, i.e. 50 nm, the gain in IQE amounts to a value of about 39 %, which demonstrates that the tapering technique is a viable approach to improve the performance of polymer solar cells.

Conclusions and further perspectives

7. Conclusions and further perspectives

The goal of the present thesis was to develop and apply multiscale solar cell algorithms for investigating the influence of polymeric morphology on the performance of polymer-based solar cells. These nanodevices possess important advantages for organic photovoltaic applications, such as low production costs and light weight. However, they suffer from a low device efficiency in comparison to their inorganic counterparts. During the past decade, the problem of low efficiency of organic solar cells was a subject of many theoretical studies, attempting to identify the relationship between the polymeric morphology and its photovoltaic performance. However, most of the proposed approaches could not correlate the morphology with optimal photovoltaic performance and corresponding polymer composition, either due to a bad polymer model or a bad treatment of elementary photovoltaic processes. In contrast, the goal of this thesis was to study the relationship between the polymeric morphology and photovoltaic efficiency by making use of both realistic polymer models and efficient treatment of elementary photovoltaic processes.

As we described in the introduction, there are two major factors, which limited the application of theoretical methods for simulating the elementary photovoltaic processes in polymer-based nanodevices till this date: (i) large time- and length-scales, required for characterizing the polymer phase separation process, and (ii) high sensitivity of exciton- and charge-transport parameters to the local environment. To overcome these problems, we developed two novel multiscale solar cell algorithms, which are based on the coupling of the dynamical Monte-Carlo technique and polymer field theory. The combination of these two methods permitted us to handle time- and length-scales of polymer phase separation process and, at the same time, to take into account the dependence of exciton- and charge-transport parameters on the local environment.

In chapter 2 we started with the introduction of theoretical background for dynamical Monte-Carlo technique. First of all, we considered the Förster resonance theory and different charge transport models, used for organic semiconductors. Then, we introduced the Marcus theory together with the related parameters and methods for their determination. Finally, we described the underlying algorithm of the dynamical Monte Carlo modeling technique. In

chapter 3, we focused on the SCFT formalism, which was used in this thesis for the description of the polymer phase separation process. To this end, we started with the description of the models, used in the approach to characterize the behavior of single polymer chains and, then, we showed how SCFT handles different polymer mixtures of interest, namely, homo-polymer blends and block-copolymers. Next, we described the algorithm for determining the numerical SCFT solution. The last section of this chapter dealt with the problem of coupling the SCFT method and dynamical Monte Carlo algorithm.

By combining the dynamical Monte-Carlo technique with polymer field theory, we developed two novel multiscale simulation techniques for treating the elementary photovoltaic processes in nanostructured polymeric morphologies. The first technique, which is called the field-based simulation approach, was invented for efficient treatment of polymer models within the mean-field approximation at mesoscopic time- and length-scales. The second technique, namely, the particle-based simulation approach, was used to enable a correct handling of the mixing regions at the DA interface within the Marcus theory as well as chemical details of the polymers. In the course of this research work, both approaches were applied to various polymer systems with the purpose of determining the physical and chemical characteristics of the polymers with the highest photovoltaic efficiencies under different circuit conditions. The results of our development and simulations were summarized as follows.

In chapter 4 we described the development and application of a novel field-based solar cell algorithm for studying the loss processes in polymer solar cell nanodevices. Our simulation approach was based on combining the dynamical self-consistent field theory method, to generate morphologies of different scale of phase separation and degree of defect formation, with a dynamical Monte Carlo method, to simulate the elementary photovoltaic processes involving the charge carriers and excitons in particle description. We applied the approach on a novel phase-separated nanostructured polymer blend, based on the electron-donating compound bis(thienylenevinylene)-substituted polythiophene and the electron-accepting compound poly(perylene diimide-alt-dithienothiophene). We found that structural inhomogeneities, such as inclusions and dead ends, significantly affect the internal quantum efficiency of the photovoltaic system. These defects are usually generated in course of the phase-separation process and are inherent artifacts produced during the fabrication procedure.

More specifically, we observed that the disjunction of continuous percolation paths leads to the creation of dead ends, which cause severe charge carrier losses through charge recombination lowering the charge transport efficiency in a decisive way. At the same time, we found that dead ends are characterized by low exciton dissociation efficiency due to a high accumulation of charge carriers, counteracting the charge generation process. From these observations, we concluded that both loss phenomena lead to a dramatic decrease in the internal quantum efficiency. Moreover, by analyzing the photovoltaic behavior of the nanostructures under different circuit conditions we demonstrated that the dark current crucially determines the impact of the inhomogeneities on the solar cell performance.

In chapter 5 we studied the role of mixing of D- and A-monomers on the performance of OPV devices. To this end, we focused on the polymer blend, composed of poly(9,9-dioctyluorene-co-bis-N,N-(4-butylphenyl)-bis-N,N-phenyl-1,4-phenylene-diamine) (PFB) and poly(9,9-dioctyluorene-co-benzo-thiadiazole) (F8BT). By comparing the results of our field-based solar cell algorithm with the ones of a novel particle-based solar cell algorithm at atomistic resolution, we have demonstrated that the mixing of the D- and A-monomers in a lamellar-like PFB-F8BT polymer blend causes that the major part of the charge generation and charge transport takes place at the domain centers of the nanostructured polymer blends in agreement with recent electrostatic force and photocurrent microscopy experiments. The contribution of the exciton dissociation efficiency, due to mixing of the D- and A- monomers, to the overall device efficiency is substantial and, therefore, cannot be neglected in simulation-based performance studies of such systems at the nanoscale. Moreover, we investigated the influence of polymer photo-oxidation on the charge transport properties within the polymer morphology. In this study, we have found that keto-defects on the fluorene moiety of the F8BT phase, induced by photo-oxidation, cause a simultaneous increase of the intra-chain contribution to the electronic current density and decrease of the corresponding inter-chain contribution, whereas in the reduced form the difference between both contributions is much smaller. This effect leads to the keto-induced trapping of electrons on the same chain in the photo-oxidized case, resulting in a deterioration of the overall electron transport efficiency in the F8BT phase of the polymer solar cell.

In chapter 6 we summarized our gained knowledge on the role of DA mixed regions and, basing on this, proposed an approach to improve the IQE of diblock-copolymer solar

cells. This was achieved by controlling the width of the interfacial region between the D- and A- domains through the application of the tapered block-copolymer technology. To investigate the effect of the interfacial width on the IQE, we generated a set of lamellar-like nanoscale morphologies, which differed from each other through the composition of the D- and A-nanophases. Our simulation results revealed that an extension of the length of the tapered middle block leads to a substantial increase of the exciton dissociation efficiency and reduces the charge transport efficiency only moderately. At the optimal tapered block length, the internal quantum efficiency exhibits a maximum, which corresponds to the best compromise between the exciton-dissociation- and charge-transport-efficiency. Overall, this provides a gain in the internal quantum efficiency with regard to the untapered case from 25 % up to 39 % by increasing the active layer thickness from 10 up to 50 nm in direction to the DA interface. This demonstrates that the tapering technique is an effective methodology to rise the photovoltaic performance of polymer solar cells and, thus, confers promising potential to increase their usefulness in flexible nanodevice applications.

To conclude, in this thesis we proposed two novel multiscale modeling techniques for treating the elementary photovoltaic processes in polymer solar cell nanodevices at both mesoscopic and atomistic level of system description. These algorithms have been applied for studying the loss phenomena, occurring in the polymer morphology, in particular, at structural defects, which are formed within the polymer phase separation process. Specific attention has been focused on the role of donor- and acceptor-polymer mixing on the performance of organic photovoltaic devices. Finally, we proposed a novel approach, to improve the photovoltaic performance of polymer-bulk heterojunctions, based on random tapering of a polymer segment encompassing the chemical junctions between the electron-donating and electron-accepting blocks of the diblock copolymer molecules. We believe that the results of our simulations are valuable for both fundamental and applied research. Moreover, we expect that our findings can efficiently serve the purpose to facilitate the progress in the field of organic photovoltaic nanodevices.

Our research on multiscale modeling of polymer solar cell can be characterized as pioneering work in the field of solar cell simulation. As such, significant amount of time was invested in the development of the appropriate simulation algorithms. For this reason, there were several aspects and applications of our research, which we could not consider in present

thesis, but they would be of interest for further work. In particular, in present thesis we focused on amorphous polymers and, consequently, our entire findings were primary related to disordered materials. Of interest would be to study the phase separation process as well as the photovoltaic behavior of semicrystalline polymer materials with partially crystalline and amorphous domains. For this, the underling Gaussian chain model, described in chapter 3.1.1, should be replaced by a polymer model, which takes into account both distances and angles between the polymer segments. Among the existing models, the worm-like chain model could be used for this purpose [56]. As an additional challenge, the density biased Monte Carlo procedure should be modified to enable the generation of the atomistically resolved crystalline phases. Moreover, it would be useful to employ the beyond mean-field theory, which takes into account density fluctuations. This could lead to a better agreement between the calculated morphology and the experimental measurements in cases, where the density fluctuations play an important role [56].

For solar cell applications, it would also be of great importance to study the influence of morphology preparation conditions on the device performance. Of particular interest in this regard is the impact of solvent evaporation rate, solvent composition, and thermal annealing on the polymer phase separation process. We point out that this research could be accomplished by using the solar cell algorithms, proposed in this thesis, in conjunction with the features of OCTA simulation package [71]. Moreover, specific interaction between the polymers and the material of electrodes could also be taken into account. Currently, this research is carried in our group and its results will be presented elsewhere.

Furthermore, in this thesis we proposed two approaches, allowing to simulate the elementary photovoltaic processes, namely, the field-based and the particle-based approaches. Each of the approaches has its own advantages: the field-based approach can handle large polymeric morphologies, while the particle-based approach can efficiently deal with the local characteristics of the morphology such as the DA mixed regions or the chemical details of the polymers. A further goal will be to include information from one representation to the other, which permits to combine the advantages of both algorithms and reduce the computational needs. To this end, we consider the possibility to parameterize the values of the charge transfer integrals as a function of polymer volume fractions of the polymer systems. This dependence can be obtained by averaging the values over the atomistic morphology and

associating them with the corresponding volume fraction of polymer systems. As an example, in Fig. 7.1 we show the values of the transfer integrals as a function of PFB volume fraction of the PFB-F8BT blend, depicted in Fig. 5.3 (b). We believe that through the inclusion of these parameters into the field-based simulation strategy, we can achieve the accuracy of the particle-based algorithm at mesoscopic time- and length-scales at moderate computational costs. This work is currently carried out in our research group and the results will be present elsewhere.

Additional improvements could be done by making use of more sophisticated transport theories to describe charge carrier and exciton motion. For instance, in the present thesis we followed the suggestions of several works [36, 46], which neglected the outer-sphere contribution of the reorganization energy. However, to extend the applicability of our approach to a broader class of solar cell applications, such as, for example, dye synthesized

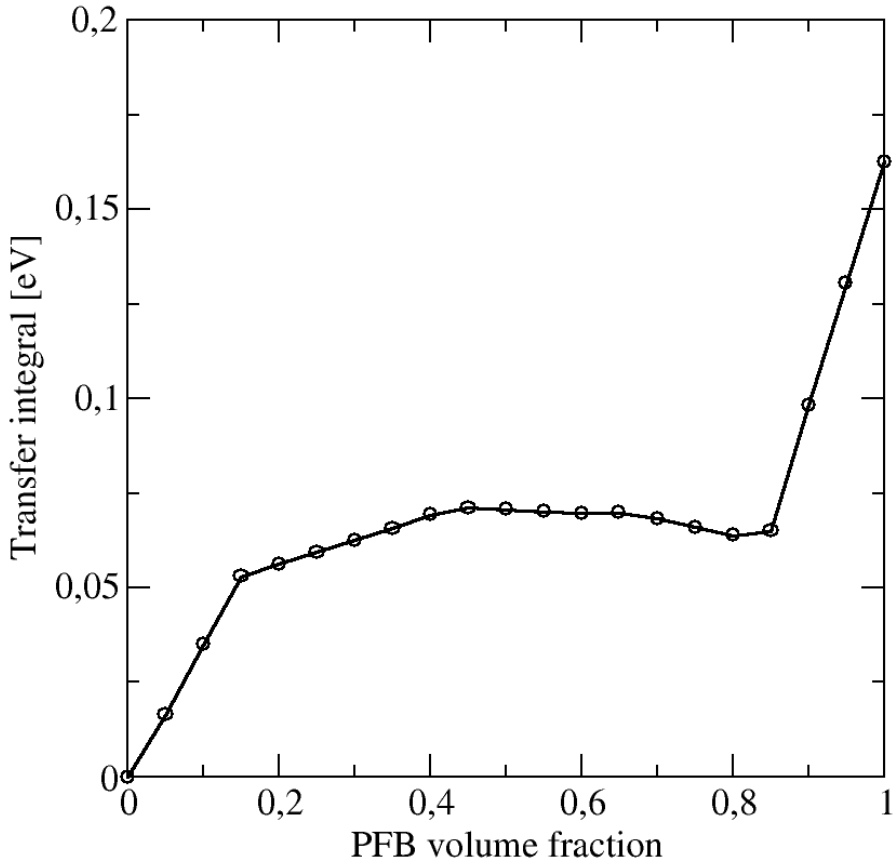

Fig. 7.1: The dependency of the charge transfer between the PFB monomers on the PBF volume fraction, obtained for the PFB-F8BT polymer blend.

solar cells [131], the contribution of the environment should be taken into account. This can be achieved by calculating the outer sphere contribution of the reorganization energy by solving the Boltzmann-Poisson equations. Moreover, it is worth mentioning that the underling Marcus theory is only valid at high temperatures and for the specific type of polymers, in which the electronic coupling is much smaller than the reorganization energy. To increase the scope of application of our solar sell algorithms, we could make use of general charge transport theories, such as the Hannewald model [132].

8. References

[1] M. Graetzel, R. A. Jannsen, D. B. Mitzi, and E. H. Sargent, *Nature* **488**, 304 (2012).

[2] R. Janssen, "Introduction to polymer solar cells", http://faculty.mu.edu.sa/public/uploads/1339275819.829Polymer%20solar%20cells.pdf

[3] T. Kietzke, *Adv. Optoelectron* **2007** (2007).

[4] T. Ameri, P. Khoram, J. Min, and C. J. Brabec, *Adv. Mater.* **25** (2013).

[5] P. Kumar and S. Chand, *Prog. Photovolt: Res. Appl.*, **20**, 337 (2012).

[6] S-S. Sun, C. Zhang, A. Ledbetter, S. Choi, K. Seo, and J. Haliburton, *Appl. Phys. Lett.* **90** (2007).

[7] K. Mueller and R. Borges, *Solar Industry* **1**, 10 (2010).

[8] J.Y. Kim, K. Lee, N. E. Coates, D. Moses, and T.Q. Nguyen, *Science* **317**, 222 (2007).

[9] J. A. Hauch, P. Schilinsky, S. A. Choulis, R. Childers, M. Biele, and C.J. Brabec, *Sol. Energ. Mat. Sol. Cells* **92**,727 (2008).

[10] http://pveducation.org/pvcdrom/solar-cell-operation/short-circuit-current

[11] http://blog.disorderedmatter.eu/2008/03/05/intermediate-current-voltage-characeristics-of-organic-solar-cells/

[12] H. Sirringhaus, *Adv. Mat.* **17**, 20 (2005).

[13] V. C. Sundar *et al*., *Science* **303**, 5664 (2004).

[14] T. D. Anthopoulos *et al*., *Appl. Phys. Lett*. **89**, 21 (2006).

[15] D. J. Gundlach, K. P. Pernstich, G. Wilckens, M. Grueter, S. Haas, and B. Batlogg *J. Appl. Phys*., **98**, 6 (2005).

[16] R. N. Marks, J. J. M. Halls, D. D. C. Bradley, R. H. Friend, and A. B. Holmes, *J. Phys.* **7**, 7 (1994).

[17] C. W. Tang, *Appl. Phys. Lett*, **48**, 183 (1986).

[18] A. C. Mayer, S. R. Scully, B. E. Hardin, M. W. Rowell, and M. D. McGehee, *Mater. Today* **10**, 28 (2007).

[19] M. Hilczer and M. Tachiya, *J. Phys. Chem. C* **114**, 6808 (2010).

[20] P. D. Topham, A. J. Parnell, and R. C. Hiorns, *J. Polym. Sci. Part B Polym. Phys.* **49**, 1131 (2011).

[21] Ch. Mueller, E. Wang, L. M. Andersson, K. Tvingstedt, Y. Zhou, M. R. Andersson, and O. Inganaes, *Adv. Func. Mat.* **20**, 2124 (2010).

[22] F. Padinger, R. S. Rittberger, and N. S. Sariciftci, *Adv. Func. Mat.* **13**, 85 (2003).

[23] M. L. Chabinyc, *Polym. Rev.* **48** (3) (2008).

[24] P. D. Andersen, J. C. Skarhoj, J. W. Andreassen, and F. C. Krebs, *Opt. Mater.* **31**, 1007 (2009).

[25] R. C. Nieuwendaal, C. R. Snyder, R. J. Kline, E. K. Lin, D. L. VanderHart, and D. M. DeLongchamp, *Chem. Mat.* **22** (9), (2010).

[26] A.N. Sokolov *et al*., *Nat. Commun*. **2**, 437 (2011).

[27] D. Chandler, Oxford University press, New York (1987).

[28] P. K. Watkins, A. B. Walker and G. L. B. Verschoor, *Nano Lett.* **5**, 1814 (2005).

[29] G. Parisi, Addison-Wesley, New York (1988).

[30] T. Forster, *Ann. Phys.,* **6** (1948).

[31] J. Seogjoo and C. Yuan-Chung. *WIREs Comput Mol Sci*, **3** (2013).

[32] K. Feron, W. J. Belcher, C. J. Fell, and P. C. Dastoorl, *Int. J. Mol. Sci.* **13**(12) (2012).

[33] K. M. Gaab and C. J. Bardeen, *J. Phys. Chem. B*. **108** (2004).

[34] F. Fennel, S. Lochbrunner, *Phys. Rev. B.* **85** (2012).

[35] A. Troisi, *Adv. Polym. Sci*. **223** (2010).

[36] B. Baumeier, J. Kirkpatrick, and D. Andrienko, *Phys. Chem. Chem. Phys*. **12** (2010).

[37] L.D. Landau, *Sov. Phys.3* **664** (1933).

[38] R.A. Marcus, *Rev. Modern Physics* **65**, 3 (1993).

[39] A. Tokmakoff, http://www.mit.edu/~tokmakof/TDQMS/Notes/12.2.%20Marcus.pdf

[40] G. Nan, L. Wang, X. Yang, Z. Shuai, and Y. Zhao, *J. Chem. Phys.* **130** (2009).

[41] S. E. Koh, C. Risko, D. A. da Silva Filho, O. Kwon, A. Facchetti, J.-L. Brédas, T. J. Marks, and M. A. Ratner, *Adv. Funct. Mater*. **18** (2008).

[42] P.-O. Löwdin, *J. Chem. Phys*. **18**, 365 (1950).

[43] J. Blumberger and G. Lamoureux, *Mol. Phys.* **106**, 12 (2008).

[44] A.-M. Kelterer, S. Landgraf, and G. Grampp, *Spectrochim. Act. A* **57** (2001).

[45] K. Asadi , A. J. Kronemeijer , T. Cramer, L. Jan Anton Koster, P. W. Blom, and D. M. de Leeuw, *Nat. Commun.*, **4** (2013).

[46] J. Kirkpatrick, V. Marcon, J. Nelson, K. Kremer, and D. Andrienko, *Phys. Rew. Lett.*, **98** (2007).

[47] J. R. Norris, *"*Marcov chains*"*, Cambridge University Press (1998).

[48] A. O'Hagan and J. Forster, New York: Oxford University Press, **2**B (2004).

[49] http://morris.umh.ac.be/ResearchTopic.aspx?id=2

[50] A. Pershin, S. Donets, and S. A. Baeurle, *J. Chem. Phys.* **136**, 19 (2012).

[51] G. Gompper and M. Schick, "Soft Matter, Volume 1: Polymer Melts and Mixtures", Wiley-VCH Verlag GmbH & Co (2006).

[52] M. Doi and S. F. Edwards, "The Theory of Polymer Dynamics", Oxford University Press (1988).

[53] A. T. Freitas and A. L. Oliveira, *DATE* Mar. (2003).

[54] N. Cufaro Petroni, S. De Martino, and S. De Siena, *Phys. Lett. A* **245** (1998).

[55] K. S. Fa, *Phys. Rew. E*, **84** (2011).

[56] G. Fredrickson, "The equilibrium theory of inhomogeneous polymers", Oxford University Press (2006).

[57] M. Casalegno, G. Raos, and R. Po, *J. Chem. Phys.* **132** (2010).

[58] U. Stalmach, B. de Boer, C. Videlot, P. F. van Hutten, and G. Hadziioannou, *J. Am. Chem. Soc.* **122**, (2000).

[59] Kendall A. Atkinson, "An Introduction to Numerical Analysis (2nd ed.)", New York: John Wiley & Sons (1989).

[60] T. Aoyagi, T. Honda, and M. Doi, *J. Chem. Phys.* **117** (2002).

[61] Th. D. Sewell, K. Ø. Rasmussen, D. Bedrov, G. D. Smith, and R. B. Thompson, *J. Chem. Phys.* **127** (2007).

[62] G. A. Buxton and N. Clarke, *Model. Simul. Mater. Sci. Eng.* **15**, 13 (2007).

[63] B. A. Gregg and M. C. Hanna, *J. Appl. Phys.* **93**, 3605 (2003).

[64] J. A. Barker, C. M. Ramsdale, and N. C. Greenham, *Phys. Rev. B***, 67**, 075205 (2003).

[65] J. O. Haerter, S. V. Chasteen, S. A. Carter, and J. C. Scott, *Appl. Phys. Lett.*, **86**, 164101 (2005).

[66] G. A. Buxton and N. Clarke, *Phys. Rev. B* **74**, 085207 (2006).

[67] R. A. Marsh, C. Groves, and N. C. Greenham, *J. Appl. Phys.* **101**, 083509 (2007).

[68] R. A. Marcus, *Rev. Mod. Phys*. **65**, 599 (1993).

[69] K. Seki and M. Tachiya, *Phys. Rev. B* **65**, 014305 (2001).

[70] R. G. E. Kimber, A. B. Walker, G. E. Schröder-Turk, and D. J. Cleaver, *Phys. Chem. Chem. Phys.* **12**, 844 (2010).

[71] See http://octa.jp/ for information about OCTA-program.

[72] S. C. Glotzer and W. Paul, *Annu. Rev. Mater. Res.* **32**, 401 (2002).

[73] H. Tang and K. F. Freed, *J. Chem. Phys.* **94**, 6307 (1991).

[74] M. Doi, *Macromol. Symposia* **195**, 101 (2003).

[75] L. Meng, Y. Shang, Q. Li, Y. Li, X. Zhan, Z. Shuai, R. G. E. Kimber, and A. B. Walker, *J. Phys. Chem. B* **114**, 36 (2010).

[76] X. Zhan, Z. Tan, B. Domercq, Z. An, X. Zhang, S. Barlow, Y. Li, D. Zhu, B. Kippelen, and S. R. J. Marder, *J. Am. Chem. Soc*. **129**, 7246 (2007).

[77] H. J. Snaith, A. C. Arias, A. C. Morteani, C. Silva, and R. H. Friend, *Nano Lett.* **2**, 1353 (2002).

[78] D. C. Coffey and D. S. Ginger, *Nat. Mater*. **5**, 735 (2006).

[79] D. Coffey and D. Ginger, *SPIE Newsroom* 27 February (2007).

[80] C. R. McNeill, B. Watts, L. Thomsen, W. J. Belcher, N. C. Greenham, and P. C. Dastoor, *Nano Lett.*, **6**, 1202 (2006).

[81] P. Peumans, S. Uchida, and S. R. Forrest, *Nature (London)* **425**, 158 (2003).

[82] T.L. Morkved, M. Lu, A. M. Urbas, E. E. Ehrichs, H.M. Jaeger, P. Mansky, and T. P. Russell, *Science* **273**, 931 (1996).

[83] C. R. McNeill, S. Westenhoff, C. Groves, R. H. Friend, and N. C. Greenham, *J. Phys. Chem. C* **111**, 19153 (2007).

[84] D.Wang, M. Reese, N. Kopidakis, and B. A. Gregg, *NREL/CP-270-42565* May 2008.

[85] P. D. Topham, A. J. Parnell, and R. C. Hiorns, *J. Polym. Sci. Part B: Polym. Phys.* **49**, 1131 (2011).

[86] D. Pospiech, "Influencing the interface in polymer blends by compatibilization with block copolymers," in *Polymer Surfaces and Interfaces*, edited by M. Stamm (Springer, Berlin, 2008), pp. 275–298.

[87] R. Mukherjee, A. Sharma, and U. Steiner, "Surface instability and pattern formation in thin polymer films," in *Generating Micro- and Nanopatterns on Polymeric Materials*, edited by A. del Campo and A. Arzt (Wiley-VCH, Weinheim, 2011), p. 246.

[88] J. Peet, M. L. Senatore, A. J. Heeger, and G. C. Bazan, *Adv. Mater.* **21**, 1521 (2009).

[89] S.-S. Sun, C. Zhang, A. Ledbetter, S. Choi, K. Seo, and J. Haliburton, *Appl. Phys. Lett*. **90**, 043117 (2007).

[90] S. M. Lindner, S. Hüttner, A. Chiche, M. Thelakkat, and G. Krausch, *Angew. Chem. Int. Ed.* **45**, 3364 (2006).

[91] S. Donets, A. Pershin, M. Christlmaier, and S.A. Baeurle, *J. Chem. Phys*. **138**, 094901-1-094901-12 (2013).

[92] A. Pershin, S. Donets, and S. A. Baeurle, "Photocurrent contribution from inter-segmental mixing in donor-acceptor-type polymer solar cells: A theoretical study", *submitted* (2013).

[93] J. A. Bartelt, Z. M. Beiley, E. T. Hoke, W. R. Mateker, J. D. Douglas, B. A. Collins, J. R. Tumbleston, K. R. Graham, A. Amassian, H. Ade, J. M. J. Fréchet, M. F. Toney, and M. D. McGehee, *Adv. Energy Mater.* **3 (20**13),.

[94] H. Yan, S. Swaraj, C. Wang, I. Hwang, N. C. Greenham, C. Groves, H. Ade, and C. R. McNeill, *Adv. Funct. Mater*. **20** (2010).

[95] A. A. Virkar, S. Mannsfeld, Z. Bao, and N. Stingelin, *Adv. Mater*. 22, 3857 (2010).

[96] W. H. Lee, J. H. Cho, and K. Cho, *J. Mater. Chem*. **20**, 2549 (2010).

[97] R. G. E. Kimber, A. B. Walker, G. E. Schöder-Turkc and D. J. Cleaver, *Phys. Chem. Chem. Phys.* **12**, 844 (2010).

[98] O. G. Reid, G. E. Rayermann, D. C. Coffey and D. S. Ginger, *J. Phys. Chem. C* **114**, 20672 (2010), and references therein.

[99] M. Doi, *Macromol. Symposia* **195**, 101 (2003).

[100] T. Aoyagi, T. Honda and M. Doi, *J. Chem. Phys.*117, 8153 (2002).

[101] T. Aoyagi, F. Sawa, T. Shoji, H. Fukunaga, J. Takimoto and M. Doi, *Comput. Phys. Commun.* **145**, 267 (2002).

[102] W. F. van Gunsteren and H. J. C. Berendsen, *Mol. Phys.* **45**, 637 (1982).

[103] E. Lindahl, B. Hess, and D. van der Spoel, *J. Mol. Model.* **7**, 306 (2001).

[104] W. L. Jorgensen, D. S. Maxwell, and J. Tirado-Rives, *J. Am. Chem. Soc.* **118**, 11225 (1996).

[105] G. A. Kaminski, R. A. Friesner, J. Tirado-Rives, and W. L. Jorgensen, *J. Phys. Chem. B* **105**, 6474 (2001).

[106] D. Frenkel and B. Smit, "Understanding molecular simulation: from algorithms to applications" Academic, San Diego (2003).

[107] L. Meng, Y. Shang, Q. Li, Y. Li, X. Zhan, Z. Shuai, R. G. E. Kimber and A. B. Walker, *J. Phys. Chem. B* **114**, 36 (2010).

[108] X. Zhan, Z. Tan, B. Domercq, Z. An, X. Zhang, S. Barlow, Y. Li, D. Zhu, B. Kippelen and S. R. J. Marder, *J. Am. Chem. Soc.*, **129**, 7246 (2007).

[109] H. Yan, S. Swaraj, C. Wang, I. Hwang, N. C. Greenham, C. Groves, H. Ade and C. R. McNeill, *Adv. Funct. Mater.* **20**, 4329 (2010).

[110] V. Ruehle, A. Lukyanov, F. May, M. Schrader, T. Veho, J. Kirkpatrick, B. Baumeier, D. Andrienko, *J. Chem. Theory Comput*. **7**, 3335 (2011).

[111] J. P. Perdew, K. Burke and M. Ernzerhof, *Phys. Rev. Lett*. 77, 3865 (1996).

[112] Gaussian 03, Revision C.02, M. J. Frisch, G. W. Trucks, H. B. Schlegel, G. E. Scuseria, M. A. Robb, J. R. Cheeseman, J. A. Montgomery, Jr., T. Vreven, K. N. Kudin, J. C. Burant, J. M. Millam, S. S. Iyengar, J. Tomasi, V. Barone, B. Mennucci, M. Cossi, G. Scalmani, N. Rega, G. A. Petersson, H. Nakatsuji, M. Hada, M. Ehara, K. Toyota, R. Fukuda, J. Hasegawa, M. Ishida, T. Nakajima, Y. Honda, O. Kitao, H. Nakai, M. Klene, X. Li, J. E. Knox, H. P. Hratchian, J. B. Cross, V. Bakken, C. Adamo, J. Jaramillo, R. Gomperts, R. E. Stratmann, O. Yazyev, A. J. Austin, R. Cammi, C. Pomelli, J. W. Ochterski, P. Y. Ayala, K. Morokuma, G. A. Voth, P. Salvador, J. J. Dannenberg, V. G. Zakrzewski, S. Dapprich, A. D. Daniels, M. C. Strain, O. Farkas, D. K. Malick, A. D. Rabuck, K. Raghavachari, J. B. Foresman, J. V. Ortiz, Q. Cui, A. G. Baboul, S. Cli_ord, J. Cioslowski, B. B. Stefanov, G. Liu, A. Liashenko, P. Piskorz, I. Komaromi, R. L. Martin, D. J. Fox, T. Keith, M. A. Al-Laham, C. Y. Peng, A. Nanayakkara, M. Challacombe, P. M. W. Gill, B. Johnson, W. Chen, M. W. Wong, C. Gonzalez and J. A. Pople, Gaussian, Inc., Wallingford CT (2004).

[113] C. R. McNeill, H. Frohne, J. L. Holdsworth, and P. C. Dastoor, *Nano Lett*. **4**, 2503 (2004).

[114] J. L. Luria, N. Hoepker, R. Bruce, A. R. Jacobs, C. Groves, and J. A. Marohn, *ACS Nano* **6**, 9392 (2012).

[115] M. McGehee „Progress in making organic solar cells highly efficient and stable", http://talks.cam.ac.uk/talk/index/45589.

[116] Y.-Y. Noh, D.-Y. Kim, Y. Yoshida, K. Yase, B.-J. Jung, E. Lim, H.-K. Shim and R. Azumi, *J. Appl. Phys.* **97**, 104504 (2005).

[117] Y.-Y. Noh, D.-Y. Kim, Y. Yoshida, K. Yase, B.-J. Jung, E. Lim, H.-K. Shim and R. Azumi, *J. Appl. Phys*. **85**, 2953 (2004).

[118] A. Van Vooren, J.-S. Kim, and J. Cornil, *ChemPhysChem* **9**, 989 (2008), and references therein.

[119] S. Van Bavel, E. Sourty, G. de With, S. Veenstra, and J. Loos, *J. Mater. Chem.* **19** (2009).

[120] G. Li, V. Shrotriya, J. Huang, Y. Yao, T. Moriarty, K. Emery, and Y. Yang, *Nat. Mater*. **4**, 864 (2005).

[121] Y. Liang, Z. Xu, J. Xia, S.-T. Tsai, Y. Wu, G. Li, C. Ray, and L. Yu, *Adv. Mater*. **22**, E135 (2010).

[122] T.-Y. Chu, S. Alem, S.-W. Tsang, S.-C. Tse, S. Wakim, J. Lu , G. Dennler, D. Waller, R. Gaudiana, and Y. Tao, *Appl. Phys. Lett.* **98** (2011).

[123] K. Knoll and N. Niessner, *Macromol. Symp,* **132**, 231 (1998).

[124] R. Roy, J. K. Park, W.-Sh. Young, S. E. Mastroianni, M. S. Tureau, and Th. H. Epps, *Macromolecules* **44** (10) (2011).

[125] P. Hodrokoukes, G. Floudas, S. Pispas, and N. Hadjichristidis, *Macromolecules* **34**, (2001).

[126] W. F. Kuan, R. Roy, L. Rong , B. S. Hsiao, and T. H. Epps 3rd., *ACS Macro Lett*, **1** (4) (2012).

[127] V. Rühle, C. Junghans, A. Lukyanov, K. Kremer, and D. Andrienko, *J. Chem. Theory Comput*. **5** (12), (2009).

[128] W. L. Jorgensen, D. S. Maxwell, and J. Tirado-Rives, *J. Am. Chem. Soc*. **118**, 11225 (1996).

[129] E. Lindahl, B. Hess, and D. van der Spoel, *J. Mol. Model.* **7**, 306 (2001).

[130] B. A. Collins, Z. Li, J. R. Tumbleston, E. Gann, C. R. McNeill, and H. Ade, *Adv. Energy Mater.* **3**, 65 (2013).

[131] V. Vaissier, P. Barnes, J. Kirkpatrick, and J. Nelson, *Phys. Chem. Chem. Phys.*, **15** (13) (2013).

[132] K. Hannewald, V. M. Stojanovic, J. M. T. Schellekens, P. A. Bobbert, G. Kresse, and J. Hafner, *Phys. Rev. B* **69** (2004).

Eidesstattliche Erklärung

Ich erkläre hiermit an Eides statt, dass ich die vorliegende Arbeit ohne unzulässige Hilfe Dritter und ohne Benutzung anderer als der angegebenen Hilfsmittel angefertigt habe; die aus anderen Quellen direkt oder indirekt übernommenen Daten und Konzepte sind unter Angabe des Literaturzitats gekennzeichnet.

Anton Pershin